Durham E-Theses

Off-Shell Effects for Single Top-Quark Production Processes at Hadron Colliders

MELLOR, PAUL

Off-Shell Effects for

Single Top-Quark Production

Processes at Hadron Colliders

A thesis submitted for the degree of

Doctor of Philosophy

by

Paul Mellor

Durham
University

Institute for Particle Physics Phenomenology

Durham University

2011

Abstract

We present a calculation of s- and t-channel single top-quark production and decay at next-to-leading order in QCD for the Tevatron and for the LHC. The calculation includes the off-shell effects of the intermediate top-quark and the non-factorisable corrections arising from interferences between the production and decay subprocesses, extending the results beyond the narrow-width approximation. A general method for including such effects is outlined. The method comprises a simultaneous expansion in the coupling constants, as in a standard perturbative approach, along with an expansion in the virtuality of the intermediate heavy-particle. This expansion makes it possible to identify the contributions relevant to the calculation, up to a desired accuracy, before computation of the amplitudes, allowing significant simplifications to be made to the final calculation. Results obtained using this method are presented, along with results obtained using both the standard and improved narrow-width approximations. This enables us to investigate the impact of both off-shell and spin-correlation effects on the cross section and various kinematic distributions. In general, both effects are found to be small except close to kinematic boundaries or for specific distributions, such as the top-quark invariant-mass, where their effects can become sizeable.

Declaration

I declare that no material presented in this thesis has previously been submitted for a degree at this, or any other, university. The research described in this thesis has been carried out in collaboration with Dr. Adrian Signer, Dr. Pietro Falgari and Dr. Floriana Giannuzzi. Chapters 1, 4, 5 and 6 are based on the published works:

- P. Falgari, P. Mellor and A. Signer, *"Production-Decay Interferences at NLO in QCD for t-channel Single-Top Production,"* Phys. Rev. D **82** (2010) 054028 [arXiv:1007.0893 [hep-ph]].

- P. Falgari, F. Giannuzzi, P. Mellor and A. Signer, *"Off-Shell Effects for t-channel and s-channel Single-Top Production at NLO in QCD,"* Phys. Rev. D **83** (2011) 094013 [arXiv:1102.5267 [hep-ph]].

Paul Mellor

August 2011

Acknowledgements

Of the many people who deserve thanks, some are particularly prominent.

First and foremost, I must thank my supervisor, Adrian Signer. Your support, guidance and approachability over the past five years have been invaluable. I wish you every success in your continued research.

I would also like to thank my other collaborators; Pietro Falgari, Floriana Giannuzzi and Andrew Papanastasiou. Your patience in the seemingly never-ending task of comparing cross sections was greatly appreciated.

I would like to thank my various office mates in OC215 who I wish the best of luck in their future endeavours, whatever they may be.

Away from the office, I would like to thank my housemates from both Ashwood and Kirkwood. In particular, I would like to thank Dr. Richard Abel and (Dr.) Luke Tyas for countless hours whiled away watching endless repeats of 'Family Guy' and for introducing me to the world of haute cuisine.

Special thanks must go to my girlfriend, Anneliese, for keeping me sane throughout the writing up process and for generally brightening up my life.

Finally, I would like to thank my family for their continued love and support. Most importantly, I would like to thank my parents for everything. Without you none of this would have been possible.

" For my parents"

Contents

List of Figures

List of Tables

Chapter 1

Introduction

As the Fermilab Tevatron enters its final months, CERN's Large Hadron Collider continues to collect data at the very start of its career. This signals a very exciting time in the world of particle physics, allowing for the potential discovery of new physics and the ability to explore many phenomena in much greater detail than ever before.

1.1 The Standard Model

The *standard model* of particle physics is a theory describing the fundamental particles of nature and their interactions. The predictions made by this theory have been consistently verified by experiment to a high degree of accuracy, proving it a very successful theory. Contained within the theory are three generations of fermionic particles, divided into quarks and leptons, and force-carrying exchange bosons. These are shown in Table 1.1. Each successive generation of fermions is a more massive copy of the last. Some mixing between quark generations is allowed. This mixing is governed by the Cabibbo-Kobayashi-Maskawa (CKM) matrix [1, 2]. The fermion with the greatest

Fermions {1st, 2nd, 3rd generation}	
Leptons	$\{e,\, \mu,\, \tau\}$
Lepton neutrinos	$\{\nu_e,\, \nu_\mu,\, \nu_\tau\}$
Up-type quarks	$\{u,\, c,\, t\}$
Down-type quarks	$\{d,\, s,\, b\}$
Force-carrying bosons	
Electromagnetic force carrier	γ
Weak force carriers	$Z,\, W^\pm$
Strong force carrier	g

Table 1.1: Particle content of the standard model. The three generations of fermions (upper table) and the force-carrying bosons (lower table).

mass is the top quark, t. It is the production of these massive top quarks that is the main focus of this thesis.

In order to study the top quark, we must understand how it interacts with other particles of the standard model. In particular, we must consider its interactions with other coloured particles via the strong force. The theory describing strong interactions, the interactions of quarks and gluons, within the standard model is known as *quantum chromodynamics* (QCD). This will be introduced in Chapter 2.

1.2 The Top Quark

The top quark is the third generation up-type quark. It was discovered in 1995 by the CDF and D0 collaborations at the Fermilab Tevatron [3, 4]. It is the heaviest known fundamental particle. Due to its large mass, it can only be produced if a large amount of energy is present in a collision. At present, the only colliders which can produce sufficient energy are the Fermilab Tevatron and CERN's Large Hadron Collider (LHC).

The Tevatron operates with a centre-of-mass (CoM) energy of 1.96 TeV for run II, while the LHC has a design CoM energy of 14 TeV, although it is currently operating at 7 TeV. The large increase in CoM energy from the Tevatron to the LHC leads to a vast increase in the production rate of top quarks. This will allow us to explore the top quark at much greater precision than ever before.

The large mass of the top quark gives it some interesting properties and also gives us the ability to explore some standard model and even beyond-standard-model phenomena [5]. Having such a large mass, the top quark decays before it can form hadronic bound states. This is a unique property amongst the quarks and it allows us to investigate the interactions of a 'free' quark. Of particular interest are the spin-correlation effects. When a light quark undergoes hadronisation, it experiences non-perturbative strong-interaction effects and its spin information is lost. As the top quark decays before hadronisation, however, its spin information is preserved. Thus, by observing angular distributions of its decay products, a bottom quark and a W-boson, we can explore the spin structure of the Wtb-vertex and the production dynamics of the top quark [6, 7].

By studying the top quark, we can also gain information on some of its other properties, for example, its mass, m_t, and obtain a direct measurement of the CKM matrix element, V_{tb}. This can be used to test the unitarity of the CKM matrix [8]. Top-quark production processes also constitute an important background to Higgs-boson searches [5], and thus a thorough understanding of their cross sections is desirable.

There are two ways in which top quarks can be produced at hadron colliders; singly, with only a single top or anti-top being produced, or as a top anti-top pair. Example Feynman diagrams of each process are shown in Figure 1.1. The cross section of top-pair production ($\sim$ 160 pb for the 7 TeV LHC, $\sim$ 7 pb for run II at the Tevatron) is
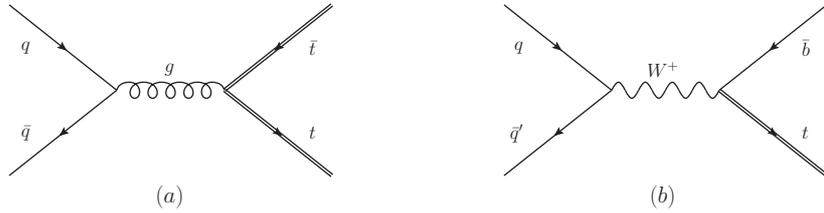
Figure 1.1: Example Feynman diagrams showing top-pair production (a) and single-top production (b).

greater than that of single-top production ($\sim$ 50 pb for the 7 TeV LHC, $\sim$ 1.5 pb for run II at the Tevatron) [9]. Single-top production contains one less final-state particle, after the decay of the top quarks has been included, however, and provides a natural starting point for the calculation. Single-top production is also a background to top-pair production, and thus, knowledge of its cross section will be useful when studying top-pair events. The production of a single top-quark at both the Tevatron and the LHC will be considered in this thesis.

1.3 Single-Top Production

Single top-quark events were first observed by both the CDF and D0 experiments at the Tevatron in 2009 [10, 11]. At the LHC, such events are expected to be observed on a regular basis, allowing them to be investigated to high precision. The production of single top-quarks at hadron colliders occurs via one of three channels; s-channel production, t-channel production and associated-tW production. Example Feynman diagrams of the three production channels are shown in Figure 1.2. The expected total cross sections of the three production channels at the Tevatron and 7 TeV LHC, taken from Refs. [9, 12], are shown in Table 1.2. In both cases, the largest contribution comes from the t-channel process. At the Tevatron this is followed by the s-channel process, with the contribution of the associated-tW process being smallest. At the LHC, how-
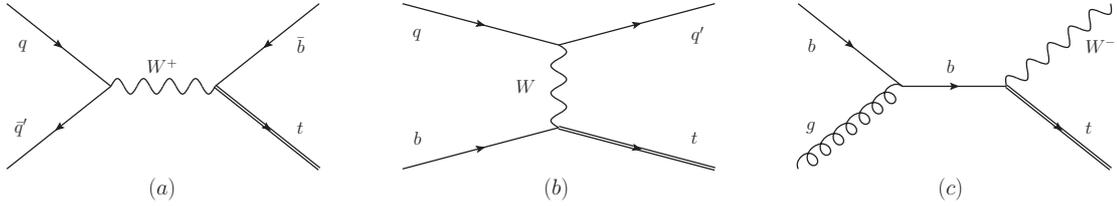
Figure 1.2: Example Feynman diagrams showing the three single-top production channels. From left to right: s-channel production, t-channel production, associated-tW production.

Cross section [pb]	s-channel	t-channel	Associated-tW
Tevatron	0.52	1.04	0.14
7 TeV LHC	3.2	41.7	7.8

Table 1.2: Approximate total cross sections for the three single-top production channels at the Tevatron and the 7 TeV LHC at next-to-next-to-leading order [9, 12].

ever, the associated-tW process provides the second largest contribution. If we want to calculate cross sections to next-to-leading order (NLO), the existence of these three distinct production channels becomes blurred. While associated-tW production has its own specific final state, the s- and t-channel production processes can give rise to the same final state and thus become entangled. For the calculation presented in this thesis we will ignore the associated-tW contribution, instead concentrating on the larger contribution of the t-channel process and, due to entanglement at NLO, the s-channel process.

In order to calculate the cross section of single top-quark production, or the production of any unstable heavy-particle, we must first decide how to treat this particle. There are a number of different treatments which can be used. Details of these treatments are given in Section 3.4. Here, we will briefly mention each method. The most straightforward method is to treat the heavy particle as a stable particle and ignore its decay. This method requires calculating the amplitudes of the production diagrams

only. These have fewer final state particles than the full process and thus are easier to calculate. We lose any information about the decay products, however. The second method is to treat the process as the production of an on-shell heavy-particle, followed by its decay. The two subprocesses are joined using the narrow-width approximation (NWA). When using this method, the NLO corrections to each subprocess are calculated separately and we are able to extract some information from, and make kinematical cuts on, the decay products. The final method is to consider the entire process, production and decay, as a whole. In this framework, the heavy particle appears only in an intermediate state and, therefore, it is not required to be on-shell. By considering the process as a whole, NLO processes which link the production and decay subprocesses must also be included. The one-loop corrections can be split, in a gauge-invariant way, into *factorisable* and *non-factorisable* contributions [13, 14]. The factorisable contributions can be assigned to either the production or decay subprocess and are analogous to those of the NWA treatment. The non-factorisable corrections link the production and decay subprocesses and provide an additional correction to the NWA treatment. We shall refer to the differences between the off-shell treatment and the NWA treatment, i.e. the effects due to the heavy particle not being constrained to be on its mass shell and the non-factorisable NLO diagrams, as the off-shell effects. Calculating these off-shell effects to s- and t-channel single-top production will be the main focus of the thesis.

Using the off-shell treatment of the top quark, the calculation consists of a Taylor expansion of the amplitudes in a small parameter, δ, followed by an asymptotic expansion of any loop integrals. The expansion in δ encompasses the standard perturbative expansion in the coupling constants, along with an additional expansion in the virtuality of the top quark, $p_t^2 - m_t^2$, which we require to be small. That is, while not requiring

that the top quark is on-shell, we require that it is close to its mass shell, or *resonant**.
The expansion in the virtuality of the top quark follows a similar methodology to the
pole approximation [15, 16], employing effective-theory (ET) inspired techniques akin
to those in Refs. [17, 18, 19]. These involve splitting the loop integrals into components
using the method of regions [20, 21] and expanding within each region separately. For
the real corrections, we choose to deviate from the strict ET approach in order to ensure
the inclusion of all relevant contributions whilst retaining the correct pole structure to
enable exact cancellation with the poles arising in the virtual corrections. After expan-
sion in δ, we can easily determine the contributions that are relevant to the calculation
up to a certain order. Contributions beyond this order can be neglected, leading to a
simplification of the final calculation. The application of the method outlined above is
discussed in Ref. [22] and will also be discussed, in much greater detail, in Chapters 4
and 5.

Throughout the calculation, quark-mixing effects will be ignored, that is the CKM
matrix will be considered diagonal, and all quarks except the top quark will be treated
as massless. We use the 5-flavour scheme, allowing bottom (and anti-bottom) quarks
to be emitted from the incoming hadrons.

1.4 Existing Calculations

Single-top production has been studied extensively in the existing literature. Here, an
overview of the current status of calculations will be given.

When considering the production of a stable top-quark, calculations for all three
production channels are available at NLO in QCD in Ref. [23], with those for t-channel

---

*$p_t^2 - m_t^2 \sim m_t \Gamma_t$.

production also in Refs. [24, 25, 26] and for s-channel and associated-tW production in Refs. [27, 28]. The full electroweak corrections are available, for s- and t-channel production, in Refs. [29, 30]. Soft-gluon corrections beyond NLO have also been studied in, for example, Refs. [31, 32, 33, 34]. Results including the top-quark decay via the narrow-width approximation can be found in Refs. [35, 36, 37, 38, 39, 40]. Calculations using the off-shell heavy-particle treatment have been presented for s-channel single-top production only [41], top-pair production [42] and $e^+e^- \to WW \to$ four fermions [14]. These off-shell effects are known to be small for observables which are inclusive enough in the invariant-mass of the top quark [43, 44]. This is a result of cancellations between the finite parts of the real and virtual contributions to the process at NLO. There could be cases where this cancellation is affected by the introduction of kinematical cuts, however, leading to more substantial effects.

The effects of a non-diagonal CKM matrix on the rapidity distribution of the top quark can be found at LO in Ref. [45], and at LO and NLO in [46]. The effects of a non-zero bottom-quark mass and the differences between using the 4-flavour and 5-flavour scheme can be found in Refs. [47, 48].

1.5 Thesis Outline

The remainder of this thesis will focus on the calculation of cross sections and kinematic distributions for single top-quark production via the s- and t-channels at both the Tevatron and the LHC.

In Chapter 2 a brief overview of perturbative QCD is presented. This includes the Feynman Rules of QCD, renormalisation and counterterms.

Chapter 3 reviews the basic method used for the calculation of a general cross section at both leading and next-to-leading order. This includes factorisation, parton distribution functions and a discussion of the problems associated with the singularities that arise in these calculations and how they are resolved. The various possible treatments of heavy particles are also given, and their respective merits and failings considered. The chapter ends with an introduction to the helicity notation.

In Chapter 4 our method for treating unstable heavy-particles is outlined. This is presented as an example of its application to t-channel single-top production, but the discussion should be such that its general application to any process follows naturally.

Chapter 5 illustrates more thoroughly the application of the method outlined in Chapter 4 to t-channel single-top production. Helicity amplitudes for the contributing Feynman diagrams are given and the cancellation of poles is shown explicitly. The chapter closes with a comparison of our results to some of those existing in the literature.

Chapter 6 contains results, calculated using the off-shell treatment of the top quark, for s- and t-channel single-top production at both the Tevatron and the 7 TeV LHC. Results calculated using the narrow-width approximation treatments of the top quark are included for comparison and to allow the size of the off-shell and spin-correlation effects to be calculated. A discussion of the ambiguity of the s- and t-channel production mechanisms at next-to-leading order is also presented.

In Chapter 7 the thesis is summarised, conclusions are drawn, and further possible applications of, and improvements to, our method are considered.

Chapter 2

Quantum Chromodynamics

In order to study processes involving the top quark, and any other quarks or gluons, we require a theory which governs the interactions of particles which carry colour charge. This theory is known as *quantum chromodynamics* (QCD). In this chapter, the Lagrangian density and associated Feynman rules of QCD will be introduced, and the renormalisation and counterterms of the theory briefly discussed.

2.1 The QCD Lagrangian

The Lagrangian density* of QCD, $\mathcal{L}_{\text{QCD}}$, is comprised of four parts;

$$\mathcal{L}_{\text{QCD}} = \mathcal{L}_{\text{quark}} + \mathcal{L}_{\text{gluon}} + \mathcal{L}_{\text{gauge-fixing}} + \mathcal{L}_{\text{ghost}} . \tag{2.1}$$

This equation gives a general, renormalisable description of the interactions between quark fields and gluons. Quarks and gluons both carry colour charge and must therefore

---

*From this point onwards referred to as the Lagrangian.

be represented by fields in colour space. Quarks transform according to the fundamental representation of $SU(3)$ and comprise a triplet of fields, q^a, where $a \in \{\mathrm{r}, \mathrm{g}, \mathrm{b}\}$ is the colour index. Gluons transform according to the adjoint representation of $SU(3)$ and comprise an octet, A_μ^A, where the superscript A is the colour index in the adjoint representation and can take any of the eight unique gluon colour values. The subscript μ is a Lorentz index[†].

The quark-field Lagrangian is derived from the Dirac Lagrangian for a free field with the requirement that the quark fields are locally gauge invariant. This derivation is widely available in the literature, see Ref. [49], for example, and gives

$$\mathcal{L}_{\text{quark}} = \sum_i \bar{q}_i^a \left(i D^\mu \gamma_\mu - m_i \right)_{ab} q_i^b. \tag{2.2}$$

Here, the subscript i denotes the flavour of the quark; $(m_i)_{ab} = m_i \delta_{ab}$ is the mass of the quark; γ_μ are the Dirac matrices, which obey the Clifford algebra,

$$\{\gamma^\mu, \gamma^\nu\} \equiv \gamma^\mu \gamma^\nu + \gamma^\nu \gamma^\mu = 2 g^{\mu\nu}; \tag{2.3}$$

and D_{ab}^μ is the covariant derivative, defined as

$$D_{ab}^\mu = \partial^\mu \delta_{ab} - i g_s A_A^\mu t_{ab}^A. \tag{2.4}$$

The QCD coupling is denoted by g_s and t^A are the eight generators of $SU(3)$ in the fundamental representation. The gluon Lagrangian is given by

$$\mathcal{L}_{\text{gluon}} = -\frac{1}{4} F_A^{\mu\nu} F_{\mu\nu}^A, \tag{2.5}$$

[†]Throughout the thesis, Greek letters will indicate Lorentz indices, lower case Latin letters will indicate colour indices in the fundamental representation and upper case Latin letters colour indices in the adjoint representation. Repeated indices indicate that they are summed over.

where $F_{\mu\nu}^A$ is the field-strength tensor, with

$$F_{\mu\nu}^A = \partial_\mu A_\nu^A - \partial_\nu A_\mu^A + g_s f^{ABC}(A_\mu)_B(A_\nu)_C \,. \tag{2.6}$$

The term f^{ABC} denotes the totally anti-symmetric structure constants of $SU(3)$, defined via the equation

$$(T_A)_{BC} = -if_{ABC} \,, \tag{2.7}$$

where T_A are the generators of $SU(3)$ in the adjoint representation. The last two terms in Eq. (2.1) are the gauge-fixing and ghost contributions, calculated by Faddeev and Popov [50]. The gauge fixing term,

$$\mathcal{L}_{\text{gauge-fixing}} = -\frac{1}{2\xi}\left(\partial^\mu A_\mu^A\right)^2 \,, \tag{2.8}$$

is required to ensure that the terms in the Lagrangian which are bilinear in the gluon field can be inverted, in order to define its propagator in the Feynman rules. The addition of this term introduces a dependence on the gauge-fixing parameter, ξ. This parameter may take an arbitrary value. This may initially seem problematic as the Feynman amplitude of a particular diagram would vary dependent on the choice of ξ. However, the calculation of individual Feynman diagrams is, in general, insufficient. We must instead perform the calculation of a full *gauge-invariant* set of diagrams. The ξ-dependence within this set must cancel, leaving our final result independent of our choice of gauge. Although the choice of ξ value is arbitrary, it is generally chosen such that it leads to a simplification of the Feynman rules. The two most popular choices are the Feynman gauge, $\xi = 1$, and the Landau gauge, $\xi = 0$. We will use the Feynman

gauge throughout. The ghost contribution,

$$\mathcal{L}_{\text{ghost}} = -\bar{c}_A \left(\partial_\mu D_{AB}^\mu \right) c^B \, , \tag{2.9}$$

where c^A are ghost fields and

$$D_{AB}^\mu = \partial^\mu \delta_{AB} + g_s f_{ABC} \left(A^\mu \right)^C \, , \tag{2.10}$$

is required to preserve unitarity. The ghost fields do not correspond to real particles and cannot appear as initial-state or final-state particles in Feynman diagrams. Instead, they appear only as intermediate virtual particles. For the calculations presented in this thesis ghost fields are not required and are included here for completeness only.

2.2 Feynman Rules

Now we have the Lagrangian of QCD, we can use this to read off the corresponding Feynman rules of the theory. Ignoring the ghost contributions and working in the Feynman gauge, we can obtain the Feynman rules of QCD by inserting the definitions in Eqs. (2.2)-(2.8) into the QCD Lagrangian and expanding. A selection of these rules, required for the calculations presented in this thesis, are shown in Figure 2.1. Within these expressions, p is the four-momentum of the propagating particle, m is its mass, $\not{p} = p^\mu \gamma_\mu$, and the prescription $i0^+$ in the denominator defines the location of the complex pole of the propagator[‡]. Momentum must be conserved at each vertex. Along with these expressions, there are a number of other rules which must also be applied. Firstly, any undetermined loop-momenta, k, must be integrated over using

---

[‡]From this point onwards, the $i0^+$ in propagator denominators will not be shown. Its presence is understood, however.

Figure 2.1: Selected momentum space QCD Feynman rules in the Feynman gauge. Top: fermion propagator. Centre: gluon propagator. Bottom: fermion-fermion-gluon vertex.

the integration measure, $\int d^4k/(2\pi)^4$. Secondly, any diagram containing a fermion loop must receive an overall prefactor of (-1). Finally, the diagram may require an overall symmetry factor. Details of this can be found in Ref. [49], for example.

2.3 Renormalisation and Counterterms

When performing a QCD calculation at next-to-leading order (NLO), we quickly run into some problems. The theory of QCD suffers from singularities arising from specific kinematic regions. These singularities can be categorised as either *ultraviolet* or *infrared*. The origins of the ultraviolet (UV) singularities will be discussed later in this section. Their removal, along with the origins and removal of the infrared (IR) singularities, will be discussed in Section 3.2.

The UV singularities originate in the parameters of the Lagrangian of the theory. These parameters; the quark masses, quark fields, couplings, etc. correspond to the

measurable physical-parameters at tree level only. At higher orders, this is not the case. Instead, these parameters are the *bare parameters* of the theory. If we try to calculate physical quantities in terms of these bare parameters, we encounter divergences. In order to obtain finite results for these physical quantities, we must define new parameters, called *renormalised parameters*, which give finite results at any order in perturbation theory. The renormalised quantities (denoted by a superscript r) are related to the bare quantities (denoted by a superscript 0) via equations of the form,

$$X^0 = X^r + \delta X^r \,. \tag{2.11}$$

The renormalisation parameters, δX^r, are fixed via renormalisation conditions and through a choice of renormalisation scheme. Here, we present only the details required for our calculation. We write our bare masses and fermion wavefunctions as

$$m^0 = m^r + \delta m^r \,, \qquad q^0 = q^r \left(1 + \frac{\delta Z^r}{2} \right) \,. \tag{2.12}$$

We will use the *on-shell* renormalisation scheme (OS) for masses throughout. In this scheme, the renormalised mass is chosen such that the pole of the physical propagator is located at $p^2 = (m^{\mathrm{OS}})^2$. From this, it follows that massless fermions have no mass renormalisation, $\delta m_i^{\mathrm{OS}} = 0$. Massless fermion fields also require no wavefunction renormalisation, $\delta Z_i^{\mathrm{OS}} = 0$. The subscript i in these expressions denotes a massless fermion. Because of this, for our calculation we need consider only the top-quark wavefunction and mass renormalisation parameters, δZ_t^{OS} and δm_t^{OS}. These can be extracted from

$$i\left((\not{p}_t - m_t^r)\delta Z_t^r - \delta m_t^r\right)$$

$$i\frac{\delta Z_t^r}{2}\frac{g_{ew}}{\sqrt{2}}\gamma^\mu\frac{1}{2}\left(1 - \gamma_5\right)$$
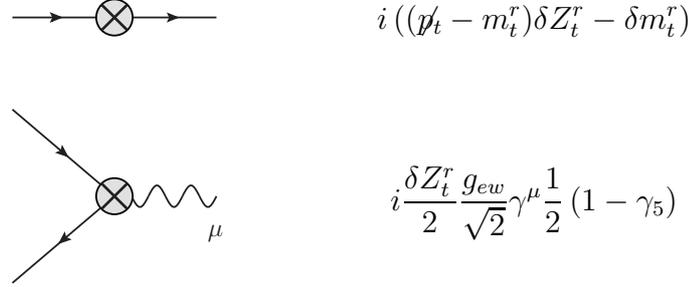
Figure 2.2: Selected counterterm diagrams with their associated Feynman rules [51]. Top: self-energy counterterm of the top quark. Bottom: Wtb-vertex counterterm.

the top-quark self-energy, $\bar{\Sigma}_t(\not{p}_t)$, via the equations

$$\delta m_t^{\mathrm{OS}} = -\bar{\Sigma}_t(m_t^{\mathrm{OS}})\,, \tag{2.13}$$

$$\delta Z_t^{\mathrm{OS}} = \frac{\partial\bar{\Sigma}_t}{\partial\not{p}_t}(m_t^{\mathrm{OS}})\,. \tag{2.14}$$

More details regarding this can be found in Sections 4.2 and 5.4, and in Appendix A. The renormalised strong coupling, g_s, gains a dependence on an additional energy scale, known as the *renormalisation scale*, μ_R. Details of this are widely available in the literature and will not be discussed here.

Substituting in the expressions for the bare parameters into the bare Lagrangian, we obtain

$$\mathcal{L}^0 = \mathcal{L}^r + \delta\mathcal{L}^r\,, \tag{2.15}$$

where $\mathcal{L}^0$ and $\mathcal{L}^r$ have the same form as Eq. (2.1), with the corresponding superscripts added, and $\delta\mathcal{L}^r$ contains the extra terms, known as the counterterms. Terms of order $(\delta m^r)^2$, $(\delta Z^r)^2$ and higher in the counterterm Lagrangian are neglected at NLO. As the renormalised Lagrangian has the same form as Eq. (2.1), the corresponding Feynman

rules have the same form as those in Section 2.2, but with renormalised parameters instead of bare parameters. The counterterm Lagrangian gives rise to counterterm diagrams which must be included, along with the usual Feynman diagrams, at NLO. The counterterm diagrams required for the calculations presented in this thesis are shown in Figure 2.2. They are the top-quark self-energy counterterm diagram and the counterterm correction to the vertex joining two quarks to a W-boson, specifically, in our case, the Wtb-vertex correction. The γ_5 appearing in the expression for the Wtb-vertex counterterm is the fifth Dirac gamma matrix. This arises due to the chiral nature of the W-boson.

Chapter 3

Calculation of Cross Sections

If we consider the calculation of the cross section of a general scattering process at a hadron collider, we are naturally led to confronting the topics of factorisation, regularisation and subtraction. These are key issues in any loop-based QCD cross-section calculation. We will also discuss various possible treatments of unstable heavy-particles and briefly introduce the helicity notation for calculating amplitudes.

3.1 Factorisation and PDFs

The method used to obtain the cross section of a general QED scattering process is well understood. All possible contributing Feynman diagrams are drawn, the appropriate Feynman rules are applied and the integration over loop momenta and phase space carried out. However, as we move to consider QCD processes, we quickly run into problems caused by confinement. In QED, the external states of the scattering process are QED particles with well known Feynman rules describing them. In QCD, however, the external states are hadrons; bound states of quarks and anti-quarks. In
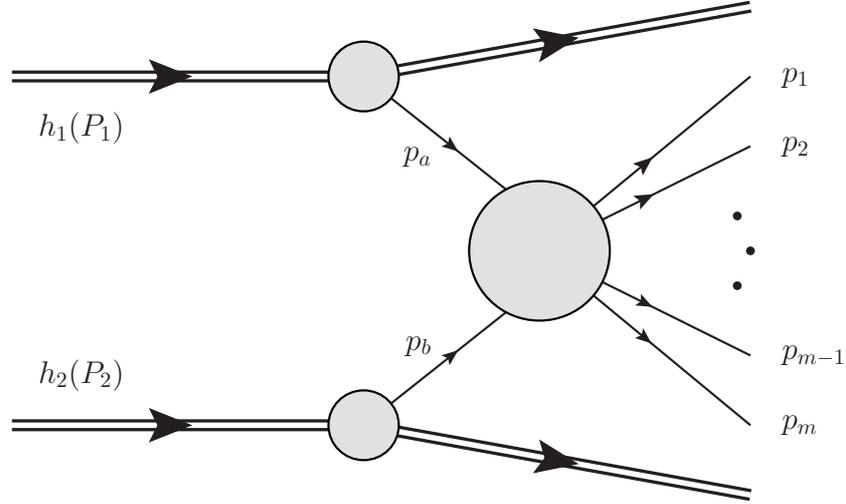
Figure 3.1: A general hadronic process. Two incoming hadrons, h_1 and h_2, emit two partons, carrying momenta p_a and p_b, which then undergo hard scattering producing m final-state particles.

order to consider the scattering of a QCD particle, or *parton*, therefore, we must first consider how we obtain the parton from the bound state containing it. Similarly, outgoing partons are not observed on their own; rather, they are seen as jets of hadrons propagating in the direction of the scattered parton. To combat these problems, we use the theorem of *factorisation* [59, 60]. This allows us to split up the process according to the energy scale involved. We can write the cross section of the general hadronic process, shown in Figure 3.1, as follows;

$$\sigma\left(h_1 h_2 \to X\right) = \sum_{a,b} \int_0^1 dx_1 \int_0^1 dx_2 \; f_{a(h_1)}\left(x_1, \mu_F\right) f_{b(h_2)}\left(x_2, \mu_F\right) \hat{\sigma}_{ab}\left(X\right) , \qquad (3.1)$$

where, at leading order (LO),

$$\hat{\sigma}_{ab}^{\mathrm{LO}} = \int_m d\sigma_{ab}^B = \int d\Phi^{(m)} \mathcal{M}_{ab}^{\mathrm{tree}}\left(p_a, p_b; p_1 \ldots p_m\right) \mathcal{J}^{(m)}\left(p_1 \ldots p_m\right) . \qquad (3.2)$$

Here, $d\Phi^{(m)}$ is the m-particle phase space, $\mathcal{M}_{ab}^{\mathrm{tree}}$ is the LO tree-level, or Born, squared matrix-element of the partonic scattering process, and $\mathcal{J}^{(m)}$ is the m-particle jet-

defining function. The next-to-leading order (NLO) contributions will be discussed later in the chapter. The sum is over all possible initial-state partons, a and b, which can give rise to the final-state configuration, X. The momenta p_a and p_b are related to the momenta of the incoming hadrons, P_1 and P_2, via the expressions $p_a = x_1 P_1$ and $p_b = x_2 P_2$.

There are two parts to the factorisation of the process: Eq. (3.1) shows the initial-state factorisation, while Eq. (3.2) shows the inclusion of jets. In the initial state, the process is split into a hard scattering of partons a and b into a final state X, that can contain QED particles, QCD jets or a combination of the two, $\hat{\sigma}_{ab}(X)$, multiplied by two *parton distribution functions* (PDFs). The PDFs, denoted by $f_{p(h)}(x, \mu_F)$, give the probability of finding a parton, p, emitted from a hadron, h, carrying a fraction, x, of the hadron's momentum. The parameter μ_F is called the *factorisation scale*. This split is possible due to the different energy scales relevant in the process. The parton-parton scattering occurs at high energies, also known as the hard scale, where perturbation theory is valid. The cross section of this *hard scattering* can be calculated using the standard perturbative approach of Feynman diagrams and rules, outlined for QCD in Chapter 2. Interactions occurring at lower energies are described by the PDFs. The cut-off energy, below which interactions are absorbed into the PDFs, is given by the factorisation scale, μ_F. The PDFs include both perturbative and non-perturbative effects and are derived from a combination of experimental data and theoretical predictions. A number of PDF sets are available to be used in calculations. Some examples can be found in Refs. [52, 53, 54, 55]. The results presented in this thesis were all calculated with the MRST2002 [52] or MSTW2008 [55] PDF sets.

The hard scattering of initial-state partons to final-state particles and jets can itself be split into a hard scattering to final-state particles and partons multiplied by

a jet-defining function, as shown in Eq. (3.2). The hard scattering of the incoming partons, a and b, to m final-state particles and partons is calculated via the squared matrix-element, $\mathcal{M}_{ab}(p_a, p_b; p_1 \ldots p_m)$, which is derived from amplitudes calculated using Feynman rules[*]. This is then multiplied by the m-particle jet-defining function, $\mathcal{J}^{(m)}(p_1 \ldots p_m)$, which takes the m outgoing particles and combines any partons into jets according to certain criteria applied to their momenta. Exact details of the jet definition used to obtain our results are given in Appendix B.

By splitting the process up in this way, the calculation of the hard-scattering cross section follows the same method as that for a QED process, which is well understood. The inclusion of PDFs and jet definitions is then fairly straightforward.

3.2 Ultraviolet and Infrared Divergences

In the previous section, the general expression for the hard-scattering cross section of a process at LO was given in Eq. (3.2). At this order, the integral over phase space is finite and the calculation proceeds in a straightforward manner. However, if we want to extend our calculation to NLO, we encounter some problems with the integrals. The general form of the NLO hard-scattering cross section is

$$\hat{\sigma}_{ab}^{\mathrm{NLO}} = \int_m d\sigma_{ab}^V + \int_{m+1} d\sigma_{ab}^R + \int_m d\sigma_{ab}^C, \tag{3.3}$$

where

$$\int_m d\sigma_{ab}^V = \int d\Phi^{(m)} \mathcal{M}_{ab}^{\mathrm{Virtual}}(p_a, p_b; p_1 \ldots p_m)\, \mathcal{J}^{(m)}(p_1 \ldots p_m) \tag{3.4}$$

---

[*]$\mathcal{M}_{ab} = |\mathcal{A}_{ab}|^2$.
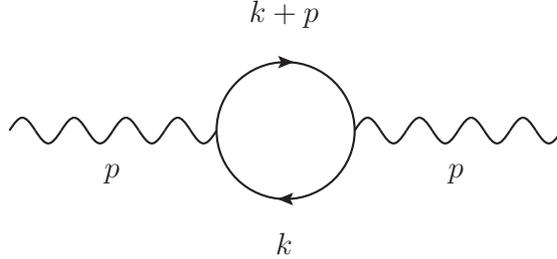
Figure 3.2: A Feynman diagram containing a massless-fermion loop. Labels represent the four-momenta of the particles.

and

$$\int_{m+1} d\sigma_{ab}^R = \int d\Phi^{(m+1)} \mathcal{M}_{ab}^{\text{Real}} \left(p_a, p_b; p_1 \ldots p_{m+1} \right) \mathcal{J}^{(m+1)} \left(p_1 \ldots p_{m+1} \right) \qquad (3.5)$$

are the virtual and real contributions respectively. The virtual matrix element is given by

$$\mathcal{M}_{ab}^{\text{Virtual}} = 2 \, \text{Re} \left[\mathcal{A}_{ab}^{1-\text{loop}} \left(\mathcal{A}_{ab}^{\text{tree}} \right)^* \right] , \qquad (3.6)$$

where the amplitude, $\mathcal{A}_{ab}^{1-\text{loop}}$, contains all one-loop diagrams relevant to the process. The real squared matrix-element, $\mathcal{M}_{ab}^{\text{Real}}$, contains all diagrams with an extra parton in the final state. The third term, $\int_m d\sigma_{ab}^C$, known as the collinear counterterm, arises due to the presence of hadrons in the initial state. Its exact form is not required at this stage, but its singularity structure will be considered.

If we first consider the virtual contributions to the NLO cross section, these arise from the Feynman diagrams of the process which contain one closed momentum loop. The momentum which flows in this loop, which we will call the loop momentum, k, can take any value and, in accordance with the Feynman rules, must be integrated over. If we take the simple case of a massless-fermion loop, shown in Figure 3.2, and apply

Feynman rules, we see that the amplitude has the form

$$\mathcal{A} \sim \int \frac{d^4 k}{(2\pi)^4} \frac{1}{k^2 (k+p)^2} \, . \tag{3.7}$$

This integral diverges both as $k \to \infty$ and as $k \to 0$. The singularities coming from the region $k \to \infty$ are the ultraviolet (UV) singularities, while those coming from $k \to 0$ are the infrared (IR) singularities. For our cross section to make physical sense, these singularities must be removed. The methods for achieving this differ for UV and IR singularities. For both, however, we first need to make the singularities explicit. This involves a process known as *dimensional regularisation*. This method, devised by 't-Hooft and Veltman [56, 57], involves changing the number of space-time dimensions from 4 to $4 - 2\epsilon$. This allows the integration to be carried out analytically, leaving the singularities explicit as powers of $1/\epsilon$. Once the singularities have been removed, the parameter ϵ is set to zero and we recover a 4-dimensional result. The removal of UV divergences comes through renormalisation, as discussed in Section 2.3. For the bubble diagram, shown in Figure 3.2, we obtain [58], using dimensional regularisation,

$$\mathcal{A} \sim \int \frac{d^{4-2\epsilon} k}{(2\pi)^{4-2\epsilon}} \frac{1}{k^2 (k+p)^2} \sim \left(\frac{\mu_R^2}{-p^2} \right)^\epsilon \left(\frac{1}{\epsilon} - \gamma_E + \log(4\pi) + 2 \right) + \mathcal{O}(\epsilon) \, , \tag{3.8}$$

where μ_R is the renormalisation scale and γ_E is the Euler-Mascheroni constant. This can be rewritten as

$$\mathcal{A} \sim \int \frac{d^{4-2\epsilon} k}{(2\pi)^{4-2\epsilon}} \frac{1}{k^2 (k+p)^2} \sim \left(\frac{\mu_R^2}{-p^2} \right)^\epsilon \left(\frac{1}{\bar{\epsilon}} + 2 \right) + \mathcal{O}(\epsilon) \, , \tag{3.9}$$

with the $\bar{\epsilon}$-pole defined as

$$\frac{1}{\bar{\epsilon}} = \frac{1}{\epsilon} e^{-\epsilon \gamma_E} (4\pi)^\epsilon \, . \tag{3.10}$$
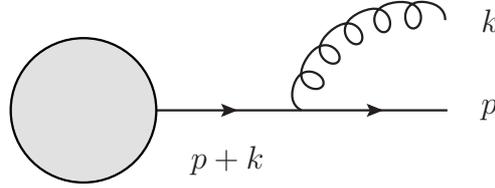
Figure 3.3: A Feynman diagram showing gluon emission off an outgoing-quark leg. Labels represent the four-momenta of the particles.

Before we can set $\epsilon \to 0$, we must remove the singularities. As the UV singularity structure coming from the associated counterterms exactly cancels that of the loop diagrams at each order in perturbation theory, we can subtract the $1/\epsilon$ terms, along with any arbitrary constants, from the expression. As long as the subtraction is performed consistently for all loop diagrams and counterterms, the final results will be identical. We will use the modified minimal-subtraction scheme ($\overline{\text{MS}}$) which involves subtracting the term $1/\bar{\epsilon}$ and, if present, any higher-order $\bar{\epsilon}$-poles. Once all UV singularities have been removed, we are still left with the IR singularities. To understand how these are cancelled we must move on to look at the real contributions to the NLO cross section.

The real contributions to the NLO cross section arise from Feynman diagrams containing an extra parton in the final state. As an example, let us consider an extra gluon being emitted from an external massless-quark leg, as shown in Figure 3.3. The matrix element gains an extra propagator representing the intermediate massless-quark before it emits the gluon. This leads to a factor in the amplitude of the form

$$\mathcal{A} \sim \frac{1}{(p+k)^2} = \frac{1}{2p \cdot k}. \tag{3.11}$$

This amplitude is IR divergent as it becomes singular when the denominator tends towards zero. This can occur either when $k \to 0$, known as the gluon becoming soft, or when $p \cdot k \to 0$, which is referred to as the quark and gluon becoming collinear. In

order for our cross section to be finite, we require these IR divergences to exactly cancel those of the virtual contribution. After calculating, we find that the IR divergences of the real contribution do successfully cancel those of the virtual contribution. There are some left over, however. The IR divergences due to collinear emission off an initial-state parton remain. To see how these are removed, we must return to the PDFs defined in the previous section. As we move from a LO to a NLO calculation, it is not only new matrix elements we have to calculate; the PDFs also change. At NLO, the redefined PDFs contain IR singularities. By factorising our remaining initial-state collinear singularities, they can be absorbed into the PDF functions. The finite remainder of this factorisation is given by the collinear counterterm contribution to the NLO cross section. The exact form of this contribution will be given later.

It has been proved that the cancellation of the IR divergences is general, to all orders in perturbation theory, for infrared-safe quantities [61, 62, 63]. This allows us to perform NLO cross section calculations.

3.3 The Subtraction Method

As discussed in Section 3.2, the cancellation of divergences in an NLO calculation is well understood. The practicalities of this cancellation when performing a calculation, however, are more troublesome. The difficulty of the phase space integrals required in a cross section calculation makes solving them analytically all but impossible, except in the simplest of cases. Instead, the integrals are carried out numerically using Monte Carlo techniques. Using numerical integration requires us to treat the integrals over m and $(m + 1)$ final-state particle phase space separately. In other words, we have to treat the virtual and real contributions individually. As discussed in the previous

section, however, these two pieces are separately divergent. We need a way of making these two contributions finite while explicitly cancelling out the poles. This is achieved by introducing a term which is subtracted from the real contribution, cancelling its divergent behaviour, and added back to the virtual contribution, explicitly cancelling the poles present in that part. The two most popular of these *subtraction methods* are Catani-Seymour dipole subtraction [64] and the method of Frixione, Kunszt and Signer (FKS) [65]. In this thesis we will focus on the Catani-Seymour method.

Catani-Seymour subtraction involves the introduction of a local counterterm, $d\sigma^A$, which, in the $(m+1)$-particle phase space, exactly cancels the IR singularities of the real contribution to the NLO cross section, $d\sigma^R$, and also, after integration over the phase space of a single particle, exactly cancels the explicit IR singularities appearing in the virtual contribution, $d\sigma^V$. We redefine our NLO hard-scattering cross section as

$$\hat{\sigma}_{ab}^{\text{NLO}} = \int_{m+1} \left(d\sigma_{ab}^R - d\sigma_{ab}^A\right)_{\epsilon=0} + \int_m \left(d\sigma_{ab}^V + d\sigma_{ab}^C + \int_1 d\sigma_{ab}^A\right)_{\epsilon=0}. \qquad (3.12)$$

The integral of $d\sigma^A$ over the single-particle phase space can be performed analytically, giving explicit ϵ-poles which exactly cancel those in $d\sigma^V$. After this cancellation, we can set $\epsilon = 0$ and perform the numerical integration. The integrals over both the $(m+1)$- and m-particle phase space are now finite. The local counterterm is defined in terms of *dipoles*,

$$d\sigma^A = \sum_{\text{dipoles}} d\sigma^B \otimes \left(dV_{\text{dipole}} + dV'_{\text{dipole}}\right), \qquad (3.13)$$

where the subscript ab has been omitted for ease of reading. This equation is very general as the exact form of the Born cross section, $d\sigma^B$, and the convolution contain the exact details of the process. The dipole functions are universal. The dV_{dipole} dipoles

exactly match the behaviour of $d\sigma^R$ in final-state soft and/or collinear regions, whereas the dV'_{dipole} dipoles match the initial-state collinear singularities. Integrating Eq. (3.13) over the single-particle phase space yields two terms. The first term,

$$\sum_{\text{dipoles}} d\sigma^B \otimes \int_1 dV_{\text{dipoles}} = d\sigma^B \otimes \boldsymbol{I} \,, \tag{3.14}$$

gives us the universal factor, $\boldsymbol{I}$. This term contains all the explicit singularities required to cancel those appearing in $d\sigma^V$. The second term combines with the collinear counterterm, $d\sigma^C$, to give the finite remainder from the factorisation of the initial-state collinear singularities into the redefined PDFs.

Combining these results, we can rewrite the NLO hard-scattering cross section as

$$\hat{\sigma}_{ab}^{\text{NLO}}(p) = \sigma_{ab}^{\text{NLO}(m+1)}(p) + \sigma_{ab}^{\text{NLO}(m)}(p) + \int_0^1 dz \; \tilde{\sigma}_{ab}^{\text{NLO}(m)}(zp, z; \mu_F) \,, \tag{3.15}$$

where, dropping the ab subscript,

$$\sigma^{\text{NLO}(m+1)}(p) = \int_{m+1} \left[d\sigma^R(p) - \sum_{\text{dipoles}} d\sigma^B(p) \otimes \left(dV_{\text{dipole}} + dV'_{\text{dipole}} \right) \right]_{\epsilon=0} \tag{3.16}$$

is the finite integral comprising the real contributions with the appropriate dipoles subtracted;

$$\sigma^{\text{NLO}(m)}(p) = \int_m \left[d\sigma^V(p) + d\sigma^B(p) \otimes \boldsymbol{I} \right]_{\epsilon=0} \tag{3.17}$$

is the finite integral comprising the virtual contributions plus the integrated local counterterm; and

$$\tilde{\sigma}^{\text{NLO}(m)}(zp, z; \mu_F) = \int_m \left[d\sigma^B(zp) \otimes \left(\boldsymbol{P}(zp, z; \mu_F) + \boldsymbol{K}(z) \right) \right]_{\epsilon=0} \tag{3.18}$$

is the finite remainder from the collinear counterterm and the factorisation of initial-state collinear singularities into the redefined PDFs. Note that, as a result of factorising the singularities into the PDFs, the finite remainder has picked up a dependence on the factorisation scale, μ_F. There is also an additional integration over z, which represents a momentum fraction of the initial-state momenta, p. The symbols $\boldsymbol{I}$, $\boldsymbol{P}$ and $\boldsymbol{K}$ are known as the universal insertion operators. As before, these equations are very general with the exact details of the process being contained within the Born cross section and the convolution. Exact expressions for the $\boldsymbol{I}$ insertions relevant to the processes being considered in this thesis are discussed further in Chapter 5 and given explicitly in Appendix D.

We now have all the tools necessary to complete an NLO cross section calculation for a general hadronic process.

3.4 Treatment of Unstable Heavy-Particles

Now we have considered the method for calculating a general cross section, we move on to look at an issue more directly related to the processes we are interested in, namely, the treatment of unstable heavy-particles. There are a number of ways in which we can deal with heavy particles in a calculation, each having some advantages and some disadvantages. If we consider, for illustration, the production of a heavy particle X, of mass m_X, which then decays into two massless particles, Y and Z. For simplicity we will ignore any PDF factors and jet definitions and work, initially, at LO. Four possible expressions for the total cross section, depending on the heavy-particle

treatment chosen, are:

$$\sigma_{\text{stable}} = \text{Br}_{X \to YZ} \, \sigma_{\text{prod}} = \text{Br}_{X \to YZ} \int d\Phi^{\text{prod}} \mathcal{M}_{\text{prod}}(p_X) \,, \qquad (3.19)$$

$$\sigma_{\text{NWA}} = \frac{1}{2\Gamma_X m_X} \int d\Phi^{\text{prod}} \mathcal{M}_{\text{prod}}(p_X) \int d\Phi^{\text{dec}} \mathcal{M}_{\text{dec}}(p_X; p_Y, p_Z) \,, \qquad (3.20)$$

$$\sigma_{\text{iNWA}} = \frac{1}{2\Gamma_X m_X} \int d\Phi^{\text{prod}} \int d\Phi^{\text{dec}} \mathcal{M}_{\text{iNWA}}(p_X, p_Y, p_Z) \,, \qquad (3.21)$$

$$\sigma_{\text{off}-\text{shell}} = \int d\Phi^{\text{off}-\text{shell}} \mathcal{M}_{\text{full}}(\tilde{p}_X, p_Y, p_Z) \,, \qquad (3.22)$$

where $d\Phi$ are phase-space elements and $\mathcal{M}$ are squared matrix-elements. More thorough explanations are given in the descriptions of the individual processes.

The simplest method is to produce the heavy particle, X, on its mass shell, assume it is stable and let it propagate. Any subsequent interactions, such as its decay into particles Y and Z, can then be treated separately. This factorisation of the process simplifies the calculation, but we lose information. The most basic case, given in Eq. (3.19) and shown in diagram (a) of Figure 3.4, is to calculate the cross section for the production of particle X, σ_{prod}, and multiply this by the branching ratio of its decay into Y and Z, $\text{Br}_{X \to YZ}$. The production cross section is given by the integration of its squared matrix-element over the production phase space. While this is the simplest calculation, as it requires only the production matrix-element, it has one large drawback. By using this treatment we have a total lack of information about the decay products. The use of the branching ratio leaves us unable to apply any kinematical cuts on the decay products or to obtain any information about their momenta.
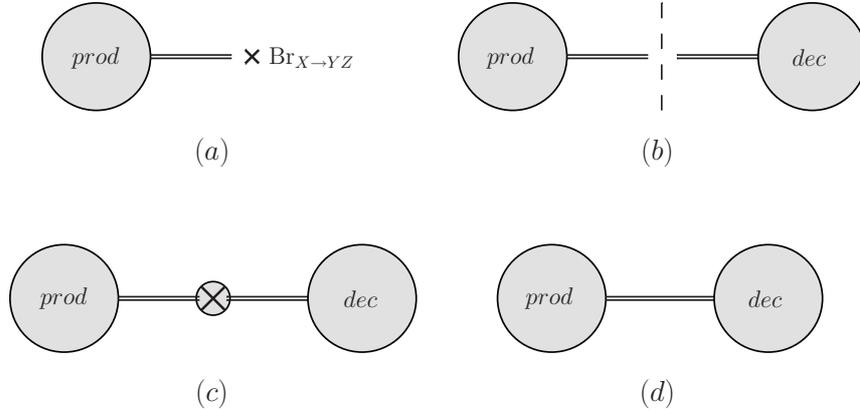
Figure 3.4: Schematic representations of four possible treatments of an unstable heavy-particle. Diagram (a) shows the on-shell stable production of the heavy particle multiplied by the branching ratio of its decay. Diagrams (b) and (c) show the narrow-width approximation and improved narrow-width approximation respectively. Diagram (d) shows the off-shell treatment.

By increasing the complexity of the calculation slightly, we can overcome this problem. Instead of using a branching ratio, we include the squared matrix-element of the decay process, along with that of the production process, using the same momentum for the heavy particle, p_X, in each. We still require the heavy particle to be on-shell, that is $p_X^2 = m_X^2$. The expression for the cross section using this method is given in Eq. (3.20) and a schematic representation is shown in diagram (b) of Figure 3.4. The vertical dotted line is used to show that the production and decay subprocesses can be treated separately but are still linked by the on-shell condition of the heavy particle. To understand where the prefactor $1/(2\Gamma_X m_X)$ arises from, we must consider how we join together the production and decay subprocesses. We cannot simply multiply the production cross section and the decay cross section. As we are joining the processes via the heavy particle, X, we must include its propagator, $1/(\tilde{p}_X^2 - m_X^2 + i\Gamma_X m_X)$, in the amplitude (see Section 4.2 for an explanation of the $i\Gamma_X m_X$ term in the propagator). Including this propagator factor and applying the constraint that the heavy particle is on-shell in both the production and decay squared matrix-elements, the total cross

section is given by ,

$$\sigma_{\mathrm{NWA}} = \int d\Phi^{\mathrm{prod}} \mathcal{M}_{\mathrm{prod}}(p_X) \cdot$$
$$\int \frac{d\tilde{p}_X^2}{(2\pi)((\tilde{p}_X^2 - m_X^2)^2 + \Gamma_X^2 m_X^2)} \int d\Phi^{\mathrm{dec}} \mathcal{M}_{\mathrm{dec}}(p_X; p_Y, p_Z) \,. \tag{3.23}$$

We allow the heavy-particle momentum in the propagator to take any value, $\tilde{p}_X$, where $\tilde{p}_X^2$ is not necessarily equal to m_X^2, and integrate over all possible values. This gives

$$\int_{-\infty}^{\infty} \frac{d\tilde{p}_X^2}{(2\pi)((\tilde{p}_X^2 - m_X^2)^2 + \Gamma_X^2 m_X^2)} = \frac{1}{2\Gamma_X m_X} \,. \tag{3.24}$$

Substituting this into Eq. (3.23), we recover Eq. (3.20). This is known as the *narrow-width approximation* (NWA). This treatment of the heavy particle gives us some information about the decay products, allowing us to administer kinematical cuts and create distributions involving their momenta. By treating the production and decay separately, however, we lose any correlation between the two processes. In order to overcome this problem, we must consider the process as a whole rather than as a production process followed by a decay.

Considering the process as a whole increases the complexity of the matrix elements. They now automatically contain the heavy-particle propagator and we can again choose to treat this in two different ways. The first method uses the same assumptions as those used in the NWA. We manually remove the heavy-particle propagator from the squared matrix-element and require that the heavy particle is on-shell in the remaining expression. We then integrate the propagator over all possible $\tilde{p}_X$ values, as in Eq. (3.24), and we obtain Eq. (3.21). Here, $\mathcal{M}_{\mathrm{iNWA}}$ is the full matrix-element of the process but with the heavy-particle propagator removed and its momentum set on-shell[†]. This treatment is known as the *improved narrow-width approximation* (iNWA). It gives us

---

[†] $\mathcal{M}_{\mathrm{iNWA}} = ((\tilde{p}_X^2 - m_X^2)^2 + \Gamma_X^2 m_X^2) \mathcal{M}_{\mathrm{full}}|_{\tilde{p}_X^2 \to p_X^2} \,.$

all the kinematical information about the decay products and also includes production-decay correlation. A schematic representation of this method is shown in diagram (c) of Figure 3.4. The convolution on the heavy-particle propagator represents the on-shell condition and the fact that the matrix element is for the full process rather than the production and decay subprocesses separately.

The only possible effects left to consider are those which arise from allowing the heavy particle to be off-shell. That is, the heavy-particle momentum is now given by $\tilde{p}_X$, rather than p_X, in the squared matrix-element as well as the heavy-particle propagator. The expression for the total cross section, using this treatment, is given in Eq. (3.22). The off-shell phase space is given by,

$$\int d\Phi^{\text{off}-\text{shell}} = \int d\tilde{\Phi}^{\text{prod}} \int d\tilde{\Phi}^{\text{dec}} \int \frac{d\tilde{p}_X^2}{(2\pi)} \,, \tag{3.25}$$

where $d\tilde{\Phi}$ are the phase spaces for a heavy particle with momentum $\tilde{p}_X$, rather than p_X. The integration over the heavy-particle momentum, $\tilde{p}_X$, must now include the squared matrix-element and the heavy-particle propagator in the integrand, rather than the propagator only, as in the NWA cases. This method is represented by diagram (d) of Figure 3.4.

If we now consider extending this example calculation to NLO, the choice of heavy-particle treatment also affects the number, and the complexity, of Feynman diagrams we need to calculate. This is illustrated in Figures 3.5 and 3.6. Using the stable treatment, we need only consider the NLO diagrams of the production process, shown in the top line of Figure 3.5. For the two NWA treatments, we can consider the NLO contributions to the production and decay subprocesses separately. The full set of these diagrams is shown in Figure 3.5. It is important to note that, as the two processes are linked when using the NWA, when calculating, for example, the NLO contributions to
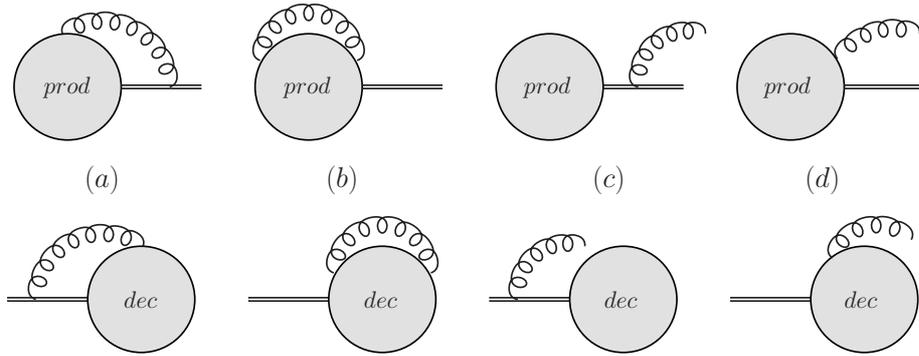
Figure 3.5: Schematic representations of the diagrams required for an NLO heavy-particle calculation using the stable production, NWA and iNWA treatments. The upper line of diagrams represent NLO corrections to the production subprocess, while the lower line of diagrams represents NLO corrections to the decay subprocess. Diagrams (a) and (b) are virtual corrections and diagrams (c) and (d) are real corrections.
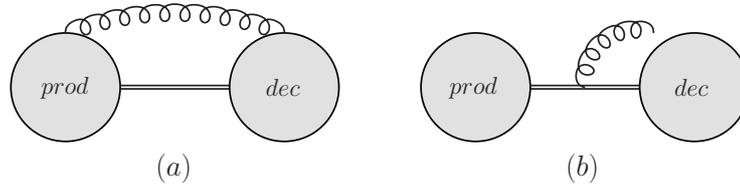
Figure 3.6: Schematic representation of the extra diagrams required for an NLO heavy-particle calculation using the off-shell treatment. Diagram (a) shows the extra virtual diagram which links the production and decay subprocesses. Diagram (b) shows the single real correction which replaces the two real corrections (diagrams (c) of Figure 3.5) present in the NWA treatments.

the production subprocess, the NLO production diagrams must be attached to a LO decay diagram and vice-versa. Attaching the NLO diagrams for each process to one another would give a next-to-next-to-leading order (NNLO) correction. In the final treatment, by allowing the heavy particle to be off-shell, we also allow interferences between the production and decay subprocesses. This leads to an extra class of virtual diagrams, shown in diagram (a) of Figure 3.6, which link the two subprocesses, and to the combination of the two real emission diagrams containing a gluon emitted by the heavy particle, shown in diagrams (c) of Figure 3.5, into a single diagram, (b) in Figure 3.6. It is these off-shell and interference effects that are the main focus of this thesis.

3.5 Helicity Notation

Now we have discussed the general method for calculating the cross section of a hadronic process at NLO, along with the various possible ways of treating any unstable heavy-particles which may appear in the process, the final stage is to calculate the matrix elements of the process. This is done by applying the Feynman rules to all contributing Feynman diagrams of the process. The calculation of these matrix elements, however, quickly becomes computationally intense as we increase the number of external particles. A more efficient way of calculating the matrix elements is to use *helicity amplitudes*. To do this, we fix the spin alignment of all particles in the process. The total squared matrix-element is then just the sum of the squares of each separate helicity state. Terms which mix the states are zero. The lack of these crossed states reduces the computational load of the calculation. As we will see in later chapters, using this method also allows us to write the amplitudes in a fairly compact form. It should be noted that the helicity method, as outlined here, is only valid for massless external

particles. The inclusion of massive external-particles requires a modification of the method and will not be discussed here.

Following the notation of Refs. [66, 67, 68], we define the two helicity states of a massless-fermion wavefunction, $\psi(p)$, according to the two chiral projectors, $\frac{1}{2}(1 \pm \gamma_5)$, where γ_5 is the fifth Dirac gamma matrix. That is,

$$|p\pm\rangle = \psi^\pm(p) = \frac{1}{2}(1 \pm \gamma_5)\,\psi(p)\,, \qquad \langle p\pm| = \overline{\psi^\pm(p)}\,, \tag{3.26}$$

where we have the normalisation

$$\langle p\pm|\gamma_\mu|p\pm\rangle = 2p_\mu\,. \tag{3.27}$$

We introduce the following notation:

$$\langle pq\rangle = \langle p-|q+\rangle\,, \qquad\qquad [pq] = \langle p+|q-\rangle\,, \tag{3.28}$$

$$[p|k|q\rangle = \langle p+|k^\mu\gamma_\mu|q+\rangle\,, \qquad \langle p|k|q] = \langle p-|k^\mu\gamma_\mu|q-\rangle\,. \tag{3.29}$$

The polarisation vectors for external massless bosons, carrying momentum p, are

$$\epsilon_\mu^\pm(p,\eta) = \pm\frac{\langle p\pm|\gamma_\mu|\eta\pm\rangle}{\sqrt{2}\langle\eta\mp|p\pm\rangle}\,, \tag{3.30}$$

where η is an arbitrary, light-like reference momentum. There are a number of identities which can be used to simplify combinations of these helicity states and thus give more compact expressions for the Feynman amplitudes. These identities are readily available in the literature (in Appendix A of Ref. [67], for example) and will not be given here.

The calculation of helicity amplitudes, using the above definitions, follows in a straightforward manner at tree level. However, when we move on to calculate one-loop

helicity amplitudes we encounter a problem. As discussed in Section 3.2, the calculation of loop amplitudes requires a switch from 4 to $4 - 2\epsilon$ space-time dimensions. The γ_5 Dirac matrix, appearing in the chiral projectors, is only well defined in 4-dimensions, however. There are a number of different dimensional regularisation schemes which can be used to overcome this problem. Details can be found in Ref. [69], for example. This is a topic in itself and is not the main focus of this thesis. For our calculations, the important feature to note is that the loop amplitudes will contain a dependence on the scheme chosen for the calculation. This will be explicit in the amplitudes in the form of a regularisation-scheme parameter, x_{sc}. This parameter takes the value $x_{sc} = 0$ in the 't Hooft-Veltman scheme, and $x_{sc} = 1$ in the four-dimensional helicity scheme. For the cross section calculation to be consistent and independent of the scheme chosen, the dependence on x_{sc} must cancel out when all relevant diagrams and contributions are included. This cancellation will be shown explicitly, for our calculations, in Chapter 5.

Chapter 4

Our Method

This chapter provides an overview of the method we use to include the off-shell and production-decay interference effects to processes involving unstable heavy-particles. For clarity, the method is illustrated for t-channel single-top production, however, the discussion will be general enough that its application to an arbitrary process should be apparent.

4.1 Setup of the Calculation

Before beginning any cross section calculation, the first step is to decide on the process to be investigated. We will consider the production of a single top-quark via the t-channel at a hadron collider. Due to the instability of the top quark, we cannot include it as a final-state particle. Instead, we must let it decay to longer-lived particles that could be detected at the collider. In this case, we let the top quark decay into a bottom quark and a W-boson. The W-boson then decays into a lepton and a neutrino. The characteristic final-state of this process contains a bottom-quark jet, a positively

charged lepton and some transverse missing-energy. That is,

$$h_1(P_1)\, h_2(P_2) \rightarrow J_b(p_b)\, l^+(p_l)\, \not{E}_T \,+\, X \,, \tag{4.1}$$

where h_1 and h_2 are the incoming hadrons, J_b is a jet originating from a bottom quark, l^+ is a positively charged lepton, $\not{E}_T$ is the missing transverse-energy of the process, originating from the neutrino, and X represents any additional jets.

There are a number of processes, not just t-channel single-top production, that could produce this final state. For example, if X contained a $\bar{b}$-jet, this final state could come from single-top production via the s-channel. By applying certain vetoes on X we can reduce the number of contributing processes. In this example, we will allow X to contain only light-quark jets, i.e. no b- or $\bar{b}$-jets. This removes the s-channel production contribution as it would contain a $\bar{b}$-jet in its final state[*]. By requiring that there is one, and only one, lepton in the final state and that it has positive charge, we remove the associated-tW production and single-anti-top production processes.

The final, and most important, constraint we apply to the final state is that the intermediate top-quark is resonant, i.e. that its invariant-mass is close to the top-quark mass. The invariant-mass of the top quark is defined as the invariant-mass of its decay products, the W-boson and b-quark,

$$m_{\mathrm{inv}}(t) = \sqrt{(p_t)^2} = \sqrt{(p_b + p_W)^2} = \sqrt{(p_b + p_l + p_\nu)^2} \,. \tag{4.2}$$

The momentum of the W-boson is reconstructed from that of the positive lepton and the transverse missing-energy using the added constraint that the W-boson was on-

---

[*]This is true at LO. However, as we will see in Chapter 6, at NLO the distinction between s- and t-channel becomes distorted. For the discussion of the method we can assume that this cut sufficiently separates the two channels at LO and NLO, however.

shell, $p_W^2 = (p_l + p_\nu)^2 = M_W^2$. Requiring that the top quark is resonant, $(p_t^2 - m_t^2) \sim m_t \Gamma_t \sim \alpha_{ew} m_t^2 \ll m_t^2$, allows the denominator of the intermediate top-quark propagator to become small. This enhances the contribution of diagrams containing an intermediate top-quark, i.e. those which we are interested in, over other background diagrams.

The following sections will outline how we systematically treat this enhancement in order to select only the most numerically important diagrams for calculation, thus reducing the amount of computation required.

4.2 Selection of Diagrams

Once we have a characteristic final-state for the process of interest, we must consider all Feynman diagrams which may contribute. By using factorisation, as discussed in Section 3.1, we can split the process into PDFs, hard-scattering cross sections and a jet-defining function. For our process, we know that we require a b-quark in the final state of the hard-scattering process, to create the b-jet, and also a positively charged lepton and its associated neutrino, to give us the l^+ and transverse missing-energy. We know these particles are the products of the on-shell W-boson decay and, therefore, for simplicity we can initially consider the hard-scattering process containing the W-boson in the final state, before it undergoes its decay. At tree level, our hard-scattering process is

$$q(p_1) \, b(p_2) \to q'(p_3) \, b(p_4) \, W^+(p_W) \to q'(p_3) \, b(p_4) \, l^+(p_5) \, \nu_l(p_6) \,, \tag{4.3}$$

where q is a light quark (u, c) or anti-quark $(\bar{d}, \bar{s})$ coming from one of the hadrons and, accordingly, q' is a quark (d, s) or anti-quark $(\bar{u}, \bar{c})$ respectively. The Feynman
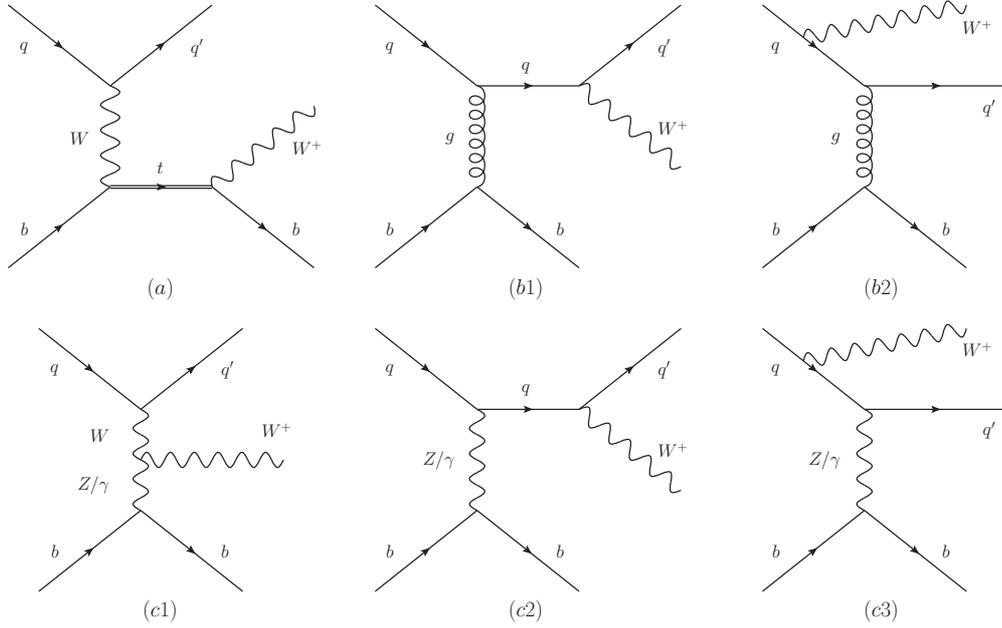
Figure 4.1: The tree-level Feynman diagrams contributing to the hard-scattering process in Eq. (4.3).

diagrams contributing to this process at tree level are shown in Figure 4.1. The decay of the W-boson is not shown. Of all the diagrams in the figure, only one actually contains a top quark, the rest of the diagrams constitute a background to our process of interest. We can divide the diagrams into two classes; *resonant* and *non-resonant*, or background, diagrams. Resonant diagrams (labelled (a) in the figure) contain an intermediate top-quark that we require to be close to its mass shell. The non-resonant diagrams do not contain such an intermediate top-quark and can be further classified into electroweak-mediated (EW) and QCD-mediated diagrams. The EW diagrams (labelled (c) in the figure) contain no colour connection (i.e. QCD particles) between the upper and lower quark lines. It should be noted that the resonant diagram is also an EW diagram. The QCD diagrams (labelled (b) in the figure) have a colour connection between the upper and lower quark lines in the form of a gluon.

The tree-level amplitude of the process shown in Eq. (4.3) is calculated by applying Feynman rules to the diagrams in Figure 4.1, with the W-decay included using the improved narrow-width approximation. This is explained, in detail, in Section 5.2. The amplitude can be written in the form

$$\mathcal{A}^{\text{tree}} = \frac{\mathcal{R}(p_i)}{p_t^2 - m_t^2} + \mathcal{N}(p_i) , \qquad (4.4)$$

where p_i are the external momenta, with $i = 1, 2, \ldots, 6$, and p_t is the momentum of the intermediate top-quark, $p_t = p_4 + p_5 + p_6$. The first term of the equation represents the resonant diagrams. The denominator of the intermediate top-quark propagator is shown explicitly, while the function $\mathcal{R}(p_i)$ contains the rest of the amplitude information. The second term, $\mathcal{N}(p_i)$, contains all the non-resonant amplitude information. It is clear to see that we encounter a pole when $p_t^2 = m_t^2$. This is due to a breakdown of strict, fixed-order perturbation theory as the intermediate top-quark approaches its mass shell. Corrections to the propagator which would usually be subleading become enhanced as the denominator, $p_t^2 - m_t^2$, becomes small. To counter this problem, we must resum these corrections. This is achieved by replacing the top-quark propagator,

$$\frac{i \left(\slashed{p}_t + m_t \right)}{p_t^2 - m_t^2} = \frac{i}{\slashed{p}_t - m_t} \rightarrow \frac{i}{\slashed{p}_t - m_t} \sum_{n=0}^{\infty} \left[\frac{\bar{\Sigma}_t(\slashed{p}_t)}{\slashed{p}_t - m_t} \right]^n = \frac{i}{\slashed{p}_t - m_t - \bar{\Sigma}_t(\slashed{p}_t)} , \qquad (4.5)$$

where $\bar{\Sigma}_t(\slashed{p}_t)$ is the sum of renormalised one-particle irreducible corrections to the top-quark two-point function. This is discussed further in Appendix A. This resummation shifts the pole of the top-quark propagator to a new location, μ_t, which is defined as the $\slashed{p}_t$ value at which the denominator of the propagator vanishes. That is, $\bar{\Gamma}_t(\mu_t) = 0$, where

$$\bar{\Gamma}_t(\slashed{p}_t) = \slashed{p}_t - m_t - \bar{\Sigma}_t(\slashed{p}_t) . \qquad (4.6)$$

This has a general solution of the form $\mu_t = m_t - i\Gamma_t/2$. There are some subtleties to this solution, however. Strictly speaking, the mass appearing in the propagator, Eq. (4.5), and that appearing in the definition of μ_t are not the same. The mass parameter which appears in the propagator is the renormalised mass, the exact definition of which is dependent on the renormalisation-scheme chosen. The mass parameter appearing in the definition of μ_t is the physical pole-mass. In general, the two definitions differ by an amount of $\mathcal{O}(\alpha_s)$. However, in the on-shell scheme, which we are using, the two masses are equivalent up to corrections of a higher order. This is discussed, in more detail, in Appendix A. Throughout the rest of this thesis, a single parameter, m_t, will be used. In the on-shell scheme, the parameter Γ_t is the on-shell top-quark decay-width. To include these resummation effects, we replace the denominator of the resonant propagator, $D_t = p_t^2 - m_t^2$, with $\Delta_t = p_t^2 - \mu_t^2$ in the amplitudes.

Expanding Eq. (4.4) around the complex pole of the full top-quark propagator, μ_t, we obtain

$$\mathcal{A}^{\text{tree}} = \frac{\mathcal{R}(p_i; p_t^2 = \mu_t^2)}{\Delta_t}(1 + \delta R_t) + \frac{\partial \mathcal{R}}{\partial p_t^2}(p_i; p_t^2 = \mu_t^2) + \mathcal{N}(p_i; p_t^2 = \mu_t^2) + \ldots, \quad (4.7)$$

where $(1 + \delta R_t)$ denotes the residue of the full top-quark propagator at $p_t^2 = \mu_t^2$.[†] The first term contains the leading contribution of the resonant diagram, while the second term is the first subleading contribution. In this term, the factor of Δ_t in the denominator has been cancelled by one which appears in the numerator due to the expansion. Terms containing higher orders of Δ_t are not shown explicitly but are present and represented by the ellipsis. The same expansion is performed on the non-resonant terms. The leading non-resonant contribution is shown, $\mathcal{N}(p_i; p_t^2 = \mu_t^2)$. Again, terms containing higher orders of Δ_t are present but not shown explicitly.

[†] $(1 + \delta R_t) = \left(\dfrac{\partial \bar{\Gamma}_t}{\partial \not{p}_t}(\mu_t) \right)^{-1} = 1 + \mathcal{O}(\alpha_{ew})$ in the on-shell scheme, see Appendix A.

This expansion can, in principle, be computed to any order in Δ_t. However, for our discussion, the terms shown in Eq. (4.7) are sufficient.

If we combine this expansion in Δ_t with the standard perturbative expansion in the electroweak and strong coupling constants, $\alpha_{ew} = g_{ew}^2/(4\pi)$ and $\alpha_s = g_s^2/(4\pi)$ respectively, we can systematically expand all amplitudes in terms of these parameters. For simplicity, we define one small expansion parameter, δ, which scales as

$$\delta \sim \alpha_{ew} \sim \alpha_s^2 \sim \frac{D_t}{m_t^2} \sim \frac{\Delta_t}{m_t^2}. \tag{4.8}$$

We can then expand all amplitudes in δ, and choose to what order in δ we wish to calculate.

Introducing the notation $A_{(l)}^{(m,n)}$ to represent an amplitude, stripped of its colour indices and coupling constants, that has a coupling prefactor $g_{ew}^m\, g_s^n$ multiplying it and which contains the propagator, Δ_t, to order l, i.e. $A_{(l)}^{(m,n)} \sim \Delta_t^l$, we can rewrite our tree-level amplitude, Eq. (4.7), as

$$\mathcal{A}^{\text{tree}} = \delta_{c_3 c_1}\delta_{c_4 c_2} \left(g_{ew}^3 A_{(-1)}^{(3,0)} + g_{ew}^3 A_{(0)}^{(3,0)} \right) + t_{c_3 c_1}^A \left(t_A \right)_{c_4 c_2} g_{ew} g_s^2 A_{(0)}^{(1,2)} + \dots\,, \tag{4.9}$$

where c_i is the colour index of the external quark, i. Note that the coupling from the decay of the W-boson is not counted in the above equation. As the W-decay would appear in all diagrams, we do not need to include its coupling in our expansion. Our treatment of the W-boson decay will be discussed in Section 5.2. Comparing Eqs. (4.7) and (4.9), the $g_{ew}^3 A_{(-1)}^{(3,0)}$ term corresponds to $\mathcal{R}(p_i; p_t^2 = \mu_t^2)/\Delta_t$, i.e. the leading part of the resonant diagrams. Similarly, $g_{ew}^3 A_{(0)}^{(3,0)}$ corresponds to the leading part of the non-resonant term, $\mathcal{N}$, arising from the EW-mediated diagrams. The final term of Eq. (4.9) corresponds to the leading part of the $\mathcal{N}$ term arising from

the QCD-mediated diagrams. The ellipsis represents the subleading terms and the term $\mathcal{R}(p_i; p_t^2 = \mu_t^2) \, \delta R_t / \Delta_t$, which is suppressed with respect to the leading part of the resonant diagram as $\delta R_t \sim \alpha_{ew} \sim \delta$ in the on-shell renormalisation scheme (see Appendix A).

Using the definition of our expansion parameter, δ, given in Eq. (4.8), we can see that the terms in Eq. (4.9) scale as follows; $g_{ew}^3 A_{(-1)}^{(3,0)} \sim \delta^{1/2}$, $g_{ew}^3 A_{(0)}^{(3,0)} \sim \delta^{3/2}$ and $g_{ew} g_s^2 A_{(0)}^{(1,2)} \sim \delta$. The colour-averaged, squared matrix-element at tree level is given by

$$
\begin{aligned}
\mathcal{M}^{\text{tree}} &= \frac{1}{N_c^2} \sum_c \left| \mathcal{A}^{\text{tree}} \right|^2 \\
&= g_{ew}^6 \left| A_{(-1)}^{(3,0)} \right|^2 + g_{ew}^6 \, 2 \operatorname{Re} \left[A_{(0)}^{(3,0)} \left(A_{(-1)}^{(3,0)} \right)^* \right] + g_{ew}^2 g_s^4 \frac{C_F}{2N_c} \left| A_{(0)}^{(1,2)} \right|^2 + \dots,
\end{aligned}
\tag{4.10}
$$

where N_c is the number of colours and $C_F = (N_c^2 - 1)/(2N_c)$. The first term scales as $\sim \delta$, while the other two terms scale as $\sim \delta^2$. The ellipsis denotes terms of higher order in δ. Note that, in principle, the interference terms between the resonant diagram and the QCD-mediated diagrams scale as $g_{ew}^4 g_s^2 \, 2 \operatorname{Re} \left[A_{(0)}^{(1,2)} \left(A_{(-1)}^{(3,0)} \right)^* \right] \sim \delta^{3/2}$. They vanish due to the colour structure, however. We define our LO contributions to be those which scale as $\sim \delta$ in the squared matrix-element. That is, our LO corresponds to the leading part of the resonant diagram, squared. Our NLO is then defined as the contributions which are suppressed by a factor of $\alpha_s \sim \delta^{1/2}$ with respect to the LO contributions. This consists of all contributions to the squared matrix-element which scale as $\sim \delta^{3/2}$.

By introducing the expansion in our small parameter, δ, we have reduced the amount of computation required in calculating the cross section up to a certain order in δ. At LO, for example, the full calculation requires calculating the matrix elements of all diagrams shown in Figure 4.1. However, after our expansion, we need only calculate the leading part of the matrix element of the resonant diagrams. Choosing only certain diagrams from a set can lead to problems with gauge dependence,
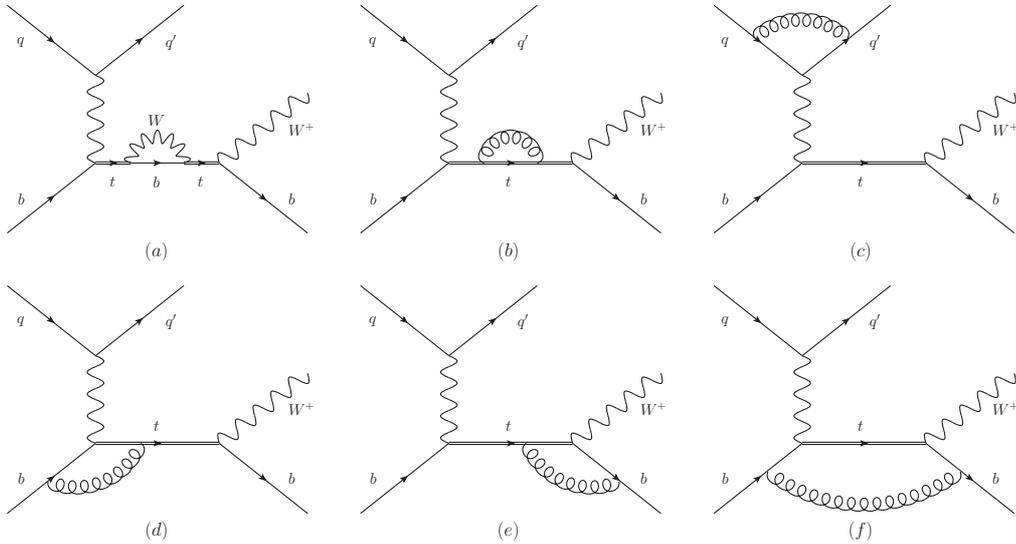
Figure 4.2: The one-loop Feynman diagrams required to calculate the NLO cross section of the hard-scattering process in Eq. (4.3) to $\mathcal{O}(\delta^{3/2})$.

however. Of the diagrams shown in Figure 4.1, the full set of QCD-mediated diagrams (b) form a gauge-invariant set and, similarly, the full set of EW-mediated diagrams form a separate gauge-invariant set. The full set of EW diagrams must include the resonant diagram, however. That is, diagrams (a) and (c) together are gauge invariant. Therefore, by calculating only diagram (a), we naturally break gauge invariance. This is not a problem, however, as our leading-order amplitude, $A_{(-1)}^{(3,0)}$, is formally gauge independent up to terms suppressed by a factor of δ or higher. That is, the gauge-violating terms, which in the full calculation would be cancelled by the rest of the EW-mediated diagrams, scale as $\sim \delta^2$ and are thus beyond the target accuracy of our calculation. As long as δ remains small we can ignore their effects. If δ were to become too large (~ 1), our expansion would break down and the full gauge-invariant set would need to be calculated.

To complete our calculation to NLO, we must include all contributions suppressed by a factor $\sim \delta^{1/2}$ with respect to the leading part of the resonant diagram in the squared matrix-element. That is, amplitudes of the form $A_{(-1)}^{(3,2)}$ which interfere with

$A_{(-1)}^{(3,0)}$, or those of the form $A_{(-1)}^{(3,1)}$ which do not interfere with $A_{(-1)}^{(3,0)}$, but are instead squared. The first set of amplitudes, $A_{(-1)}^{(3,2)}$, correspond to the virtual corrections to diagram (a) of Figure 4.1 which contain one QCD loop. These are shown in Figure 4.2. The second set of amplitudes, $A_{(-1)}^{(3,1)}$, correspond to the real QCD corrections to diagram (a) of Figure 4.1. These are shown in Figures 4.3 and 4.4. This gives us two more contributions to our cross section;

$$\mathcal{M}^{\text{Virtual}} = g_{ew}^6 g_s^2 \, 2 \operatorname{Re} \left[A_{(-1)}^{(3,2)} \left(A_{(-1)}^{(3,0)} \right)^* \right] \tag{4.11}$$

and

$$\mathcal{M}^{\text{Real}} = g_{ew}^6 g_s^2 \left| A_{(-1)}^{(3,1)} \right|^2 = \left| \mathcal{A}_{qb}^{\text{Real}} \right|^2 + \left| \mathcal{A}_{gb}^{\text{Real}} \right|^2 + \left| \mathcal{A}_{qg}^{\text{Real}} \right|^2 , \tag{4.12}$$

where $\mathcal{A}_{qb}^{\text{Real}}$ are the amplitudes containing the resonant diagram dressed with an extra outgoing gluon, shown in Figure 4.3, and $\mathcal{A}_{gb}^{\text{Real}}$ and $\mathcal{A}_{qg}^{\text{Real}}$ are the amplitudes with a gluon as an initial-state parton and an extra (anti-)quark in the final state, shown in Figure 4.4.

There are some subtleties with both of these contributions, however. For the virtual contributions, diagram (a) of Figure 4.2 contains an electroweak loop rather than a QCD loop. The reasons behind its inclusion will be discussed in the next section, and in Section 5.4. For the real contributions, the diagrams with an initial-state gluon on the lower quark line, diagrams (b)-(d) of Figure 4.4, clearly contain a final-state $\bar{b}$-jet which violates our veto. We will keep these contributions, however, as they are required when comparing our results to those which exist in the literature. The strict application of a veto on a final-state $\bar{b}$-jet will be discussed in Chapter 6.
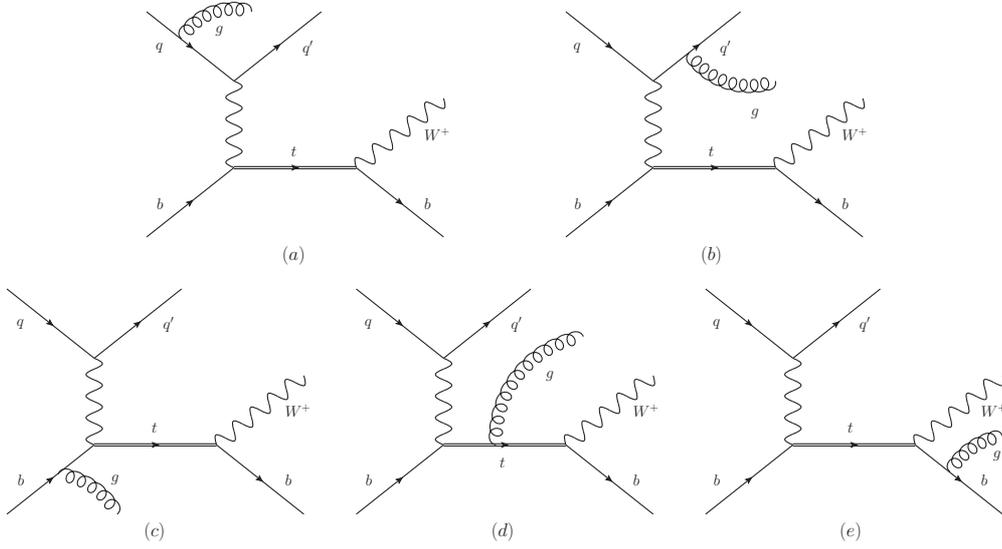
Figure 4.3: The Feynman diagrams containing an extra emitted gluon required to calculate the real contribution to the NLO cross section of the hard-scattering process in Eq. (4.3) to $\mathcal{O}(\delta^{3/2})$.
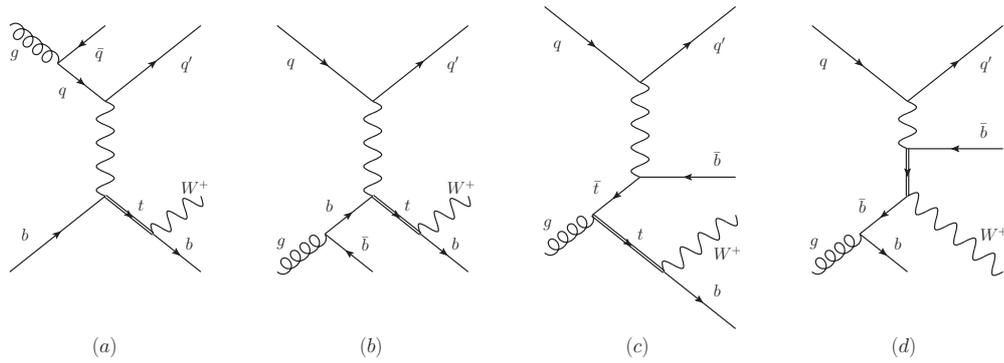
Figure 4.4: The gluon-initiated Feynman diagrams required to calculate the real contribution to the NLO cross section of the hard-scattering process in Eq. (4.3) to $\mathcal{O}(\delta^{3/2})$.

We now have all the Feynman diagrams necessary to complete our calculation to $\mathcal{O}(\delta^{3/2})$. The next step is to compute all required matrix elements from these Feynman diagrams. This will be the focus of the rest of this chapter.

4.3 Loop Corrections

As in the tree-level case, to calculate the loop amplitudes we must expand the Feynman diagrams systematically in δ. This expansion consists of a Taylor expansion of the amplitude, analogous to that of the tree-level case, along with an asymptotic expansion of the loop integrals. The expansion of the integrals is performed using the *method of regions* [20, 21]. This involves splitting the loop momentum into various kinematic regions. In each of these regions, the integrand can be expanded in any momenta and invariants which are small in that region. The resulting integrands are then integrated over all possible loop momenta and the contributions of each kinematic region summed.

The first step in obtaining the amplitudes is to ascertain which Feynman diagrams contribute at the required order. We want to complete our calculation to $\mathcal{O}(\delta^{3/2})$ and, therefore, require all loop diagrams with amplitudes which scale as $\sim \delta$. The simplest category of diagrams fitting this constraint are those comprising the resonant LO diagrams with a QCD loop. These are shown in diagrams (b)-(f) of Figure 4.2. It should be noted that while, in principle, the diagrams with a gluon joining the upper and lower quark lines also contribute at this order, their colour structure is such that, when combined with the LO matrix-element, their contribution is zero. As they do not contribute to our overall result, their amplitudes need not be calculated and they are not shown in the figure. Diagram (a) of Figure 4.2 does not, at first glance, appear to have the required scaling. Instead, it appears to be suppressed by an extra factor
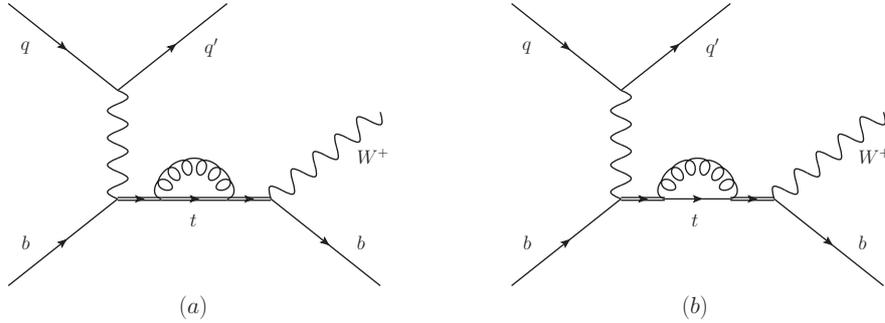
Figure 4.5: Feynman diagrams representing the soft (a) and hard (b) contributions to the one-loop QCD top-quark self-energy diagram.

of $\delta^{1/2}$, due to having electroweak loop, rather than QCD loop, and contribute beyond our target accuracy. However, as we will see later in the section, when considered with certain loop momenta, its contribution is enhanced and it must be included in our calculation.

Now we have all the required Feynman diagrams, we must consider the relevant loop-momentum regions. For our process there are only two relevant momentum regions; the *soft* region and the *hard* region. The soft-momentum region is defined as the region in which the loop momentum, k, scales as $k \sim \Gamma_t \sim m_t \delta$, whereas in the hard-momentum region, $k \sim m_t$. For simplicity, we will drop factors of m_t in the scaling relations and redefine the soft region as $k \sim \delta$ and the hard region as $k \sim 1$. Each diagram is split into soft and hard components and their respective contributions summed. We can identify the hard components with the factorisable corrections, while the soft components correspond to the non-factorisable corrections [70]. A more detailed discussion of this method, along with an example calculation for one of the diagrams, is given in Section 5.3. The remainder of this section will focus on the contributions of diagrams (a) and (b) of Figure 4.2, which do not always scale as expected.

If we consider the one-loop QCD contribution to the top-quark self-energy, diagram (b) of Figure 4.2, we expect this to scale as $\sim \delta$. The scaling, however, depends on

the loop-momentum region. Representations of the soft and hard contributions to the diagram are shown in Figure 4.5. If we consider a stripped down amplitude containing only the couplings, the integration measure, d^4k, and the denominators of the top-quark propagators,

$$\mathcal{A} \sim g_{ew}^3 g_s^2 \frac{d^4k}{\Delta_t^2 \, k^2 \left((p_t - k)^2 - m_t^2\right)} = g_{ew}^3 g_s^2 \frac{d^4k}{\Delta_t^2 \, k^2 \left(k^2 - 2p_t \cdot k + D_t\right)}, \qquad (4.13)$$

we can examine its behaviour in the two relevant loop-momentum regions. In the soft-momentum region, $k \sim \delta$, the denominator of the propagator originating from the top-quark in the loop becomes $(-2p_t \cdot k + \Delta_t)$. Here we have dropped the factor k^2, as it is suppressed with respect to $p_t \cdot k$ and Δ_t, and we have replaced $D_t \to \Delta_t$ as the denominator scales as $\sim \delta$ and so finite-width effects must be included. Using this, along with the fact that $g_{ew}^3 g_s^2 \sim \delta^2$ and $d^4k \sim \delta^4$, in the soft region, we obtain the scaling

$$\mathcal{A}^S \sim g_{ew}^3 g_s^2 \frac{d^4k}{\Delta_t^2 \, k^2 \left(-2p_t \cdot k + \Delta_t\right)} \sim \delta^2 \frac{\delta^4}{\delta^2 \cdot \delta^2 \cdot \delta} \sim \delta \qquad (4.14)$$

for the soft contribution. This agrees with the expected scaling. We can see that the denominator effectively contains three resonant top-quark propagators, as shown in diagram (a) of Figure 4.5. The extra factors of δ appearing in the denominator due to the extra resonant propagators combine with those from the soft-gluon propagator, $1/k^2 \sim 1/\delta^2$, to cancel out by those which appear in the numerator from the integration measure, however, leading to the agreement with the expected scaling. In the hard momentum region, $k \sim 1$, the denominator of the propagator coming from the top-quark in the loop becomes $(k^2 - 2p_t \cdot k)$, where we have dropped the D_t as it scales $\sim \delta$ and is suppressed with respect to k^2 and $2p_t \cdot k$. Hence, for the hard contribution

we obtain the scaling

$$\mathcal{A}^H \sim g_{ew}^3 g_s^2 \frac{d^4k}{\Delta_t^2 \, k^2 \, (k^2 - 2p_t \cdot k)} \sim \delta^2 \frac{1^4}{\delta^2 \cdot 1^2 \cdot 1} \sim 1 \, . \qquad (4.15)$$

This appears to be a problem. This contribution is not only less suppressed than expected, it is actually enhanced with respect to our LO contribution, which scales as $\sim \delta^{1/2}$. We will therefore refer to this contribution as a '*superleading*' contribution. As will be shown in Section 5.4, however, this 'superleading' contribution will be cancelled out exactly by the top-quark self-energy counterterm in the on-shell renormalisation scheme. In a general renormalisation scheme, these terms would be resummed inside the complex pole of the top-quark propagator. The enhancement of the diagram in the hard loop-momentum region can be seen more clearly in diagram (b) of Figure 4.5. The presence of a hard gluon loop on the intermediate top-quark line leads to two resonant propagators in the amplitude. It is this extra propagator, $1/\Delta_t \sim 1/\delta$, which causes the enhancement over the expected scaling of the diagram. It should be noted that, along with the 'superleading' terms, the hard diagram also contains contributions that scale as expected, $\sim \delta$, and must be included in our amplitude. In this particular case, these subleading terms are also cancelled by the counterterm, as will be shown in Section 5.4. This is not general, however.

As we have seen, diagrams containing a loop on the intermediate top-quark line may become enhanced in certain loop-momentum regions. Therefore, to ensure we include all relevant contributions, we must consider diagrams which would naïvely scale as $\sim \delta^{3/2}$ but may be enhanced. Examples of this class of diagram are the electroweak contributions to the one-loop top-quark self-energy. The amplitudes of these diagrams have the same form as those of the QCD contribution but with the strong coupling, g_s, replaced by the electroweak coupling, g_{ew}. Making this replacement in Eqs. (4.14)

and (4.15), we see that the soft contribution scales as $\sim \delta^{3/2}$, which is the expected scaling of the diagram, and can be neglected as it is beyond our target accuracy. The hard contribution, however, scales as $\sim \delta^{1/2}$, the same scaling as our LO diagram. This leading contribution, therefore, must be included. This is achieved through the resummation of the top-quark propagator. As will be discussed in Section 5.4 and Appendix A, it is only the imaginary part of these diagrams which is resummed. Only one of the contributing diagrams contains an imaginary part and, hence, it is the hard part of this diagram that is shown as diagram (a) of Figure 4.2. Similarly, the two-loop QCD contribution to the top-quark self-energy has a soft scaling $\sim \delta^{3/2}$ which can be neglected, but a hard scaling $\sim \delta^{1/2}$ which we must include. This is again achieved via resummation. In the on-shell scheme we are using, we get a cancellation of its leading contribution with the counterterm diagram, as in the one-loop case (see Appendix A). Its subleading contributions are beyond our target accuracy and can be neglected.

4.4 Real Corrections

The final set of diagrams required for the calculation are the real correction diagrams. The contributing Feynman diagrams, at the order we are interested in, are shown in Figures 4.3 and 4.4. These correspond to the resonant tree-level diagram with an extra emitted gluon and the gluon-initiated processes containing a resonant top-quark respectively. There are similar diagrams based on the other tree-level diagrams, or with an extra photon, rather than gluon, in the final state. These contribute beyond our target accuracy, however.

Calculating the amplitudes of these diagrams is not as straightforward as in the tree-level and one-loop cases. For consistency, the real amplitudes should be calculated in

the same way as the virtual amplitudes, using the method of regions. This is necessary to preserve the cancellation of infrared poles, as outlined in Section 3.2. In general, the infrared poles of the real contributions are isolated via the subtraction and re-addition of a local counterterm, $d\sigma^A$, as discussed in Section 3.3. Using this subtraction method, the real cross section is given by

$$\hat{\sigma}^{\text{Real}} = \int \left(d\sigma^R - d\sigma^A \right) + \int d\sigma^A \, . \tag{4.16}$$

The local counterterm approximates the full real matrix element in all singular regions, making the first term of Eq. (4.16) finite. The partial integration of the local counterterm over the phase-space of the single emitted particle leads to analytic ϵ-poles in the second term that exactly cancel those coming from the virtual diagrams. This full cancellation occurs only if the real and virtual contributions are calculated consistently. The application of the effective theory to the real calculations raises some issues, however.

Firstly, the presence of an extra final-state particle, with momentum p_7, leads to an uncertainty on the exact definition of the expansion parameter. This can be seen by considering the diagrams in Figure 4.3. These have a resonant top-quark propagator when $p_t^2 \simeq m_t^2$. For diagrams (a)-(c), it is clear to see that $p_t = p_W + p_b$, as in the tree-level and one-loop cases. However, for diagram (e), the top-quark momentum, $p_t = p_W + p_b + p_7$. Diagram (d) is resonant for both kinematic configurations. Both of these kinematic regions are relevant and must be taken into account. Another problem relates to the definition of our observables. We want to be able to calculate any infrared-safe observable and thus we need to perform the calculation of the amplitudes without having any variable explicitly defined. However, the definition of an observable may introduce additional scales which we would need to consider in our effective

theory. Hence, we must deviate from the effective theory used to calculate the virtual corrections, but ensure that the exact cancellation of the infrared poles remains.

In our calculation we use the full matrix-element to calculate the real corrections. This ensures that all required contributions are included and that the observable definition cannot affect our expansion in δ. Using the full matrix-element will spoil the cancellation of the virtual poles, however. To combat this, we must modify the form of the local counterterm that is added back to the amplitude. The local counterterm, $d\sigma^A$, becomes important in kinematic regions where a gluon is soft or two partons become collinear and, therefore, it is always clear what the correct form of the expansion parameter should be. Hence, we introduce an expanded local counterterm, $d\sigma^A_{\text{exp}}$, and modify Eq. (4.16) to

$$\hat{\sigma}^{\text{Real}} = \int \left(d\sigma^R - d\sigma^A \right) + \int d\sigma^A_{\text{exp}} + \mathcal{O}(\delta^2) \,. \tag{4.17}$$

The error introduced by changing $d\sigma^A$ to $d\sigma^A_{\text{exp}}$ is of order δ^2 and is thus beyond our target accuracy. We now have a consistent way in which to treat our real amplitudes, ensuring the required cancellation of infrared poles between the full real matrix-element and the local counterterm and between the explicit virtual poles and those of the partially-integrated, expanded local counterterm.

4.5 Completing the Calculation

Once we have all the amplitudes required for our calculation, the next step is to select a suitable jet-defining function. Any jet definition can be used provided it is both infrared and collinear safe. Exact details of the jet-defining function used in our calculations are given in Appendix B.

With all the required amplitudes and a jet-defining function, the final step is to perform the necessary integrals in order to obtain the cross section of the process. These integrals are calculated using *Monte Carlo integration*. For our calculations, we use the 'Vegas' adaptive Monte Carlo algorithm from the 'CUBA' library for multidimensional numerical integration [71].

The results presented in Chapters 5 and 6 were calculated using two independent programs, one implemented using the Catani-Seymour dipole subtraction method, as outlined in Section 3.3, and the other using FKS subtraction. The agreement of the results of these two programs provided a useful check of the two implementations.

Chapter 5

An Example Calculation: t-Channel Single-Top Production

In this chapter, the methods outlined in Chapter 4 are applied to t-channel single-top production leading to the full set of amplitudes required to calculate the cross section of the process to NLO in our counting. The final section contains some basic results, a comparison to existing results and a discussion of the validity of our δ-counting.

The following abbreviations are used throughout this chapter and the rest of the thesis:

$$s_{ij} = (p_i + p_j)^2 \,, \qquad D_t = p_t^2 - m_t^2 \,,$$
$$p_t = p_4 + p_5 + p_6 \,, \qquad \Delta_t = p_t^2 - \mu_t^2 \,. \tag{5.1}$$

The helicity notation, described in Section 3.5, is used for the amplitudes.
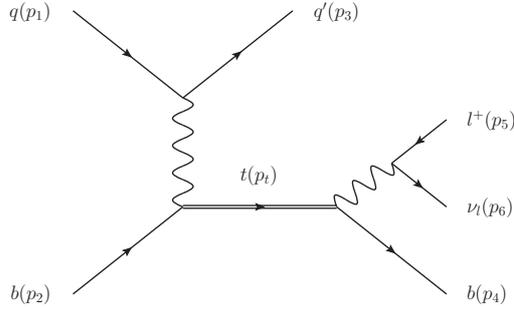
Figure 5.1: The only tree-level Feynman diagram contributing to the LO cross section of the hard-scattering process in Eq. (4.3) to $\mathcal{O}(\delta)$.

5.1 Tree-Level Amplitude

As was shown in Chapter 4, the only diagram relevant to our calculation at tree level is the resonant one, shown in Figure 5.1, which scales as $\sim \delta^{1/2}$. Calculating the amplitude using the helicity method, the only non-vanishing contribution is that of the helicity configuration $q_L\, b_L \to q'_L\, b_L\, l^+_R\, \nu_L$, where q is a light quark. The amplitude of the diagram, with the decay of the W-boson included using the improved narrow-width approximation (iNWA), is

$$A^{(3,0)}_{(-1)} = g_{ew}\sqrt{\frac{1}{2M_W\Gamma_W}}\frac{[12]\langle 46\rangle\langle 3|4+6|5]}{(s_{13}+M_W^2)\,\Delta_t}\,. \tag{5.2}$$

This equation contains a factor g_{ew}, whereas the amplitudes, $A^{(m,n)}_{(l)}$, are supposed to have been stripped of their coupling constants. This extra coupling constant comes from the inclusion of the W-boson decay. As the amplitude also contains a factor $\Gamma_W^{-1/2}$ and $\Gamma_W \sim g_{ew}^2$, this dependence on g_{ew} cancels out and our overall counting is not affected, however. It should be noted that the above amplitude is correct only if the initial-state q is a quark. If q represents an anti-quark, the relevant amplitude is obtained by crossing the momenta $p_1 \leftrightarrow -p_3$ in Eq. (5.2). This momentum crossing can also be applied to the one-loop and real amplitudes.

5.2 Inclusion of the W-Boson Decay

As mentioned in the previous section, we treat the decay of the W-boson using the iNWA. This has been discussed briefly in the context of a heavy-particle treatment in Section 3.4. A more thorough description of both the NWA and iNWA, as they apply to the W-boson decay in this calculation, will be given here. In the NWA, we treat the production of the W-boson and its decay separately, joining the two processes with a propagator. If we refer to the production amplitude, stripped of the polarisation vector due to the external W-boson, $\varepsilon(p_W)$, as $\mathcal{A}^{\mathrm{prod}}$ and the squared matrix-element for the decay of the W-boson as $\mathcal{M}^{\mathrm{decay}}$, then the total cross section is

$$
\begin{aligned}
\sigma(\mathrm{NWA}) = \int d\Phi^{\mathrm{prod}}(p_i; p_W)(\mathcal{A}_\mu^{\mathrm{prod}})^* \mathcal{A}_\nu^{\mathrm{prod}} \sum_k \varepsilon_k^\mu(p_W)(\varepsilon_k^\nu)^*(p_W) \\
\cdot \int \frac{d\tilde{p}_W^2}{(2\pi)((\tilde{p}_W^2 - M_W^2)^2 + M_W^2\Gamma_W^2)} \int d\Phi^{\mathrm{decay}}(p_W; p_j)\mathcal{M}^{\mathrm{decay}} ,
\end{aligned}
\tag{5.3}
$$

where $i = 1, 2, 3, 4$ are the particles involved in the production process, $j = 5, 6$ are the particles coming from the W-boson decay, and k are polarisation states. As mentioned in Section 3.4, we require that the W-boson is on-shell in the production and decay subprocesses, $p_W^2 = M_W^2$, whereas in the propagator we relax this constraint and integrate over all possible momenta, $\tilde{p}_W$, as in Eq. (3.24). Contracting the Lorentz indices in the production stage, to give us a separate production squared matrix-element, $\mathcal{M}^{\mathrm{prod}}$, we obtain

$$
\sigma(\mathrm{NWA}) = \frac{1}{2\Gamma_W M_W} \int d\Phi^{\mathrm{prod}}(p_i; p_W)\mathcal{M}^{\mathrm{prod}} \int d\Phi^{\mathrm{decay}}(p_W; p_j)\mathcal{M}^{\mathrm{decay}} .
\tag{5.4}
$$

It can clearly be seen that the production and decay subprocesses are separate, with the only parameter linking the two processes being the on-shell W-boson momentum. If we move to the iNWA, however, rather than writing the external W-boson of the

production process in terms of its polarisation vectors, we instead define a leptonic tensor, $L^{\mu\nu}$, which encompasses its decay and contract this with the stripped production amplitudes. The total cross section is then

$$\sigma(\text{iNWA}) = \int d\Phi^{\text{prod}}(p_i; p_W)(\mathcal{A}_\mu^{\text{prod}})^* \mathcal{A}_\nu^{\text{prod}}$$
$$\cdot \int \frac{d\tilde{p}_W^2}{(2\pi)((\tilde{p}_W^2 - M_W^2)^2 + M_W^2 \Gamma_W^2)} \int d\Phi^{\text{decay}}(p_W; p_j) L^{\mu\nu} \,. \tag{5.5}$$

We must now contract the Lorentz indices across the production and decay processes. This leads to a mixing of the production and decay momenta, i and j, and preserves the correlations between them. We call the amplitude and squared matrix-element, after this contraction, $\mathcal{A}$ and $\mathcal{M}$ respectively and obtain

$$\sigma(\text{iNWA}) = \frac{1}{2\Gamma_W M_W} \int d\Phi^{\text{prod}}(p_i; p_W) \int d\Phi^{\text{decay}}(p_W; p_j) \mathcal{M}(p_i, p_j) \,, \tag{5.6}$$

where, as usual, $\mathcal{M} = |\mathcal{A}|^2$. For simplicity, we absorb the overall prefactor of $1/(2\Gamma_W M_W)$ into our amplitudes, leaving each with a factor $\sqrt{1/(2\Gamma_W M_W)}$. It is this factor, along with the coupling constant, g_{ew}, which comes from the leptonic tensor, that appears in Eq. (5.2) and will also appear in the rest of the amplitudes.

5.3 One-Loop Amplitudes

As explained in Chapter 4, the only one-loop diagrams required to calculate the cross section to NLO in our counting are shown in Figure 4.2. To calculate these amplitudes, we use the method of regions to simplify the expressions, splitting each into a soft and hard component. This was explained in Section 4.3. The soft-momentum region is defined as the region in which the loop-momentum scales as $k \sim \delta$, whereas in the hard-
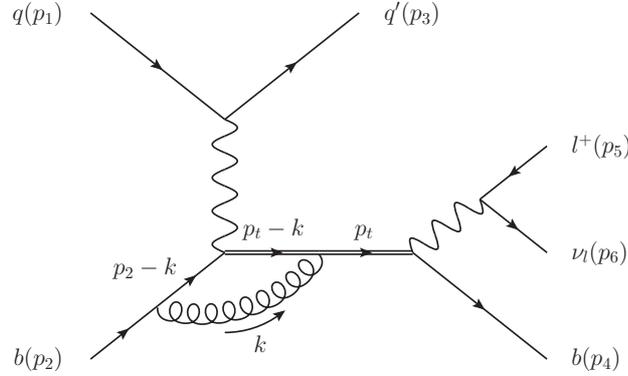
Figure 5.2: An example one-loop Feynman diagram required for the NLO calculation. Labels on internal lines represent momenta.

momentum region $k \sim 1$. In this section, we will show, explicitly, the application of this method to one of the required diagrams, to illustrate its use, and briefly discuss the simplifications it allows us to make to the other diagrams. The hard parts of diagrams (a) and (b) of Figure 4.2 constitute special cases and will be discussed separately at the end of this section.

We take diagram (d) of Figure 4.2 as our example diagram. For clarity, this is shown in more detail in Figure 5.2. After applying Feynman rules, we obtain an expression for the amplitude that has the form

$$A_{(-1),d}^{(3,2)} \sim \int \frac{d^d k}{(2\pi)^d} \frac{\dots (\not{p}_t + m_t)\gamma^\mu(\not{p}_t - \not{k} + m_t)\dots(\not{p}_2 - \not{k})\gamma_\mu u(p_2)}{\dots D_t\, k^2\left((p_t - k)^2 - m_t^2\right)(p_2 - k)^2}, \qquad (5.7)$$

where overall constants have been omitted, for simplicity, and the ellipses represent quantities which are not dependent on the loop momentum. The parameter, d, represents the number of space-time dimensions and will be set to $4 - 2\epsilon$.

We first consider the soft-momentum region, $k \sim \delta$, and look at the expansion of the denominators of the various propagators. The denominator of the gluon propagator has only one scale, $k^2 \sim \delta^2$, and hence, it is not expanded. The denominator of the

bottom-quark propagator becomes

$$(p_2 - k)^2 = p_2^2 - 2p_2 \cdot k + k^2 \rightarrow -2p_2 \cdot k \,, \tag{5.8}$$

where we have used the fact that $p_2^2 = m_b^2 = 0$ and we have neglected the k^2 term, which scales as $\sim \delta^2$, as it is suppressed in comparison to the $p_2 \cdot k$ term, which scales as $\sim \delta$. Similarly, the denominator of the top-quark propagator can be written as

$$(p_t - k)^2 - m_t^2 = k^2 - 2p_t \cdot k + D_t \rightarrow \Delta_t - 2p_t \cdot k \,, \tag{5.9}$$

where we again neglect the k^2 term, as it is suppressed compared to $p_t \cdot k$ and D_t which both scale as $\sim \delta$, and we make the replacement $D_t \rightarrow \Delta_t$, as $D_t - 2p_t \cdot k \sim \delta$ and so finite-width effects must be resummed to all orders. Applying the same methodology to the numerator of Eq. (5.7), the loop momentum is always parametrically smaller than the external momenta, p_i, and so can be neglected. Hence, the numerator becomes

$$\ldots (\slashed{p}_t + m_t)\gamma^\mu (\slashed{p}_t - \slashed{k} + m_t)\ldots (\slashed{p}_2 - \slashed{k})\gamma_\mu u(p_2) \rightarrow$$

$$\ldots (\slashed{p}_t + m_t)\gamma^\mu (\slashed{p}_t + m_t)\ldots (\slashed{p}_2)\gamma_\mu u(p_2) = 4p_2 \cdot p_t \ldots (\slashed{p}_t + m_t)\ldots u(p_2) \,, \tag{5.10}$$

where we have used Dirac algebra and the properties of the u-spinor,

$$\slashed{p}_2 \gamma_\mu u(p_2) = 2(p_2)_\mu u(p_2) \tag{5.11}$$

$$(\slashed{p}_t + m_t)\gamma^\mu (\slashed{p}_t + m_t) = 2p_t^\mu (\slashed{p}_t + m_t) - D_t \gamma^\mu \,. \tag{5.12}$$

We also drop the D_t term in Eq. (5.12), as it is suppressed by a factor $\sim \delta$, to further simplify the expanded numerator. Putting these simplifications together, the leading

contribution to the amplitude is given by

$$A_{(-1),d}^{(3,2),S} \sim \frac{\dots(\not{p}_t + m_t)\dots u(p_2)}{\dots\Delta_t}\,(4p_2 \cdot p_t) \int \frac{d^dk}{(2\pi)^d} \frac{1}{k^2(\Delta_t - 2p_t \cdot k)(-2p_2 \cdot k)} \quad (5.13)$$

in the soft-momentum region. The factors which do not contain a dependence on k have been moved outside the integral. Here, we recover an expression that is proportional to the tree-level amplitude, given in Eq. (5.2). This factorisation into the tree-level amplitude multiplied by an overall loop integral is general for all the soft amplitudes. That is,

$$A_{(-1),i}^{(3,2),S} = \delta V_i^S A_{(-1)}^{(3,0)}, \quad (5.14)$$

where δV_i^S is the soft factor for diagram (i) of Figure 4.2 and $A_{(-1)}^{(3,0)}$ is the tree-level amplitude. This factorisation is due to the simple structure of the quark-gluon vertex in the soft limit (the eikonal approximation),

$$\frac{(\not{p} - \not{k})\gamma^\mu}{(p - k)^2} \to \frac{p^\mu}{(-p \cdot k)}\,. \quad (5.15)$$

For our example diagram, the soft factor is given by

$$\delta V_d^S = -4iC_F \tilde{\mu}^{2\epsilon}(p_2 \cdot p_t) \int \frac{d^dk}{(2\pi)^d} \frac{1}{k^2} \frac{1}{(\Delta_t - 2p_t \cdot k)} \frac{1}{(-2p_2 \cdot k)}\,, \quad (5.16)$$

where $\tilde{\mu}^{2\epsilon} = e^{\epsilon\gamma_E}\mu^{2\epsilon}/(4\pi)^\epsilon$ and $\mu = \mu_R$ is the renormalisation scale. The introduction of the parameter $\tilde{\mu}$ leads to a simplification of the $\overline{\text{MS}}$ scheme, introduced in Section 3.2. When combined with the $\bar{\epsilon}$-poles (defined in Eq. (3.10)), which arise from the UV divergences of the loop integrals, we get a cancellation of the exponential and (4π) terms leaving only a factor $\mu^{2\epsilon}$ and ϵ-poles. The $\overline{\text{MS}}$ subtraction scheme then involves the removal of the ϵ-poles only.

At this stage, it is useful to check that our diagram still has the same δ-scaling as expected. It is possible that, for some diagrams, the soft and/or hard contributions may be suppressed by extra factors of δ and thus beyond the required accuracy of our calculation. These can then be neglected. For our NLO calculation, we require diagrams suppressed by a factor $\sim \delta^{1/2}$ with respect to the tree-level amplitude. Due to the prefactors, $A^{(3,2)}_{(-1)}$ is already suppressed by a factor $g_s^2 \sim \delta^{1/2}$ with respect to $A^{(3,0)}_{(-1)}$ and, therefore, we require $\delta V^S \sim 1$ for the contribution to be included in our calculation. Considering the denominators of the propagators in δV_d^S, Eq. (5.16); the gluon propagator has scaling, $k^2 \sim \delta^2$, the bottom-quark propagator, $(-2p_2 \cdot k) \sim \delta$, and the top-quark propagator, $(\Delta_t - 2p_t \cdot k) \sim \delta$, giving a total contribution that scales as $\sim \delta^4$. The numerator contains the infinitesimal volume element, $d^d k$, which scales as $\sim \delta^d$. However, we know that $d = 4 - 2\epsilon$ with $\epsilon \to 0$ and thus, $d^d k \sim \delta^4$. This exactly cancels the contribution of the denominator leaving $\delta V_d^S \sim 1$, as required for the diagram to be included in our calculation. We can perform the integral in Eq. (5.16) using standard techniques. This leads to the simple result

$$\delta V_d^S = \frac{C_F}{8\pi^2} \left[\frac{1}{2\epsilon^2} + \frac{5}{24}\pi^2 \right] \left(-\frac{\Delta_t}{\mu m_t} \right)^{-2\epsilon}. \tag{5.17}$$

Here we can see how the $\tilde{\mu}^{2\epsilon}$ factor has combined with the $\bar{\epsilon}$-poles from the loop integral leaving only ϵ-poles.

Applying the above method to the other one-loop diagrams of Figure 4.2, we obtain a full set of soft amplitudes. These are given in Eqs. (C.7)-(C.11) of Appendix C. Diagram (a) of Figure 4.2 has an amplitude of the form $A^{(5,0)}_{(-1),a}$ and thus, as mentioned in Section 4.3, should naïvely contribute at an accuracy beyond that at which we are aiming. In the case of the soft contributions this is true. We find that $g_{ew}^5 A^{(5,0),S}_{(-1),a} \sim \delta^{3/2}$, a suppression of a factor $\sim \delta$ with respect to our LO contribution, which is beyond our

target accuracy. Hence, there is no soft contribution from diagram (a). Another point of note is that the soft contribution of diagram (c) of Figure 4.2 is zero, as we are left with a scaleless integral. This occurs as the gluon is attached to the upper quark line only and, hence, carries no information about the off-shell momentum of the top quark, which is on the lower quark line. It is therefore insensitive to the soft scale and does not contribute. Summing all the soft contributions, we get the total soft contribution, $\delta V^S = \sum_{i \in \{b,c,d,e,f\}} \delta V_i^S$, which has the form

$$\delta V^S = \frac{C_F}{8\pi^2} \left(-\frac{\Delta_t}{\mu m_t} \right)^{-2\epsilon} \left[\frac{1}{\epsilon} \left(1 - \ln \left(\frac{(s_{2t} - m_t^2)(s_{4t} - m_t^2)}{m_t^2 s_{24}} \right) \right) \right. $$
$$\left. + 2 + \mathrm{Li}_2 \left(1 - \frac{(s_{2t} - m_t^2)(s_{4t} - m_t^2)}{m_t^2 s_{24}} \right) \right], \tag{5.18}$$

where Li_2 is the dilogarithm function*. By expanding our amplitudes in the soft-momentum region, we have reduced the sum of the one-loop amplitudes to a simple prefactor multiplying the tree-level amplitude.

Now considering the hard-momentum region, $k \sim 1$, we can no longer ignore factors of k in Eq. (5.7). The factor $D_t = p_t^2 - m_t^2 \sim \delta$ is much smaller than any other parameter, however, and so we can expand the integrand in D_t using

$$\frac{1}{(p_t - k)^2 - m_t^2} = \frac{1}{k^2 - 2p_t \cdot k + D_t}$$
$$= \frac{1}{k^2 - 2p_t \cdot k} - \frac{D_t}{(k^2 - 2p_t \cdot k)^2} + \mathcal{O}(D_t^2). \tag{5.19}$$

As $D_t \sim \delta$, we can neglect all terms except the leading term of the expansion in Eq. (5.19). This is equivalent to setting $D_t = p_t^2 - m_t^2 = 0$ in the loop of the amplitude. In other words, we set the top quark on-shell within the loop. This allows us to write

---

*$\mathrm{Li}_2(z) = \sum_{n=1}^{\infty} \frac{z^n}{n^2}$.

the hard contribution to our example diagram as

$$
A^{(3,2),H}_{(-1),d} \sim \frac{1}{\dots D_t} \int \frac{d^d k}{(2\pi)^d} \frac{\dots (\not{p}_t + m_t)\gamma^\mu(\not{p}_t - \not{k} + m_t)\dots(\not{p}_2 - \not{k})\gamma_\mu u(p_2)}{k^2(k^2 - 2p_t \cdot k)(k^2 - 2p_2 \cdot k)} \ . \tag{5.20}
$$

Note that finite-width effects are not resummed in the top-quark propagator which appears inside the integral. This is due to the fact that when the loop-momentum is hard, the top-quark within the loop is not resonant. The top-quark which is not part of the loop is still resonant, however, and the remaining factor of D_t (shown outside of the integral in Eq. (5.20)) must be replaced with Δ_t, as in the soft case. We can again check the overall δ-scaling. Here, the only parameter which scales as $\sim \delta$ is Δ_t. One Δ_t factor remains in the denominator, from the resonant top-quark propagator, and hence, $A^{(3,2),H}_{(-1),d} \sim \delta^{-1}$ which, when combined with the prefactor $g^3_{ew} g^2_s \sim \delta^2$, gives an overall scaling $\sim \delta$, as expected. Performing the integration using standard techniques, the resulting expression splits into a piece which is proportional to the tree-level amplitude and a piece with a different Lorentz structure. That is,

$$
A^{(3,2),H}_{(-1),i} = \delta V^H_i A^{(3,0)}_{(-1)} + \delta A^H_i \ , \tag{5.21}
$$

where δV^H_i is the hard factor for diagram (i) of Figure 4.2 and δA^H_i is the extra piece that does not factorise. All the poles of the diagram are contained within the δV^H_i factor, while the extra piece, δA^H_i, is finite. This split is general for all the hard corrections. As the hard factor comes from the loop integral, and we have seen that the top quark is set on-shell within the loop, the hard factors of our off-shell process are given by the equivalent hard factors of the one-loop diagrams in the on-shell process. Strictly speaking, on-shell here should mean $p^2_t = \mu^2_t$. However, as we are neglecting terms suppressed by $\mathcal{O}(\delta)$, and $\mu^2_t - m^2_t \sim \delta$, we can set $p^2_t = m^2_t$. For our example

diagram, we have

$$\delta V_d^H = \frac{C_F}{8\pi^2} \left[-\frac{1}{2\epsilon^2} + \frac{1}{\epsilon} \left(\ln \left(\frac{s_{2t} - m_t^2}{\mu m_t} \right) - \frac{1}{2} \right) + \text{Li}_2 \left(1 - \frac{m_t^2}{s_{2t} - m_t^2} \right) - 2 \right.$$
$$-\frac{\pi^2}{24} - \frac{1}{2} \ln^2 \left(\frac{s_{2t} - m_t^2}{\mu m_t} \right) + \frac{1}{8} \ln^2 \left(\frac{m_t^2}{\mu^2} \right) + \frac{s_{2t} - m_t^2}{4(2m_t^2 - s_{2t})} \ln \left(\frac{m_t^2}{\mu^2} \right)$$
$$\left. + \ln \left(\frac{s_{2t} - m_t^2}{\mu m_t} \right) \left(1 - \frac{s_{2t} - m_t^2}{2(2m_t^2 - s_{2t})} - \frac{1}{2} \ln \left(\frac{m_t^2}{\mu^2} \right) \right) + \frac{x_{sc}}{2} \right] \tag{5.22}$$

and

$$\delta A_d^H = g_{ew} \sqrt{\frac{1}{2M_W \Gamma_W}} \frac{C_F}{16\pi^2} \frac{[52]\langle 46 \rangle \langle 3|2|1]}{(s_{13} + M_W^2) \Delta_t} \frac{m_t^2}{2m_t^2 - s_{2t}} \ln \left(\frac{s_{2t} - m_t^2}{m_t^2} \right) . \tag{5.23}$$

Here, x_{sc} is the regularisation-scheme parameter, introduced in Section 3.5.

Applying the same method to to diagrams (c)-(f) of Figure 4.2 yields the results given in Eqs. (C.15)-(C.18) and (C.20)-(C.23) of Appendix C. Diagrams (a) and (b) of Figure 4.2 require special treatment and will be discussed later in this section. There are particular points of note regarding the hard amplitudes of diagram (c) and diagram (f) of Figure 4.2. The denominator of diagram (c) contains no factor of the form $(p - k)^2 - m_t^2 = k^2 - 2p \cdot k + D_t$ and thus, no expansion in D_t can be performed. Therefore, the hard contribution to this diagram is equivalent to its full contribution. This was to be expected as it had no soft contribution. Diagram (f) has no hard contribution at the order we are interested in. If the gluon in the diagram were hard, the top quark would no longer be resonant, $D_t \not\sim \delta$, and we would lose a factor of δ from the denominator. This gives the diagram an overall scaling $\sim \delta^2$, which is beyond our target accuracy. This can also be considered in the context of our earlier statement that, at the order we are working at, 'the hard factors of our off-shell process are given by the equivalent hard factors of the one-loop diagrams in the on-shell process'. Diagram (f) contains a gluon which links the production and decay subprocesses and, therefore,

has no analog in the on-shell case. Thus, we would expect its hard contribution to vanish at the order we are working.

If we now consider diagram (b) of Figure 4.2 and try to follow the above prescription, the scaling problem, introduced in Section 4.3, soon becomes evident. The expression for the amplitude of the diagram has the form

$$A_{(-1),b}^{(3,2)} \sim \int \frac{d^d k}{(2\pi)^d} \frac{\dots (\not{p}_t + m_t) \dots (\not{p}_t - \not{k} + m_t) \dots (\not{p}_t + m_t) \dots}{\dots k^2(p_t^2 - m_t^2)\left((p_t - k)^2 - m_t^2\right)(p_t^2 - m_t^2)}$$

$$= \int \frac{d^d k}{(2\pi)^d} \frac{\dots (\not{p}_t + m_t) \dots (\not{p}_t - \not{k} + m_t) \dots (\not{p}_t + m_t) \dots}{\dots k^2 D_t^2(k^2 - 2p_t \cdot k + D_t)} \,. \tag{5.24}$$

Expanding the denominator in D_t, using Eq. (5.19), we obtain

$$\frac{1}{D_t^2(k^2 - 2p_t \cdot k + D_t)} = \frac{1}{D_t^2(k^2 - 2p_t \cdot k)} - \frac{1}{D_t(k^2 - 2p_t \cdot k)^2} + \mathcal{O}(1) \,. \tag{5.25}$$

The first term scales as $\sim \delta^{-2}$ and the second as $\sim \delta^{-1}$, all other terms can be neglected at the order we are working to. When combined with the rest of the amplitude, which scales as ~ 1, and the overall prefactor $g_{ew}^3 g_s^2 \sim \delta^2$, we obtain two scales for the diagram. The part coming from the second term of Eq. (5.25) scales as $\sim \delta$, which is the expected scaling of the diagram. The part coming from the first term scales as ~ 1, however. This represents a 'superleading' contribution, i.e. it is even more important in our counting than the LO contribution, which scales as $\sim \delta^{1/2}$. This is in agreement with our earlier results. This 'superleading' contribution will be cancelled out exactly by the top-quark self-energy counterterm. This is shown in the next section.

The scaling of diagram (a) of Figure 4.2 is obtained in the same way as that of diagram (b), replacing the strong couplings, g_s, with electroweak couplings, g_{ew}. As in the case of diagram (b), we obtain two scales. The leading contribution scales as $\sim \delta^{1/2}$,

with the subleading contribution scaling as $\sim \delta^{3/2}$. The subleading contribution shows the scaling expected from our counting and constitutes an effect of higher order than we are aiming for. Therefore, it can be neglected. The leading contribution, however, has the same scaling as our LO diagram and must be resummed. This is described in Sections 4.2 and 5.4, and in Appendix A.

By expanding the one-loop diagrams in the soft- and hard-momentum regions, significant simplifications have been made to the calculation. A good illustration of this is diagram (f) of Figure 4.2. Rather than having to calculate the full box diagram, we require only the soft part, which is more straightforward to calculate. We have also seen that the hard contributions are linked to the one-loop amplitudes of the on-shell NWA calculation, while the soft contributions contain the off-shell effects.

5.4 Renormalisation and Resummation

In the previous section, we saw that diagrams (a) and (b) of Figure 4.2 contain terms which contribute at 'superleading' and leading order respectively. This appears to be a problem as these NLO diagrams should be suppressed with respect to the LO diagram in our counting. These problems can be solved using renormalisation and resummation, however.

As discussed in Section 2.3, when we perform an NLO calculation we must use renormalisation. This renormalisation introduces counterterms to the Feynman diagrams which we must include. Using the on-shell scheme, and with NLO defined as diagrams suppressed by a factor α_s with respect to LO, the only relevant, non-zero counterterms are those of the top-quark self-energy and the Wtb-vertex corrections. These are shown in Figure 5.3.
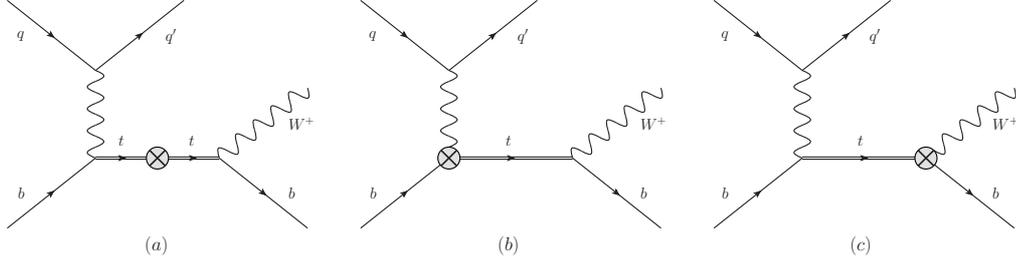
Figure 5.3: The counterterm diagrams required to calculate the NLO cross section of the hard-scattering process in Eq. (4.3) to $\mathcal{O}(\delta^{3/2})$ in the on-shell renormalisation scheme.

If we take the expression for the amplitude of the one-loop QCD self-energy correction to the top-quark propagator, appearing in diagram (b) of Figure 4.2,

$$\frac{i(\not{p}_t + m_t)}{D_t} \left(-4\pi\alpha_s C_F \tilde{\mu}^{2\epsilon} \int \frac{d^d k}{(2\pi)^d} \frac{\gamma^\rho(\not{p}_t - \not{k} + m_t)\gamma_\rho}{k^2(k^2 - 2p_t \cdot k + D_t)} \right) \frac{i(\not{p}_t + m_t)}{D_t}, \qquad (5.26)$$

expand in D_t and integrate in the hard-momentum region, we obtain

$$\frac{\alpha_s C_F}{2\pi} \left[\frac{3}{2\epsilon} + 2 + \frac{x_{sc}}{2} \right] \left(\frac{m_t^2}{\mu^2} \right)^{-\epsilon} \left[\frac{2im_t^2(\not{p}_t + m_t)}{D_t^2} + \frac{im_t}{D_t} - \frac{i(\not{p}_t + m_t)}{D_t} \right]. \qquad (5.27)$$

Here we can clearly observe the 'superleading' term, with the double power of D_t in the denominator, and the subleading terms, with the single power of D_t in the denominator, which scale as we expected. If we now consider the top-quark self-energy counterterm, diagram (a) in Figure 5.3, and look at the correction to the top-quark propagator, by using the counterterm expression, shown in Figure 2.2, in the on-shell renormalisation scheme, we get

$$\frac{i(\not{p}_t + m_t)}{D_t} \left(i(\not{p}_t - m_t)\delta Z_t^{\mathrm{OS}} - i\delta m_t^{\mathrm{OS}} \right) \frac{i(\not{p}_t + m_t)}{D_t}. \qquad (5.28)$$

Using Eq. (5.12) and simplifying, this becomes

$$\delta m_t^{\text{OS}} \left(\frac{2im_t(\not{p}_t + m_t)}{D_t^2} + \frac{i}{D_t} \right) - \delta Z_t^{\text{OS}} \left(\frac{i\,(\not{p}_t + m_t)}{D_t} \right) . \tag{5.29}$$

Using Eq. (2.14), along with the expression for the top-quark self-energy to order α_s [49], discussed later, we find

$$\delta m_t^{\text{OS}} = -\frac{\alpha_s C_F}{2\pi} m_t \left[\frac{3}{2\epsilon} + 2 + \frac{x_{sc}}{2} \right] \left(\frac{m_t^2}{\mu^2} \right)^{-\epsilon} , \tag{5.30}$$

$$\delta Z_t^{\text{OS}} = \frac{\delta m_t^{\text{OS}}}{m_t} = -\frac{\alpha_s C_F}{2\pi} \left[\frac{3}{2\epsilon} + 2 + \frac{x_{sc}}{2} \right] \left(\frac{m_t^2}{\mu^2} \right)^{-\epsilon} . \tag{5.31}$$

Combining these expressions with Eq. (5.29), the contribution of the top-quark self-energy counterterm to the top-quark propagator is given by

$$-\frac{\alpha_s C_F}{2\pi} \left[\frac{3}{2\epsilon} + 2 + \frac{x_{sc}}{2} \right] \left(\frac{m_t^2}{\mu^2} \right)^{-\epsilon} \left[\frac{2im_t^2(\not{p}_t + m_t)}{D_t^2} + \frac{im_t}{D_t} - \frac{i(\not{p}_t + m_t)}{D_t} \right] , \tag{5.32}$$

which exactly cancels that of the top-quark self-energy diagram, Eq. (5.27). Here, the counterterm diagram cancels not only the 'superleading' term, but also the two subleading terms. The 'superleading' terms are, in fact, cancelled by the mass renormalisation only (as required by Eq. (A.13)). The inclusion of the wavefunction renormalisation leads to the cancellation of the remaining contributions. It is important to note that the exact cancellation of the 'superleading' term with the counterterm is not general for any renormalisation scheme. In a generic scheme, these terms must be resummed into the top-quark propagator. A detailed discussion of this can be found in Appendix A.

Although we have solved the problem of the 'superleading' terms, we must still continue with our calculation and include all relevant counterterms. The calculation

of the Wtb-vertex correction counterterms (diagrams (b) and (c) of Figure 5.3) is more straightforward, however. Taking the counterterm expression, shown in Figure 2.2, in the on-shell scheme, this is just the standard Wtb-vertex Feynman rule with an extra factor of $\delta Z_t^{\mathrm{OS}}/2$. Hence, it acts only as an overall multiplicative factor to the tree-level amplitude. Thus, the amplitude for each of the diagrams is given by

$$A_{(-1),ct(b)}^{(3,2)} = A_{(-1),ct(c)}^{(3,2)} = \frac{\delta Z_t^{\mathrm{OS}}}{2} A_{(-1)}^{(3,0)} . \tag{5.33}$$

Combining the top-quark self-energy diagram with these three counterterms, we can write the contribution to the amplitude in the same form as those given in Section 5.3, see Eq. (5.21). We find

$$\delta V_{b+ct}^{H} = \frac{C_F}{8\pi^2} \left[-\frac{3}{2\epsilon} + \frac{3}{2} \ln \left(\frac{m_t^2}{\mu^2} \right) - 2 - \frac{x_{sc}}{2} \right] , \tag{5.34}$$

$$\delta A_{b+ct}^{H} = 0 , \tag{5.35}$$

where the subscript $b+ct$ indicates that this contribution to the amplitude contains that of diagram (b) of Figure 4.2, plus the three counterterm diagrams shown in Figure 5.3. It is worth noting that this result can also be obtained in a more straightforward way, as outlined in Section 3.3 of Ref. [22]. The fact that the top quark appears only as an internal line in the Feynman diagrams means that its wavefunction renormalisation can be ignored, i.e. $\delta Z_t^{\mathrm{OS}} = 0$, leaving only the mass renormalisation in the self-energy counterterm and removing the Wtb-vertex counterterms. The mass renormalisation in the self-energy counterterm exactly cancels the 'superleading' terms, as observed earlier, leaving the remaining terms as contributions to the amplitude. In our earlier method, these contributions were cancelled out by the wavefunction renormalisation

terms in the self-energy counterterm but then added back in the form of the Wtb-vertex counterterms. For calculations using the NWA treatments, the top quark appears as an external particle in the production and decay subprocesses and, therefore, the wavefunction renormalisation of the top quark is required. Hence, it is more illustrative to leave in the wavefunction renormalisation in the off-shell calculation for comparison to the on-shell, NWA treatments, given later.

Using renormalisation, we have removed the 'superleading' terms coming from diagram (b) of Figure 4.2. However, we still have the leading terms which arise from the hard contribution of diagram (a). These are included via the resummation of the top-quark propagator. As discussed in Section 4.2, we must modify the propagator to have the form

$$
\frac{i}{\not{p}_t - m_t} \rightarrow \frac{i}{\not{p}_t - m_t - \bar{\Sigma}_t(\not{p}_t)} \rightarrow \frac{i}{\not{p}_t - \mu_t} \,. \tag{5.36}
$$

To calculate $\bar{\Sigma}_t(\not{p}_t)$, and hence μ_t, to the required accuracy, we must consider all corrections to the top-quark propagator which are suppressed by orders up to and including δ. These are the one-loop QCD self-energy (diagram (b) of Figure 4.2), which has a suppression $\sim \alpha_s \sim \delta^{1/2}$; the one-loop electroweak self-energies (diagram (a) of Figure 4.2, plus the diagrams with a Z-boson and a photon, rather than a W-boson, in the loop), which have a suppression $\sim \alpha_{ew} \sim \delta$; and the two-loop QCD contribution, which has a suppression $\sim \alpha_s^2 \sim \delta$. Using a general renormalisation scheme, we would have to calculate the contributions of all of these diagrams in order to define m_t and Γ_t, which appear in the definition of μ_t. However, as we saw earlier, by choosing the on-shell scheme we can simplify this somewhat. As shown at the beginning of this section, we get an exact cancellation between the 'superleading' terms of the one-loop QCD self-energy diagram and the top-quark self-energy counterterm. A similar can-

cellation is also present at two-loops in QCD. This is shown in Appendix A. Therefore, we need not include these two diagrams in our calculation of $\bar{\Sigma}_t(\not{p}_t)$. The number of electroweak self-energy diagrams to be included can also be reduced. In the on-shell scheme, only the imaginary part of the one-loop contributions is effectively resummed (see Appendix A). The only one-loop electroweak self-energy diagram which has an imaginary part is the one which has a W-boson in the loop. Hence, we may also neglect the diagrams containing a Z-boson and a photon. The only diagram which contributes to $\bar{\Sigma}_t(\not{p}_t)$ is, therefore, the one shown in diagram (a) of Figure 4.2. Resumming this diagram gives us our definition, $\mu_t^2 = m_t^2 - i m_t \Gamma_t$, with m_t the on-shell top-quark mass and Γ_t the on-shell top-quark decay-width. By using the resummed top-quark propagator in the amplitudes of the other diagrams, we automatically include diagram (a) of Figure 4.2 and thus do not need a separate expression for its amplitude. We now have all the one-loop amplitudes required for the calculation.

5.5 Real Amplitudes

The real diagrams required to calculate the cross section to NLO in our counting are shown in Figures 4.3 and 4.4. These can be split into diagrams which represent the resonant tree-level diagram with an extra gluon emitted, Figure 4.3, which we refer to as $\mathcal{A}_{qb}^{\text{Real}}$, and gluon-initiated diagrams, Figure 4.4, which we refer to as $\mathcal{A}_{gb}^{\text{Real}}$ and $\mathcal{A}_{qg}^{\text{Real}}$. Here $\mathcal{A}_{gb}^{\text{Real}}$ are the amplitudes of the diagrams with the initial-state gluon on the upper quark line, shown in diagram (a) of Figure 4.4, and $\mathcal{A}_{qg}^{\text{Real}}$ are those with the initial-state gluon on the lower quark line, shown in diagrams (b)-(d) of Figure 4.4. The amplitude for the gluon-emission diagrams can be written as

$$\mathcal{A}_{qb}^{\text{Real}}(g_7^{\pm}) = \delta_{c_4 c_2} t_{c_3 c_1}^{A_7} g_{ew}^3 g_s A_{(-1),[31]}^{(3,1)}(g_7^{\pm}) + \delta_{c_3 c_1} t_{c_4 c_2}^{A_7} g_{ew}^3 g_s A_{(-1),[42]}^{(3,1)}(g_7^{\pm}), \qquad (5.37)$$

where c_i is the colour index of external quark, i, A_7 is the colour index of the emitted gluon and $g^\pm$ denotes the two possible helicity states of the emitted gluon. The amplitudes $A^{(3,1)}_{(-1),[31]}$ and $A^{(3,1)}_{(-1),[42]}$ are the contributions of diagrams with a gluon emitted from the upper quark line, shown in diagrams (a) and (b) in Figure 4.3, and lower quark line, shown in diagrams (c)-(e) in Figure 4.3, respectively. The contributions of the diagrams with a gluon emitted from the upper quark line are given by

$$A^{(3,1)}_{(-1),[31]}(g_7^+) = g_{ew}\sqrt{\frac{1}{2M_W\Gamma_W}}\frac{\sqrt{2}\,\langle 46\rangle\,\langle 3|4+6|5]\,\langle 3|7-1|2]}{(s_{137}+M_W^2)\Delta_t\,\langle 17\rangle\langle 37\rangle},$$

$$A^{(3,1)}_{(-1),[31]}(g_7^-) = -g_{ew}\sqrt{\frac{1}{2M_W\Gamma_W}}\frac{\sqrt{2}\,\langle 46\rangle[12]\,[1|3+7|4+6|5]}{(s_{137}+M_W^2)\Delta_t\,[17][37]}, \qquad (5.38)$$

where $s_{137} = s_{13} + s_{17} - s_{37}$. For the lower quark line emission we obtain

$$A^{(3,1)}_{(-1),[42]}(g_7^+) = -g_{ew}\sqrt{\frac{1}{2M_W\Gamma_W}}\frac{\sqrt{2}\langle 46\rangle}{(s_{13}+M_W^2)\Delta_t}\left(\frac{\langle 3|4+6|5]\langle 4|7-2|1]}{\langle 27\rangle\langle 47\rangle}\right.$$
$$\left.+\frac{[12]}{\langle 47\rangle}\frac{\langle 3|1+2|7]\langle 4|6|5]-\mu_t^2\langle 34\rangle[57]}{\Delta_{t7}}\right),$$

$$A^{(3,1)}_{(-1),[42]}(g_7^-) = -g_{ew}\sqrt{\frac{1}{2M_W\Gamma_W}}\frac{\sqrt{2}\,[12]}{(s_{13}+M_W^2)\Delta_{t7}}\left(\frac{\langle 3|1+2|5]\langle 6|4+7|2]}{[27][47]}\right.$$
$$\left.-\frac{\langle 46\rangle}{[27]}\frac{\langle 3|1|2]\langle 7|4+6|5]+\mu_t^2\langle 37\rangle[25]}{\Delta_t}\right), \qquad (5.39)$$

with $\Delta_{t7} = (p_t + p_7)^2 - \mu_t^2$. It can clearly be seen from Eq. (5.39) that, as mentioned in Section 4.4, the amplitudes can become enhanced in two different kinematic regions. The region where $\Delta_t \sim \delta$, which corresponds to the usual resonant top-quark region, but also the region where $\Delta_{t7} \sim \delta$. It should also be noted that the μ_t^2 factor in the numerator of Eq. (5.39) could be replaced with a factor m_t^2 instead. As discussed for the hard loop-corrections in Section 4.3, making this replacement leads to a violation of gauge-invariance which is of the order $\sim \delta$ and is thus a higher-order effect in our

counting. Choosing to use the factor μ_t^2 guarantees that the QCD Ward identities are satisfied, however. The amplitudes for the gluon-initiated diagrams, $\mathcal{A}_{gb}^{\text{Real}}$ and $\mathcal{A}_{qg}^{\text{Real}}$, can be obtained by crossing the momenta of Eqs. (5.38) and (5.39) respectively.

5.6 Cancellation of Poles

We now have expressions for all the amplitudes required for our calculation. Before we can begin to calculate cross sections and kinematic distributions, however, we must consider the cancellation of poles. As discussed in Sections 3.2 and 3.3, the poles coming from the virtual diagrams must be cancelled exactly by those from the real diagrams. The poles coming from the virtual diagrams are already explicit in the amplitude expressions, given in Appendix C. To cancel these analytically, we need to make the poles in the real amplitudes explicit. Following the method of Catani and Seymour [64], as outlined in Section 3.3, we must consider the $\boldsymbol{I}$ insertions, as these contain all the explicit poles. For our process, the general expression for $\boldsymbol{I}$ is

$$\boldsymbol{I} = \frac{\alpha_s C_F}{2\pi} \sum_i \sum_{j \neq i} \left(\frac{1}{\bar{\epsilon}^2} + \frac{3}{2\bar{\epsilon}} + 5 - \frac{7\pi^2}{12} - \frac{x_{sc}}{2} \right) \left(\frac{\tilde{\mu}^2}{2p_i \cdot p_j} \right)^\epsilon , \qquad (5.40)$$

where i and j are external quarks on the same fermion line. The equation has been put into a form consistent with those of the virtual corrections, containing the factor $\tilde{\mu}^{2\epsilon}$ and $\bar{\epsilon}$-poles[†]. After expansion in ϵ, these combine to leave only ϵ-poles. These can then be subtracted in the $\overline{\text{MS}}$ scheme, as explained in Section 5.3. Performing the sum over the external quarks, we obtain

$$\boldsymbol{I} = \boldsymbol{I}_{[31]} + \boldsymbol{I}_{[42]} , \qquad (5.41)$$

[†]Here, $\dfrac{1}{\bar{\epsilon}^2} = \dfrac{1}{\epsilon^2} \, e^{-\epsilon \gamma_E} (4\pi)^\epsilon$.

where

$$\boldsymbol{I}_{[31]} = \frac{\alpha_s C_F}{\pi} \left[\frac{1}{\epsilon^2} - \frac{1}{\epsilon} \left(\ln \left(\frac{s_{13}}{\mu^2} \right) - \frac{3}{2} \right) - \frac{x_{sc}}{2} \right] + \mathcal{O}(1) \qquad (5.42)$$

is the contribution from the diagrams with the gluon emitted from the upper quark line, and

$$\boldsymbol{I}_{[42]} = \frac{\alpha_s C_F}{\pi} \left[\frac{1}{\epsilon^2} - \frac{1}{\epsilon} \left(\ln \left(\frac{s_{24}}{\mu^2} \right) - \frac{3}{2} \right) - \frac{x_{sc}}{2} \right] + \mathcal{O}(1) \qquad (5.43)$$

is the contribution from the diagrams with the gluon emitted from the lower quark line. We show only the poles and the dependence on the regularisation-scheme parameter, x_{sc}, as it will be instructive to see how these are cancelled by the virtual terms. Full expressions, including the finite terms, can be found in Appendix D. The structure of our amplitudes allows us to deal with the upper and lower quark lines separately. The gluon-initiated diagrams do not contain any explicit ϵ-poles and so are ignored here.

Taking the one-loop amplitudes from Appendix C, considering only the parts containing poles and the regularisation-scheme parameter, and combining them, we find

$$\delta V_{[31]}^S = \delta V_{(c)}^S = 0 \,, \qquad (5.44)$$

$$\delta V_{[42]}^S = \frac{C_F}{8\pi^2} \left[\frac{1}{\epsilon} \left(1 - \ln \left(\frac{(s_{2t} - m_t^2)(s_{4t} - m_t^2)}{m_t^2 s_{24}} \right) \right) \right] + \mathcal{O}(1) \qquad (5.45)$$

for the soft contributions to the upper and lower quark lines respectively, and

$$\delta V_{[31]}^H = \frac{C_F}{8\pi^2} \left[-\frac{1}{\epsilon^2} + \frac{1}{\epsilon} \left(\ln\left(\frac{s_{13}}{\mu^2}\right) - \frac{3}{2} \right) + \frac{x_{sc}}{2} \right] + \mathcal{O}(1), \tag{5.46}$$

$$\delta V_{[42]}^H = \frac{C_F}{8\pi^2} \left[-\frac{1}{\epsilon^2} + \frac{1}{\epsilon} \left(\ln\left(\frac{(s_{2t} - m_t^2)(s_{4t} - m_t^2)}{\mu^2 m_t^2}\right) - \frac{5}{2} \right) + \frac{x_{sc}}{2} \right] + \mathcal{O}(1) \tag{5.47}$$

for the hard contributions. Combining the soft and hard contributions gives

$$\delta V_{[31]} = \frac{C_F}{8\pi^2} \left[-\frac{1}{\epsilon^2} + \frac{1}{\epsilon} \left(\ln\left(\frac{s_{13}}{\mu^2}\right) - \frac{3}{2} \right) + \frac{x_{sc}}{2} \right] + \mathcal{O}(1), \tag{5.48}$$

$$\delta V_{[42]} = \frac{C_F}{8\pi^2} \left[-\frac{1}{\epsilon^2} + \frac{1}{\epsilon} \left(\ln\left(\frac{s_{24}}{\mu^2}\right) - \frac{3}{2} \right) + \frac{x_{sc}}{2} \right] + \mathcal{O}(1). \tag{5.49}$$

It can clearly be seen that the pole structure of Eqs. (5.48) and (5.49) matches those of Eqs. (5.42) and (5.43) respectively. To see the full cancellation, we must consider the squared matrix-elements. Using the fact that $\mathcal{M}^{\text{Virtual}} = g_{ew}^6 g_s^2 \, 2\,\text{Re}\left[A_{(-1)}^{(3,2)} \left(A_{(-1)}^{(3,0)} \right)^* \right]$, along with Eqs. (5.14) and (5.21), we find that

$$d\sigma_{[31]}^V = \frac{\alpha_s C_F}{\pi} \left[-\frac{1}{\epsilon^2} + \frac{1}{\epsilon} \left(\ln\left(\frac{s_{13}}{\mu^2}\right) - \frac{3}{2} \right) + \frac{x_{sc}}{2} \right] d\sigma^B + \mathcal{O}(1), \tag{5.50}$$

$$d\sigma_{[42]}^V = \frac{\alpha_s C_F}{\pi} \left[-\frac{1}{\epsilon^2} + \frac{1}{\epsilon} \left(\ln\left(\frac{s_{24}}{\mu^2}\right) - \frac{3}{2} \right) + \frac{x_{sc}}{2} \right] d\sigma^B + \mathcal{O}(1), \tag{5.51}$$

where $d\sigma^B$ is the tree-level differential cross section. Using these expressions, along with those for the real insertions, Eqs. (5.42) and (5.43), in Eq. (3.17), it is clear to see that the poles, and the dependence on x_{sc}, cancel exactly. We can then set $\epsilon = 0$ in the integrand and perform the integration numerically.
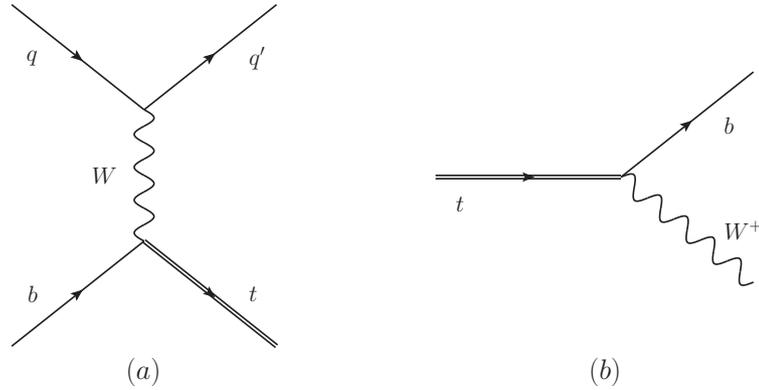
Figure 5.4: The tree-level Feynman diagrams for the *t*-channel production (a) and the decay (b) of an on-shell top quark.

5.7 Comparison of Heavy-Particle Treatments

Hitherto, the results given in this chapter have been for the off-shell treatment of the top quark, as this is the focus of the thesis. However, in order to assess the importance of the extra effects this treatment includes, we must compare our results to those obtained using an alternative, on-shell treatment. These alternative treatments are discussed in Section 3.4. In this section, we will consider the diagrams needed to calculate the cross section in each case and also see how the cancellation of poles changes from treatment to treatment.

By setting the top quark to be on its mass shell, we can decouple the overall process into separate production and decay subprocesses. The tree-level Feynman diagrams for the two processes are shown in diagrams (a) and (b) of Figure 5.4 respectively. In the stable production and NWA treatments, the amplitudes of production and decay are calculated separately, whereas in the iNWA the amplitude is given by that of the off-shell treatment, Eq. (5.2), with the top-quark propagator removed and the top-quark momentum set on-shell[‡]. As the separate production and decay subprocesses contain

---

[‡] $\mathcal{A}_{\text{iNWA}} = \Delta_t \mathcal{A}_{\text{off}-\text{shell}}\big|_{p_t^2 = m_t^2}$.
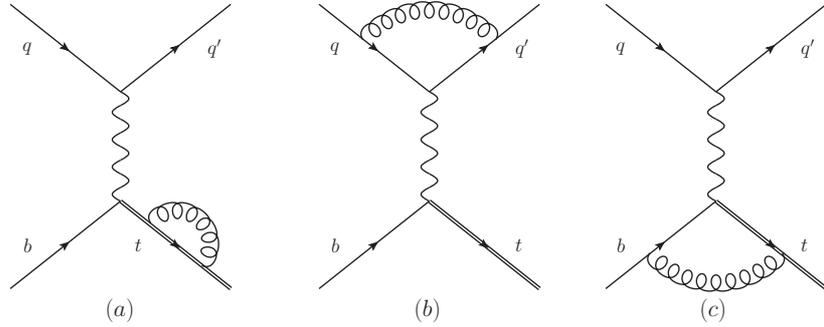
Figure 5.5: The one-loop Feynman diagrams contributing to the t-channel production of an on-shell top quark.

massive external particles, we do not use the helicity notation for their amplitudes. The appropriate squared matrix-elements or amplitudes for the various on-shell treatments, at tree level, are;

$$\mathcal{M}_{\text{prod}}^{\text{tree}} = g_{ew}^4 \frac{s_{12}(s_{3t} - m_t^2)}{(s_{13} + M_W^2)^2} , \tag{5.52}$$

$$\mathcal{M}_{\text{dec}}^{\text{tree}} = g_{ew}^4 \frac{1}{2M_W \Gamma_W} \frac{s_{46}(s_{5t} - m_t^2)}{2} , \tag{5.53}$$

$$\mathcal{A}_{\text{iNWA}}^{\text{tree}} = g_{ew}^4 \sqrt{\frac{1}{2M_W \Gamma_W}} \frac{[12]\langle 46\rangle\langle 3|4 + 6|5]}{(s_{13} + M_W^2)} , \tag{5.54}$$

with $p_t^2 = (p_4 + p_5 + p_6)^2 = m_t^2$ and $p_W^2 = (p_5 + p_6)^2 = M_W^2$, while for the off-shell treatment we have

$$\mathcal{A}_{\text{off-shell}}^{\text{tree}} = g_{ew}^4 \sqrt{\frac{1}{2M_W \Gamma_W}} \frac{[12]\langle 46\rangle\langle 3|4 + 6|5]}{(s_{13} + M_W^2)\,\Delta_t} . \tag{5.55}$$

Moving on to the diagrams which contribute at NLO, the virtual corrections to the production and decay subprocesses are shown in Figures 5.5 and 5.7 respectively, and the associated counterterm diagrams in Figures 5.6 and 5.8. Comparing these diagrams
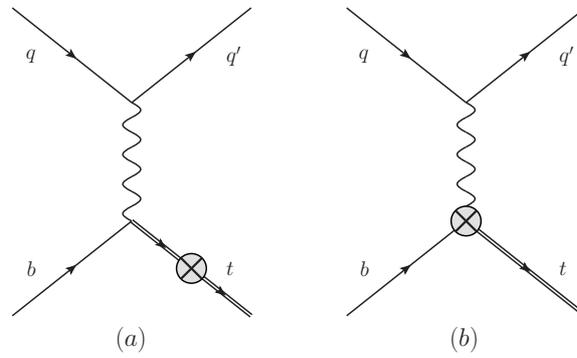
Figure 5.6: The Feynman counterterm diagrams contributing to the t-channel production of an on-shell top quark.
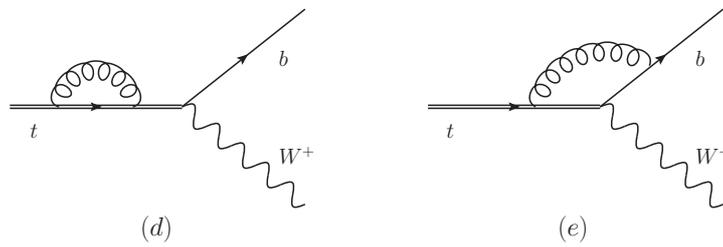
Figure 5.7: The one-loop Feynman diagrams contributing to the decay of an on-shell top quark.
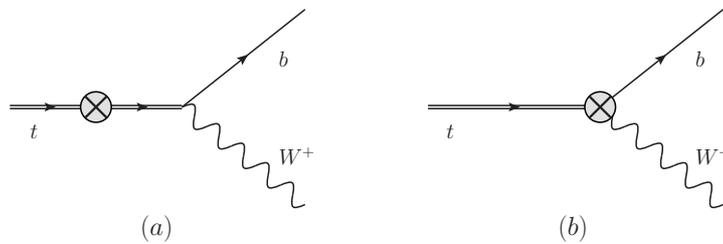
Figure 5.8: The Feynman counterterm diagrams contributing to the decay of an on-shell top quark.

to those required for the off-shell treatment, shown in Figure 4.2, we can see that we no longer have a diagram with a gluon linking the production and decay subprocesses (like diagram (f) in Figure 4.2), and the gluon loop, which was on the intermediate top-quark propagator in the off-shell case, splits into two diagrams, each containing a gluon loop on the external top-quark leg. The amplitudes of these diagrams can be calculated in a straightforward manner. Again, for the iNWA, the amplitudes can be obtained from those of the off-shell treatment by removing the top-quark propagator and setting the top-quark momentum on-shell. As the top quark is on-shell, only the hard contributions to the cross section are required. In all cases, we can still factorise the amplitudes into a pole-containing factor which multiplies the corresponding tree-level amplitude, plus a finite piece. The pole-containing factors are independent of the treatment being used. That is,

$$A_{X,i}^H = \delta V_i^H A_X^{\text{tree}} + \delta A_{X,i}^H. \tag{5.56}$$

Hence, the amplitude of diagram (c) in Figure 5.5, in the stable on-shell production treatment, is given by

$$A_{\text{prod},c}^{\text{Virtual}} = \delta V_c \, A_{\text{prod}}^{\text{tree}} + \delta A_{\text{prod},c}, \tag{5.57}$$

where we have dropped the H subscript as the on-shell treatments contain only hard contributions. The pole-containing factor is

$$
\begin{aligned}
\delta V_c = \frac{C_F}{8\pi^2} \Bigg[&-\frac{1}{2\epsilon^2} + \frac{1}{\epsilon}\left(\ln\left(\frac{s_{2t} - m_t^2}{\mu m_t} \right) - \frac{1}{2} \right) + \text{Li}_2\left(1 - \frac{m_t^2}{s_{2t} - m_t^2} \right) - 2 \\
&- \frac{\pi^2}{24} - \frac{1}{2}\ln^2\left(\frac{s_{2t} - m_t^2}{\mu m_t} \right) + \frac{1}{8}\ln^2\left(\frac{m_t^2}{\mu^2} \right) + \frac{s_{2t} - m_t^2}{4(2m_t^2 - s_{2t})}\ln\left(\frac{m_t^2}{\mu^2} \right) \\
&+ \ln\left(\frac{s_{2t} - m_t^2}{\mu m_t} \right)\left(1 - \frac{s_{2t} - m_t^2}{2(2m_t^2 - s_{2t})} - \frac{1}{2}\ln\left(\frac{m_t^2}{\mu^2} \right) \right) + \frac{x_{sc}}{2} \Bigg],
\end{aligned}
\tag{5.58}
$$

which is identical to the pole-containing factor of the hard contribution to the corresponding diagram in the off-shell treatment (diagram (d) in Figure 4.2), given in Eq. (5.22). Therefore, we already have all the explicit poles coming from the on-shell virtual diagrams in our off-shell amplitudes. They are given by

$$A^{\text{Virtual}}_{\text{prod},[31]} = \delta V_b \, A^{\text{tree}}_{\text{prod}} + \delta A_{\text{prod},[31]} \,, \tag{5.59}$$

$$A^{\text{Virtual}}_{\text{prod},[42]} = (\delta V_{a+ct} + \delta V_c) \, A^{\text{tree}}_{\text{prod}} + \delta A_{\text{prod},[42]} \,, \tag{5.60}$$

$$A^{\text{Virtual}}_{\text{dec},[42]} = (\delta V_{d+ct} + \delta V_e) \, A^{\text{tree}}_{\text{dec}} + \delta A_{\text{dec},[42]} \,, \tag{5.61}$$

for the upper quark line and production and decay parts of the lower quark line respectively. The δV_i factors, corresponding to diagram (i) of Figures 5.5 and 5.7, are linked to the general δV^H factors, given in Eqs. (C.20)-(C.22) of Appendix C, by

$$\delta V_b = \delta V^H_{[31]}, \quad \delta V_c = \delta V^H_{[2t]}, \quad \delta V_e = \delta V^H_{[4t]}, \quad \delta V_{a+ct} = \delta V_{d+ct} = \frac{\delta V^H_{se+ct}}{2} \,. \tag{5.62}$$

For the self-energy diagrams plus the appropriate counterterms, we have an exact cancellation between the top-quark self-energy diagram and the top-quark self-energy counterterm, as was shown in Section 5.4 for the off-shell treatment. The remaining contribution is due to the Wtb-vertex counterterm only. As the production and decay subprocesses each have only one diagram containing such a counterterm, compared to two diagrams for the full process, this leads the overall factor of 1/2 multiplying δV^H_{se+ct}. The finite δA factors must be calculated separately for each treatment.

The Feynman diagrams required to calculate the real contribution to the cross section at NLO are shown in Figures 5.9 - 5.11. Comparing these to the real diagrams for
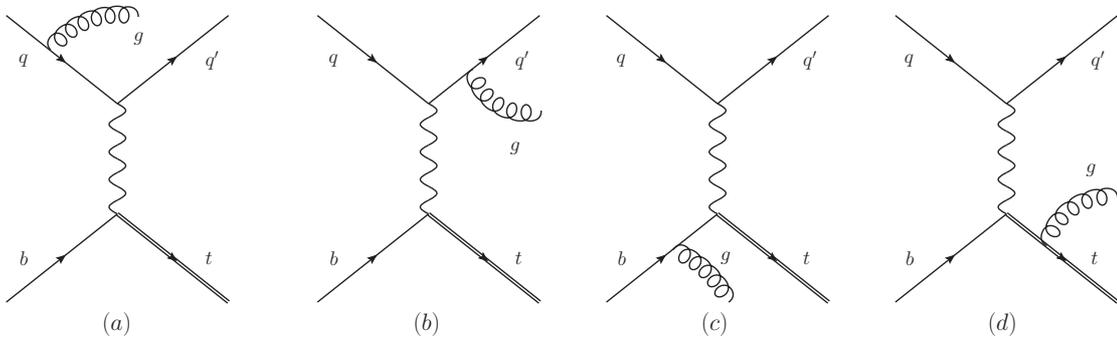
Figure 5.9: The real gluon-emission Feynman diagrams contributing to the *t*-channel production of an on-shell top quark.
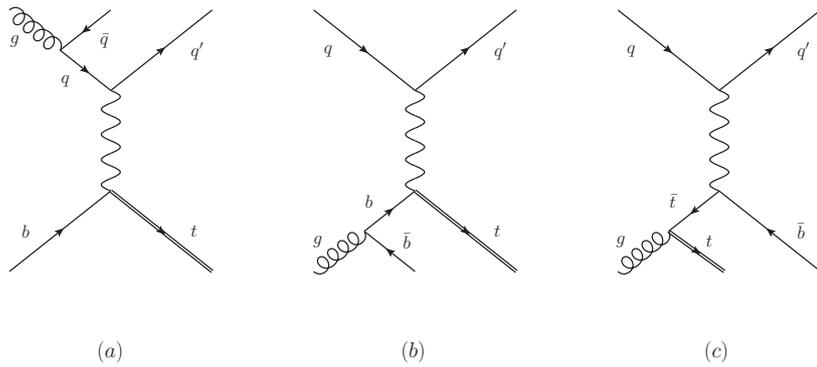
Figure 5.10: The real gluon-initiated Feynman diagrams contributing to the *t*-channel production of an on-shell top quark.
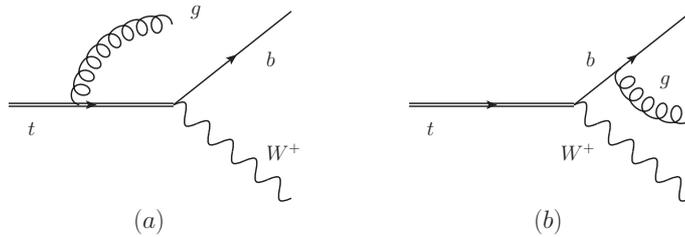
Figure 5.11: The real Feynman diagrams contributing to the decay of an on-shell top quark.

the off-shell process, shown in Figures 4.3 and 4.4, we can see that the off-shell diagram in which a gluon is emitted from the intermediate top-quark (diagram (d) of Figure 4.3) is replaced by two diagrams containing a gluon emitted from the external top-quark leg. There are also fewer gluon-initiated diagrams with the gluon on the lower quark line. Again, the amplitudes of these diagrams can be calculated in a straightforward manner. Making the poles of these diagrams explicit is less straightforward, however. We follow the method of Catani and Seymour, as outlined in Section 3.3, once more. The presence of a massive external-particle makes the calculation of the required dipoles more complicated. For the production process, where the massive particle is in the final state, we follow the prescription outlined in Ref. [72], while for the decay process, with the massive particle in the initial state, we follow the method given in Ref. [35]. The I insertion for the upper quark line, $I_{[31]}$, is unchanged as the splitting of the process into a production and decay subprocess occurs on the lower quark line. Therefore, the cancellation of the upper line poles follows in exactly the same way as in the off-shell case, see Eqs (5.42) and (5.48). For the lower quark line, we split the insertions into a production-process insertion, $I_{\text{prod},[42]}$, and a decay-process insertion, $I_{\text{dec},[42]}$. Taking the results from Appendix D, showing only the poles and regularisation-scheme parameter explicitly, we have

$$I_{\text{prod},[42]} = \frac{\alpha_s C_F}{2\pi} \left[\frac{1}{\epsilon^2} - \frac{1}{\epsilon} \left(2\ln\left(\frac{s_{2t} - m_t^2}{\mu m_t}\right) - \frac{5}{2} \right) - \frac{x_{sc}}{2} \right] + \mathcal{O}(1), \qquad (5.63)$$

$$I_{\text{dec},[42]} = \frac{\alpha_s C_F}{2\pi} \left[\frac{1}{\epsilon^2} - \frac{1}{\epsilon} \left(2\ln\left(\frac{s_{4t} - m_t^2}{\mu m_t}\right) - \frac{5}{2} \right) - \frac{x_{sc}}{2} \right] + \mathcal{O}(1). \qquad (5.64)$$

Comparing these expressions with those coming from the virtual corrections, given in Eqs. (5.60) and (5.61), which lead to

$$d\sigma^V_{\text{prod},[42]} = \frac{\alpha_s C_F}{2\pi} \left[-\frac{1}{\epsilon^2} + \frac{1}{\epsilon}\left(2\ln\left(\frac{s_{2t} - m_t^2}{\mu m_t}\right) - \frac{5}{2}\right) + \frac{x_{sc}}{2} \right] d\sigma^B_{\text{prod}} + \mathcal{O}(1)\,, \quad (5.65)$$

$$d\sigma^V_{\text{dec},[42]} = \frac{\alpha_s C_F}{2\pi} \left[-\frac{1}{\epsilon^2} + \frac{1}{\epsilon}\left(2\ln\left(\frac{s_{4t} - m_t^2}{\mu m_t}\right) - \frac{5}{2}\right) + \frac{x_{sc}}{2} \right] d\sigma^B_{\text{dec}} + \mathcal{O}(1)\,, \quad (5.66)$$

we see an exact cancellation of the poles and the x_{sc} dependence, as required.

If we consider the pole structure of the various heavy-particle treatments,

$$\mathcal{M}^{\text{Virtual}}_{\text{prod}} = \left(\delta V^H_{[31]} + \delta V^H_{[2t]} + \frac{\delta V^H_{se+ct}}{2} \right) \mathcal{M}^{\text{tree}}_{\text{prod}} + \text{finite}\,, \quad (5.67)$$

$$\mathcal{M}^{\text{Virtual}}_{\text{dec}} = \left(\delta V^H_{[4t]} + \frac{\delta V^H_{se+ct}}{2} \right) \mathcal{M}^{\text{tree}}_{\text{dec}} + \text{finite}\,, \quad (5.68)$$

$$\mathcal{M}^{\text{Virtual}}_{\text{(i)NWA}} = \left(\delta V^H_{[31]} + \delta V^H_{[2t]} + \delta V^H_{[4t]} + 2\frac{\delta V^H_{se+ct}}{2} \right) \mathcal{M}^{\text{tree}}_{\text{(i)NWA}} + \text{finite}\,, \quad (5.69)$$

$$\mathcal{M}^{\text{Virtual}}_{\text{off}-\text{shell}} = \left(\delta V^H_{[31]} + \delta V^H_{[2t]} + \delta V^H_{[4t]} + \delta V^H_{se+ct} + \delta V^S \right) \mathcal{M}^{\text{tree}}_{\text{off}-\text{shell}} + \text{finite}\,, \quad (5.70)$$

where $\mathcal{M}^{\text{tree}}_{\text{NWA}} = \mathcal{M}^{\text{tree}}_{\text{prod}} \mathcal{M}^{\text{tree}}_{\text{dec}}$, 'finite' represents additional contributions which do not contain any poles or dependence on x_{sc}, and δV^S is the pole-containing factor of the soft contributions, it is easy to see how the pole structure of the various treatments develops. As we move from considering only the production process to the on-shell, NWA treatments, which include both production and decay, we gain additional singularities which come from the extra virtual and counterterm diagrams in the decay

process. The structure of these combined singularities exactly matches the structure of the hard singularities of the off-shell treatment. The only extra singularities which appear in the off-shell treatment arise from the soft contributions.

Here we have seen how the pole structure of the amplitudes develops as we move from considering the production of an on-shell top quark only to the inclusion of its decay and off-shell effects. The final step would be to perform the full calculation, without δ expansion. In this case, the poles of the virtual amplitudes would still factorise in the same way, into a tree-level amplitude multiplied by a pole-containing factor. The contributions would no longer be split into hard and soft components, however. Without the expansion in δ allowing us to neglect the contributions of certain diagrams, we would need to include all relevant diagrams. At tree level this would correspond to all diagrams shown in Figure 4.1. Each tree-level diagram would have a corresponding set of virtual diagrams. These virtual corrections would factorise in the same way as before, with the pole-containing factors multiplying the appropriate tree-level amplitude.

We have now considered all amplitudes necessary to calculate the cross section of t-channel single-top production to NLO using the various heavy-particle treatments outlined in Section 3.4. Some basic results, a comparison to existing results and a validation of our δ-counting are presented in the following section.

5.8 Comparison to Existing Results and Validation

In this section, a comparison of our total cross section values to some of those existing in the literature is presented and the validity of our δ-counting discussed.

$\mu_R = m_t/2$	$M_W = 80.4$ GeV
$\mu_F = m_t/2$	$\Gamma_W = 2.05141$ GeV
$\alpha_{ew} = 0.03402$	$\Gamma_t^{\text{LO}} = 1.46893$ GeV
$m_t = 172$ GeV	$\Gamma_t^{\text{NLO}} = 1.32464$ GeV

Table 5.1: Input parameters used for calculating the cross sections shown in Table 5.2.

	Ref. [48]	σ_{prod}	σ_{NWA}	$\sigma_{\text{off-shell}}$
LO [pb]	76.6	76.62(1)	76.62(1)	77.36(5)
NLO [pb]	84.4	84.41(1)	84.91(2)	86.3(3)

Table 5.2: Comparison of total cross sections, calculated using our various heavy-particle treatments, to those of Campbell et al. (2009) [48] at LO and NLO. Numbers in brackets represent Monte Carlo errors.

We begin by comparing our results, calculated using the various heavy-particle treatments, to those in Ref. [48], for the production of a stable, on-shell top-quark. For an LHC run with centre-of-mass energy, $\sqrt{s} = 10$ TeV, using the MSTW2008 PDF set [55], with the corresponding α_s value, and with other parameters shown in Table 5.1, we obtain the results presented in Table 5.2. We use the LO and NLO top-quark decay-widths for the calculation of the LO and NLO total cross sections respectively. This ensures agreement between the total cross sections when using the stable top-quark production and NWA treatments at LO, after integration over the fully-inclusive top-quark and W-boson decays, as it is equivalent to setting $\sigma_{\text{dec}}^0 = 2\Gamma_t^{\text{LO}} m_t$ and thus,

$$\sigma_{\text{NWA}}^0 = \frac{\sigma_{\text{prod}}^0 \sigma_{\text{dec}}^0}{2\Gamma_t^{\text{LO}} m_t} = \frac{2\sigma_{\text{prod}}^0 \Gamma_t^{\text{LO}} m_t}{2\Gamma_t^{\text{LO}} m_t} = \sigma_{\text{prod}}^0 . \tag{5.71}$$

Here, the superscript 0 denotes that the cross sections are at LO. It should be noted that, as there are no cuts made on the decay products of the W-boson, the total cross sections calculated using the NWA and iNWA treatments are identical. We obtain very good agreement with the results from Ref. [48] at LO, when using the stable top-quark

$\mu_R = m_t$	$M_W = 80.4$ GeV
$\mu_F = m_t$	$\Gamma_W = 2.06$ GeV
$\alpha_{ew} = 0.03394$	$\Gamma_t^{\text{LO}} = 1.6511$ GeV
$m_t = 178$ GeV	$\Gamma_t^{\text{NLO}} = 1.5077$ GeV

Table 5.3: Input parameters used for calculating the cross sections shown in Table 5.4.

production and NWA treatments, with our off-shell results having a slightly greater total cross section. At NLO, we still get agreement when using the stable production treatment, as we would expect, however, we now have a slight disagreement when using the NWA treatment. Our off-shell results are again slightly larger than those obtained using the other treatments. The discrepancy between the results obtained via the stable top-quark production and NWA treatments is due to the presence of the overall factor $1/(2\Gamma_t m_t)$ in the expression for total cross section when using the NWA treatment (Eq. (3.20)). Unlike the LO case, where there is a full cancellation of the decay-widths, as shown in Eq. (5.71), at NLO we do not get a complete cancellation and are instead left with a residual dependence on Γ_t;

$$\sigma_{\text{NWA}} = \frac{2m_t \left(\sigma_{\text{prod}}^0 \Gamma_t^{\text{NLO}} + \sigma_{\text{prod}}^1 \Gamma_t^{\text{LO}} \right)}{2\Gamma_t^{\text{NLO}} m_t} = \sigma_{\text{prod}} + \sigma_{\text{prod}}^1 \frac{\Gamma_t^{\text{LO}} - \Gamma_t^{\text{NLO}}}{\Gamma_t^{\text{NLO}}} , \qquad (5.72)$$

where $\sigma_{\text{NLO}} = \sigma^0 + \sigma^1$, with σ^0 and σ^1 the LO and NLO contributions to the full NLO cross section respectively. This residual dependence is a higher-order correction in our counting, however, as σ^1 is suppressed by a factor $\delta^{1/2}$ with respect to σ^0 and $(\Gamma_t^{\text{LO}} - \Gamma_t^{\text{NLO}})/\Gamma_t^{\text{NLO}} \sim \alpha_s \sim \delta^{1/2}$.

We now move on to our comparison with the results presented in Ref. [35], for the on-shell production of a single top-quark via the *t*-channel, followed by its decay. For an LHC run with centre-of-mass energy, $\sqrt{s} = 14$ TeV, using the MRST2002 NLO

	$\sigma^0_{\text{prod}}B_{t\to bl\nu}$	$\sigma_{\text{prod}}B_{t\to bl\nu}$	σ^0_{NWA}	σ_{NWA}	$\sigma^0_{\text{off}-\text{shell}}$	$\sigma_{\text{off}-\text{shell}}$
Ref. [35] [pb]	17.69(1)	17.05(2)	17.69(1)	16.98(2)	-	-
Our results [pb]	17.71(1)	17.04(1)	17.71(1)	16.98(1)	17.94(1)	17.33(8)

Table 5.4: Comparison of total cross sections, calculated using our various heavy-particle treatments, to those of Campbell et al. (2004) [35] at LO and NLO. Numbers in brackets represent Monte Carlo errors.

PDF set [52], with the corresponding α_s value, and with other parameters shown in Table 5.3, we obtain the results presented in Table 5.4. We again see good agreement, this time at both LO (denoted by the 0 superscript) and NLO, when using the stable top-quark production and NWA treatments. The stable top-quark production result is obtained by multiplying the production cross section by the LO branching ratio of the top quark into its decay products, $B_{t\to bl\nu} = 0.1104$. Once more, the inclusion of our off-shell effects increases the total cross section at both orders.

While it is clear that we are getting reasonable agreement with various existing total cross section values, it should be noted that we would not expect our off-shell results to be giving particularly good results in these cases. Our δ-counting requires that the top quark is close to resonance, that is $\Delta_t/m_t^2 \sim \delta$. In the above comparisons, however, no cuts were made on the decay products of the top quark, forcing it to be close to its mass shell, and thus our counting may not be valid. A more detailed discussion of this follows later in the section.

The above results are for the total, fully-inclusive cross sections. One of the main advantages of using the NWA and off-shell treatments of the top-quark, however, is the ability to apply cuts, allowing for better comparisons to experimental data. Applying cuts to the decay products of the top quark also highlights the differences between the NWA and iNWA treatments. We now look at a basic 'realistic' LHC setup with

$\sqrt{s} = 7$ TeV	$M_Z = 91.2$ GeV
$\mu_R = m_t/2$	$M_W = 80.4$ GeV
$\mu_F = m_t/2$	$\Gamma_W = 2.14$ GeV
$D_{\mathrm{res}} = 0.7$	$p_T(l^+) \geq 25$ GeV
$\not{E}_T \geq 25$ GeV	$p_T(J_b) \geq 20$ GeV
$m_t = 172$ GeV	$\Gamma_t^{\mathrm{NLO}} = 1.3281$ GeV
$\alpha_{ew} = 0.03394$	$120 \leq m_{\mathrm{inv}}(t) \leq 200$ GeV

Table 5.5: Input parameters used for calculating the cross sections shown in Table 5.6.

	σ_{NWA}	σ_{iNWA}	$\sigma_{\mathrm{off-shell}}$
LO [pb]	2.6782(7)	2.5498(8)	2.5185(8)
NLO [pb]	2.331(1)	2.257(2)	2.227(4)

Table 5.6: Comparison of LO and NLO cross sections for our basic 'realistic' LHC setup, calculated using three different heavy-particle treatments. Numbers in brackets represent Monte Carlo errors.

cuts applied to the outgoing particles and jets. In particular, we apply cuts on the transverse-momenta of the outgoing lepton, neutrino (in the form of the transverse missing-energy) and bottom-quark jet, and on the invariant-mass of the top quark, defined by

$$m_{\mathrm{inv}}(t) = \sqrt{(p(t))^2} = \sqrt{(p(J_b) + p(l^+) + p(\nu_l))^2} \,. \tag{5.73}$$

The bottom-quark jet, J_b, is defined using the algorithm outlined in Appendix B, with resolution parameter, D_{res}. We assume that we can always identify the jet originating from the bottom quark. The parameters and cuts used are shown in Table 5.5. We use MSTW2008 NLO PDFs and the NLO top-quark decay-width throughout. The results, at LO and NLO, for the NWA, iNWA and off-shell treatments of the top quark are shown in Table 5.6. As we now apply cuts to the decay products, the stable top-quark
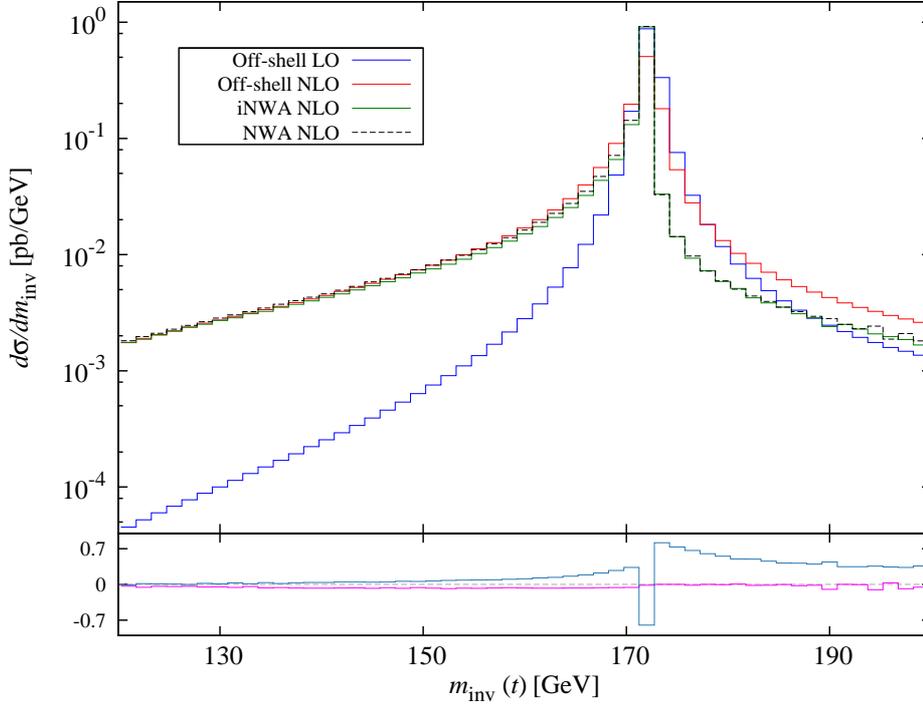
Figure 5.12: The top-quark invariant-mass distribution at LO (blue) and NLO (red) in the
off-shell treatment and NLO in the NWA (dashed black) and iNWA (green)
treatments. The lower panel shows the ratio of the off-shell effects (azure) and
spin-correlation effects (magenta) to the full off-shell NLO result.

production treatment can no longer be used, due to the branching ratio requiring fully-
inclusive decays. The first point to note is that, with the inclusion of cuts, the cross
sections obtained using the off-shell treatment are now smaller than those obtained
using the NWA treatments, whereas without cuts the cross sections were larger. The
size of the off-shell effects remains approximately the same at $\sim$ 1-2% of the full NLO
result. The more pronounced effect comes as we move from the NWA to the iNWA,
including spin-correlation effects. Here, the effect is $\sim$ 3-5% of the full NLO result.
While the cross sections are useful for comparisons to existing work, we are more
interested in kinematic distributions.

The distribution of the top-quark invariant-mass, defined in Eq. (5.73), is shown in
Figure 5.12. The plot shows the NLO results for the NWA, iNWA and off-shell top-

quark treatments, along with the LO off-shell result. The NWA results at LO would comprise a large delta-function peak at $m_{\text{inv}}(t) = m_t$, plus a very small contribution for $m_{\text{inv}}(t) > m_t$ and are not shown. In this particular distribution, there is little difference between the two NWA treatments and, therefore, in the following discussion they are referred to collectively. The most notable change comes at LO, where we move from a sharp peak at $m_{\text{inv}}(t) = m_t$ (not shown in the figure) to the more spread out Breit-Wigner shape (shown in blue) as we include the off-shell effects. At NLO, while the effects are not as pronounced as at LO, there are still substantial changes to the shape of the distribution. For $m_{\text{inv}}(t) < m_t$, the shape of the distributions in the off-shell and NWA treatments are very similar, with substantial increases in the differential cross section over the LO off-shell result. Around the m_t peak, and for $m_{\text{inv}}(t) > m_t$, however, the two treatments show different effects. In the NWA treatments, the peak at m_t is much sharper than in the off-shell treatment. As the invariant-mass increases, the differential cross section of the NWA treatments remains smaller than that of the off-shell treatment. Although the overall difference in the total cross section is only small, the effects seen in the distribution are more substantial. The lower panel of Figure 5.12 shows the ratio of the off-shell effects, defined as the difference between the off-shell and iNWA results at NLO, and the spin-correlation effects, defined as the difference between the iNWA and NWA results at NLO,

$$\sigma_{\text{os}} = \sigma_{\text{off-shell}} - \sigma_{\text{iNWA}} \,, \qquad \sigma_{\text{sc}} = \sigma_{\text{iNWA}} - \sigma_{\text{NWA}} \qquad (5.74)$$

to the full off-shell result at NLO, $\sigma_{\text{off-shell}}$. This illustrates more clearly how the inclusion of off-shell effects, despite changing the overall cross section by only a few percent, can have a large effect in certain kinematic regions of distributions. For $m_{\text{inv}}(t) \leq 165$ GeV, the NWA and off-shell treatments give almost identical results. At invariant-mass values greater than this, however, the off-shell effects are much greater

than the few percent seen in the cross section. In fact, very close to the peak, these off-shell effects can be as large as $\sim 70\%$ in some bins. The spin-correlation effects are small across the whole distribution. Considering the shape of the invariant-mass distribution can also help to explain why the inclusion of off-shell effects causes an increase in the cross section when no cuts are applied, but a decrease when we include cuts. As mentioned earlier, the NWA treatments have a sharper peak than the off-shell treatment, but the off-shell treatment is larger for $m_{\text{inv}}(t) > m_t$ at NLO. These competing effects can act to make the off-shell corrections either positive or negative. For a loose invariant-mass cut, or no cut at all, the increased contribution of the off-shell treatment in the region $m_{\text{inv}}(t) > m_t$ outweighs the larger peak of the NWA treatments, resulting in a positive correction overall. However, if we apply a tighter cut on $m_{\text{inv}}(t)$, we lose some of the increased off-shell contribution from the region $m_{\text{inv}}(t) > m_t$ and, if the cut is tight enough, the larger peak of the NWA dominates, leading to the off-shell contribution being negative overall. The size of the invariant-mass cut is important for more than just the cross section results, however. It is also vital for our δ-counting to behave as expected. This is discussed later in the section.

As an illustration of our δ-counting, it is useful to consider the subleading contributions to the tree-level squared matrix-element. As shown in Eq. (4.10), the first subleading terms, suppressed by a factor $\sim \delta$ with respect to our leading diagram, are the QCD-mediated diagrams, $\mathcal{M}_{\text{QCD}} \sim g_{ew}^2 g_s^4 \left| A_{(0)}^{(1,2)} \right|^2$, and the diagrams comprising the interference between the resonant EW-diagram and the other EW-mediated diagrams, $\mathcal{M}_{\text{int}} \sim g_{ew}^6 \, 2\,\text{Re}\left[A_{(0)}^{(3,0)} \left(A_{(-1)}^{(3,0)} \right)^* \right]$. Beyond this, we have the square of the EW-mediated diagrams, $\mathcal{M}_{\text{EW}} \sim g_{ew}^6 |A_{(0)}^{(3,0)}|^2$, which is suppressed by a factor $\sim \delta^2$ with respect to the leading diagram. The squared matrix-elements of these diagrams are relatively easy to calculate and can offer us an insight into the validity of our δ-counting. Using the parameters in Table 5.5, we obtain the cross sections shown in

$\sigma^0_{\text{off-shell}}$	$\sigma^1_{\text{off-shell}}$	σ_{QCD}	σ_{int}	σ_{EW}
2.5185(8)	$-0.291(3)$	0.3908(3)	$-0.00415(3)$	0.00724(1)

Table 5.7: Comparison of leading and subleading contributions to the cross section for our basic 'realistic' LHC setup. Numbers in brackets represent Monte Carlo errors. All values are in picobarns.

Table 5.7. Here, $\sigma_{\text{off-shell}} = \sigma^0_{\text{off-shell}} + \sigma^1_{\text{off-shell}}$, with $\sigma^0_{\text{off-shell}}$ and $\sigma^1_{\text{off-shell}}$ the LO ($\sim \delta$) and NLO ($\sim \delta^{3/2}$) contributions to the full off-shell NLO cross section respectively. We can see that our counting has produced the expected results in some cases. Our NLO contribution, $\sigma^1_{\text{off-shell}}$, is suppressed by a factor $\sim \delta^{1/2}$ with respect to our LO contribution, $\sigma^0_{\text{off-shell}}$, and the electroweak-interference terms, σ_{int}, are suppressed by a factor $\sim \delta$. However, the QCD and EW terms do not show the expected suppression. This can be explained if we consider the cut applied to the invariant-mass of the top quark. We restrict this to the range $120 \leq m_{\text{inv}}(t) \leq 200$ GeV. This can give us a Δ_t/m_t^2 value anywhere in the range $\sim 0.01 - 0.5$, when we use $p_t^2 \approx m_{\text{inv}}(t)^2$. In our counting we assume that $\Delta_t/m_t^2 \sim \delta$. Clearly, within our invariant-mass cut, there is a region where this is satisfied. There are also regions where the propagator scales more like $\Delta_t/m_t^2 \sim \delta^{1/2}$, however. In these regions, our counting no longer applies in the same way. Instead, the leading part of the resonant diagram would scale as $\sim \delta$, rather than $\sim \delta^{1/2}$. In this case, the QCD diagrams would be of the same order as the resonant diagram, while the EW diagrams would be suppressed only by a factor $\sim \delta^{1/2}$. This effect can be seen in Figure 5.13, where we show the contributions of the various diagrams to the top-quark invariant-mass distribution. Here, it is clear to see that the QCD contribution, for example, is no longer suppressed with respect to the off-shell NLO contribution for invariant-mass values too far away from m_t. In fact, in the ranges $m_{\text{inv}}(t) < 145$ GeV and $m_{\text{inv}}(t) > 185$ GeV, the QCD contribution is actually greater than that of the off-shell NLO diagrams. The lower panel of Figure 5.13
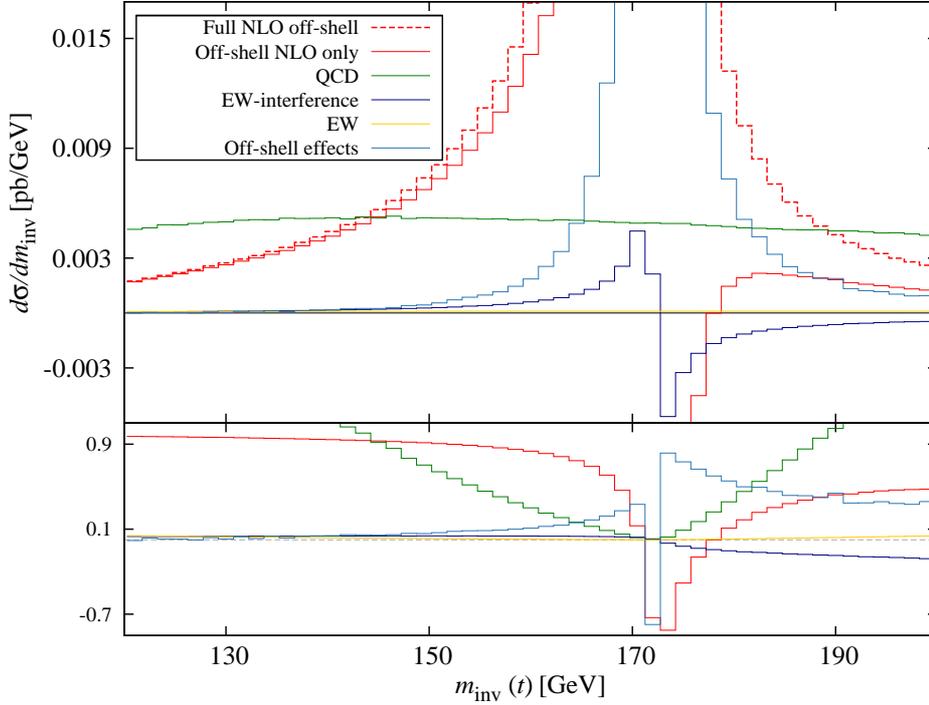
Figure 5.13: The contributions of $\sigma^1_{\text{off}-\text{shell}}$ (red), σ_{QCD} (green), σ_{int} (dark blue), σ_{EW} (yellow) and the off-shell effects, σ_{os} (azure), to the top-quark invariant-mass distribution. The lower panel shows the ratio of each contribution to the full off-shell NLO result, $\sigma_{\text{off}-\text{shell}}$ (shown as the dashed red line in the upper panel).

shows the ratio of the various contributions to the full NLO cross section in the off-shell treatment. While it is clear that, in the region close to m_t, the NLO contribution and off-shell effects dominate, as we move further away, other contributions, in particular the QCD contribution, become increasingly important. It is the contributions from these regions which lead to the QCD and EW cross sections being less suppressed than expected.

Clearly, the size of the invariant-mass cut has an important effect on our δ-counting. Figure 5.14 shows the δ-suppression (with δ defined via the couplings rather than the resonant propagator) of the various contributions, with respect to the LO resonant diagram, as a function of the top-quark invariant-mass window, Δ_{m_t}, used. We use the
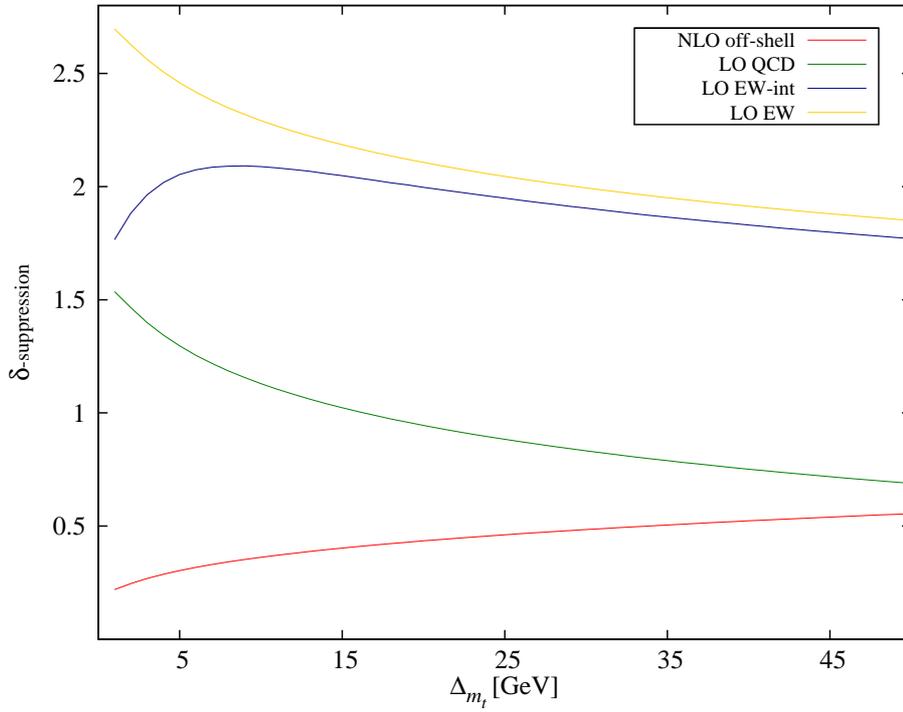
Figure 5.14: The δ-suppression of $\sigma^1_{\mathrm{off-shell}}$ (red), σ_{QCD} (green), σ_{int} (dark blue) and σ_{EW} (yellow), with respect to $\sigma^0_{\mathrm{off-shell}}$, as a function of the width of the top-quark invariant-mass cut, Δ_{m_t}. The y-axis gives the power of δ by which the contribution is suppressed with respect to LO.

parameters and cuts shown in Table 5.5, but with the top-quark invariant-mass cut modified to $(m_t - \Delta_{m_t}/2) \leq m_{\text{inv}}(t) \leq (m_t + \Delta_{m_t}/2)$. The y-axis of the figure shows the power of δ by which the contribution is suppressed with respect to the LO diagram. For example, a value of 2 on the y-axis indicates that the contribution is suppressed by a factor $\sim \delta^2$ compared to LO. With an invariant-mass window of $\Delta_{m_t} \sim 20$ GeV, we observe the expected behaviour in most of the cases. The off-shell NLO contributions show a suppression of $\sim \delta^{1/2}$, the QCD contributions a suppression $\sim \delta$, and the EW contributions a suppression $\sim \delta^2$. The EW-interference contribution shows greater suppression than expected. This is a total cross section effect, however. Looking at the EW-interference contribution in Figure 5.13 (dark blue), we see that around the m_t peak, the size of the corrections is of a similar order to the QCD corrections (green), as expected in our counting. However, due to the sign change that occurs in the correction, its total effect on the cross section suffers some cancellation and is smaller than expected. As the invariant-mass window increases, the difference between the δ-suppression of the QCD corrections and the off-shell NLO corrections becomes smaller and smaller, indicating that our power counting is breaking down. The EW-interference and EW contributions are still sufficiently suppressed that they can be ignored to the order at which we are working.

Although we have seen that using a wide invariant-mass cut leads to a slight breakdown of our δ-counting, we will continue to use this for the rest of our results. While using a tighter cut would lead to improved behaviour of the δ-counting, it would also lead to a loss of cross section and is generally not used in experiment. We therefore take this cut with the expectation that some of our subleading corrections may be larger than expected.

Chapter 6

Results

In this chapter, results obtained using the method outlined in Chapters 4 and 5 are given for runs at both the Tevatron and the 7 TeV LHC. A brief comparison to some existing results is also performed.

6.1 Defining Processes

As mentioned in Section 1.2, a single top-quark can be produced via the s-channel, the t-channel or with an associated W-boson, see Figure 1.2. The associated-tW production channel can be easily distinguished from s- and t-channel production due to the presence of an extra W-boson (lepton plus transverse missing-energy) in the final state. As the total cross section of this production channel is also suppressed with respect to the t-channel cross section, as seen in Table 1.2, it will not be discussed further. We will instead focus on the other two production channels. It should be noted, however, that the methods presented in this thesis could easily be applied to the associated-tW production channel.

The s- and t-channel production mechanisms, while distinguishable at tree level, are entangled at NLO. For t-channel production we have

$$q(p_1)\, b(p_2) \rightarrow q'(p_3)\, b(p_4)\, l^+(p_5)\, \nu_l(p_6)\,, \tag{6.1}$$

for the tree-level and one-loop processes, and

$$q(p_1)\, b(p_2) \rightarrow q'(p_3)\, b(p_4)\, l^+(p_5)\, \nu_l(p_6)\, g(p_7)\,, \tag{6.2}$$

$$g(p_1)\, b(p_2) \rightarrow q'(p_3)\, b(p_4)\, l^+(p_5)\, \nu_l(p_6)\, \bar{q}(p_7)\,, \tag{6.3}$$

$$q(p_1)\, g(p_2) \rightarrow q'(p_3)\, b(p_4)\, l^+(p_5)\, \nu_l(p_6)\, \bar{b}(p_7)\,, \tag{6.4}$$

for the real processes. Similarly, for the s-channel we have

$$Q(p_1)\, \bar{Q}'(p_2) \rightarrow \bar{b}(p_3)\, b(p_4)\, l^+(p_5)\, \nu_l(p_6)\,, \tag{6.5}$$

for the tree-level and one-loop processes, and

$$Q(p_1)\, \bar{Q}'(p_2) \rightarrow \bar{b}(p_3)\, b(p_4)\, l^+(p_5)\, \nu_l(p_6)\, g(p_7)\,, \tag{6.6}$$

$$Q(p_1)\, g(p_2) \rightarrow \bar{b}(p_3)\, b(p_4)\, l^+(p_5)\, \nu_l(p_6)\, Q'(p_7)\,, \tag{6.7}$$

for the real processes. Here, q is a light quark (u, c) or anti-quark $(\bar{d}, \bar{s})$ and, accordingly, q' is a quark (d, s) or anti-quark $(\bar{u}, \bar{c})$ respectively. Q represents a light quark (u, c), with $\bar{Q}'$ the respective anti-quark of its generational partner $(\bar{d}, \bar{s})$. Clearly, Eq. (6.4) and Eq. (6.7) have the same particles in the final state, despite one belonging to t-channel production and the other to s-channel production. Therefore, rather than defining channels according to their production mechanism, we instead define them
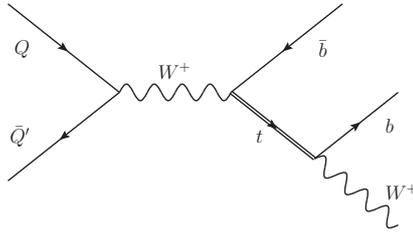
Figure 6.1: The only tree-level Feynman diagram contributing to the LO cross section of the hard-scattering process in Eq. (6.5) to $\mathcal{O}(\delta)$.

according to their final states. Let us define two hadronic processes;

$$h_1 \, h_2 \to J_b \, J_l \, l^+ \, \not{E}_T \, + \, X \,, \tag{6.8}$$

$$h_1 \, h_2 \to J_b \, J_{\bar{b}} \, l^+ \, \not{E}_T \, + \, X \,, \tag{6.9}$$

where h_1 and h_2 are incoming hadrons, with $h_1 h_2 = p\bar{p}$ for the Tevatron and $h_1 h_2 = pp$ for the LHC, J_b ($J_{\bar{b}}$) is a jet originating from a bottom (anti-)quark, J_l is a jet originating from a light parton and $\not{E}_T$ represents transverse missing-energy. The parameter, X, denotes any additional jets which do not originate from a bottom quark or anti-quark. At tree level, it is clear to see that Eq. (6.8) corresponds to t-channel production and Eq. (6.9) corresponds to s-channel production. The real t-channel processes in Eqs. (6.2) and (6.3) are included in the process defined in Eq. (6.8), henceforth referred to as the single b-jet process. The remaining processes are ambiguous, however. Assuming that the $\bar{b}$-jet has sufficient transverse momentum to be detected, all the remaining processes (Eqs. (6.4), (6.6) and (6.7)) are included in Eq. (6.9), henceforth referred to as the double b-jet process. However, if the $\bar{b}$-jet is very forward, and remains undetected, the final state of these processes could correspond to that of the single b-jet process. In this case, they must be included in that cross section.

All the amplitudes necessary to calculate the cross sections of the single b-jet and double b-jet processes to $\mathcal{O}(\delta^{3/2})$ can be obtained from those appearing in Chapter 5
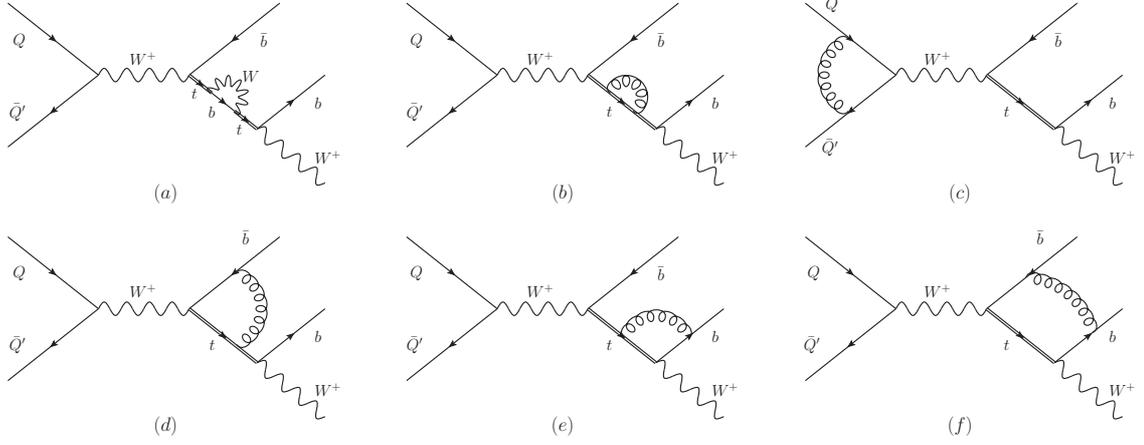
Figure 6.2: The one-loop Feynman diagrams required to calculate the NLO cross section of the hard-scattering process in Eq. (6.5) to $\mathcal{O}(\delta^{3/2})$.
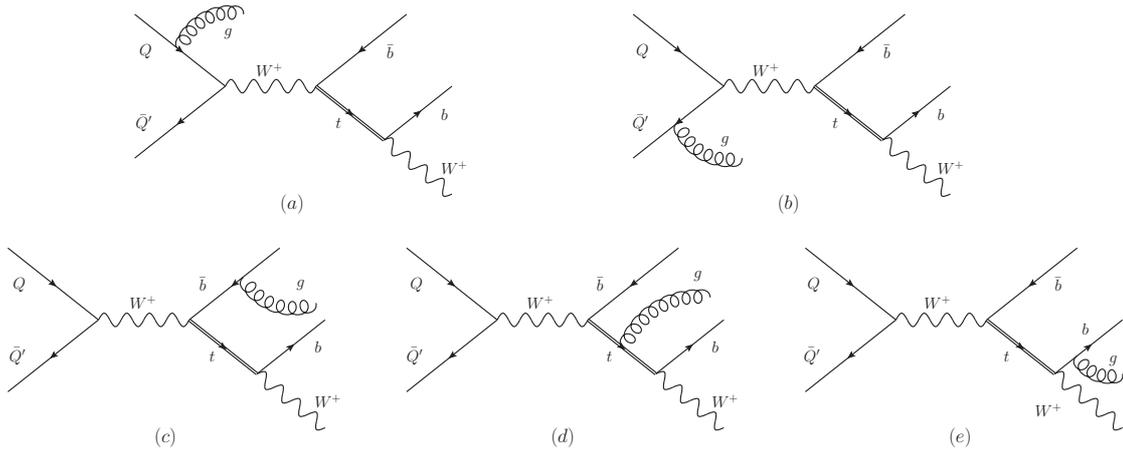
Figure 6.3: The real gluon-emission Feynman diagrams, representing the process in Eq. (6.6), required to calculate the NLO cross section of the hard-scattering process in Eq. (6.5) to $\mathcal{O}(\delta^{3/2})$.
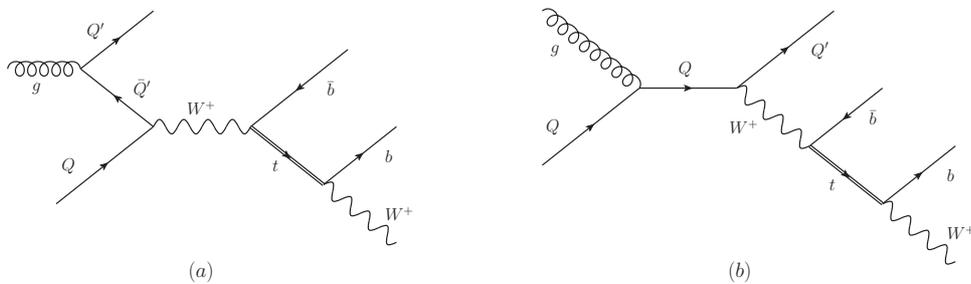
Figure 6.4: The real gluon-initiated Feynman diagrams, representing the process in Eq. (6.7), required to calculate the NLO cross section of the hard-scattering process in Eq. (6.5) to $\mathcal{O}(\delta^{3/2})$.

$M_Z = 91.2$ GeV	$\mu_R = \mu_F = m_t/2$
$M_W = 80.4$ GeV	$\alpha_{ew} = 0.03394$
$m_t = 172$ GeV	$\Gamma_W = 2.14$ GeV
$D_{\text{res}} = 0.7$	$\Gamma_t^{\text{NLO}} = 1.3281$ GeV

Table 6.1: Input parameters used for calculating the cross sections and distributions shown throughout Chapter 6.

and Appendix C. The diagrams required for the processes in Eqs. (6.1)-(6.4) are shown in Figures 4.1a, 4.2, 4.3 and 4.4, while those for the processes in Eqs. (6.5)-(6.7) are shown in Figures 6.1 - 6.4.

To obtain the s-channel amplitudes from the t-channel amplitudes, appearing in Appendix C, we use momentum crossing. Here we show, as an example, how the s-channel tree-level amplitude is obtained from that of the t-channel. By comparing the tree-level diagrams in Figures 4.1a and 6.1, we can see that the two are closely related. If we swap the outgoing $\bar{b}$-quark for an incoming b-quark and the incoming $\bar{Q}'$-quark for an outgoing Q'-quark in the s-channel diagram, we obtain the t-channel diagram. This is equivalent to exchanging the momenta $p_2 \leftrightarrow -p_3$ in the amplitude. We obtain the s-channel tree-level amplitude by exchanging these momenta in the t-channel tree-level amplitude, Eq. (5.2). This gives

$$A_{(-1)}^{(3,0)} = g_{ew} \sqrt{\frac{1}{2M_W \Gamma_W}} \frac{[13]\langle 46 \rangle \langle 2|4+6|5]}{(-s_{12} + M_W^2) \Delta_t} . \tag{6.10}$$

Using the same method as outlined above, we can calculate the amplitudes of all the required s-channel diagrams from their t-channel counterparts.

The parameters used to obtain the results presented in this chapter are given in Table 6.1. We use the NLO top-quark decay-width and the NLO MSTW2008 PDFs

$p\bar{p} \to J_b J_l \, l^+ \, \not{E}_T + X$	$p\bar{p} \to J_b J_{\bar{b}} \, l^+ \, \not{E}_T + X$
$p_T(J_b) \geq 20$ GeV	$p_T(J_b) \geq 20$ GeV
$p_T(J_l^H) \geq 20$ GeV	$p_T(J_{\bar{b}}) \geq 20$ GeV
$p_T(J_{\bar{b}}) < 20$ GeV	$p_T(J_l) < 15$ GeV
$\left(\not{E}_T + p_T(l^+)\right) \geq 30$ GeV	$\left(\not{E}_T + p_T(l^+)\right) \geq 30$ GeV
$120 \leq m_{\mathrm{inv}}(t) \leq 200$ GeV	$120 \leq m_{\mathrm{inv}}(t) \leq 200$ GeV

Table 6.2: Kinematical cuts applied to the two considered processes at the Tevatron.

[55], with the corresponding strong coupling, α_s, throughout. Jets are constructed according to the algorithm in Appendix B.

6.2 Tevatron Results

The first set of results we present are for the Fermilab Tevatron with a centre-of-mass energy, $\sqrt{s} = 1.96$ TeV. The kinematical cuts applied to our two processes of interest; the single b-jet process, given in Eq. (6.8), and the double b-jet process, given in Eq. (6.9), are shown in Table 6.2. For both processes, we apply a loose cut on the invariant-mass of the top quark, defined in Eq. (5.73), to ensure that our δ-counting roughly holds but we don't lose too much cross section (see Section 5.8 for a more detailed discussion of this). We also apply transverse-momentum cuts on all final-state jets and particles that we hope to observe (J_b, J_l^H, l^+, $\not{E}_T$ for the single b-jet process, and J_b, $J_{\bar{b}}$, l^+, $\not{E}_T$ for the double b-jet process), in order that they are seen in the detectors rather than being lost down the beam pipe. It should be noted that, in the single b-jet process, the cut on the light jet, J_l, is applied to the hardest light-jet present in the final state, as it is possible that more than one light-parton jet may exist. The hardest light-jet is denoted J_l^H. Along with these cuts, we also apply a jet veto in each

		σ_{NWA}	σ_{iNWA}	$\sigma_{\mathrm{off-shell}}$
$p\bar{p} \to J_b J_l \, l^+ \not{E}_T + X$	LO [fb]	87.12(1)	88.11(1)	$86.89(1)^{+0.45}_{-4.01}$
	NLO [fb]	53.84(1)	54.43(5)	$53.62(5)^{+7.76}_{-15.24}$
$p\bar{p} \to J_b J_{\bar{b}} \, l^+ \not{E}_T + X$	LO [fb]	34.85(1)	35.16(1)	$34.68(1)^{+3.53}_{-2.97}$
	NLO [fb]	27.54(1)	27.79(1)	$27.42(2)^{+1.95}_{-1.00}$

Table 6.3: The LO and NLO cross sections for $p\bar{p} \to J_b J_l \, l^+ \not{E}_T + X$ and $p\bar{p} \to J_b J_{\bar{b}} \, l^+ \not{E}_T + X$ at the Tevatron, calculated using the NWA, iNWA and off-shell top-quark treatments. Numbers in brackets represent Monte Carlo errors. The subscript and superscript values on the off-shell results are errors arising from scale uncertainty only.

case, to suppress contributions coming from the 'wrong' process. For the single b-jet process, we apply a veto on a $\bar{b}$-jet to suppress contributions from s-channel diagrams. This veto also suppresses the contribution of the t-channel process given in Eq. (6.4), however. For the double b-jet process, we veto a light jet to suppress contributions from t-channel diagrams, although this veto also suppresses the contributions of the NLO s-channel processes given in Eqs. (6.6) and (6.7). The contributions from the 'wrong' processes cannot be fully removed, however. Configurations in which the jets travel down the beam pipe and remain undetected must still be included.

The cross sections of the two processes are given, at LO and NLO in our counting, in Table 6.3. Results calculated using both the NWA and iNWA treatments of the top quark are also given for comparison. The total NLO corrections to the two processes are very large, amounting to $\sim 40\%$ and $\sim 20\%$ of the LO value for the single b-jet and double b-jet configurations respectively. The differences between the three heavy-particle treatments are small, with the off-shell effects typically being approximately 1-2% of the full NLO result. This is in agreement with the naïve expectation that the NWA has accuracy of the order $\Gamma_t/m_t \sim 1\%$.
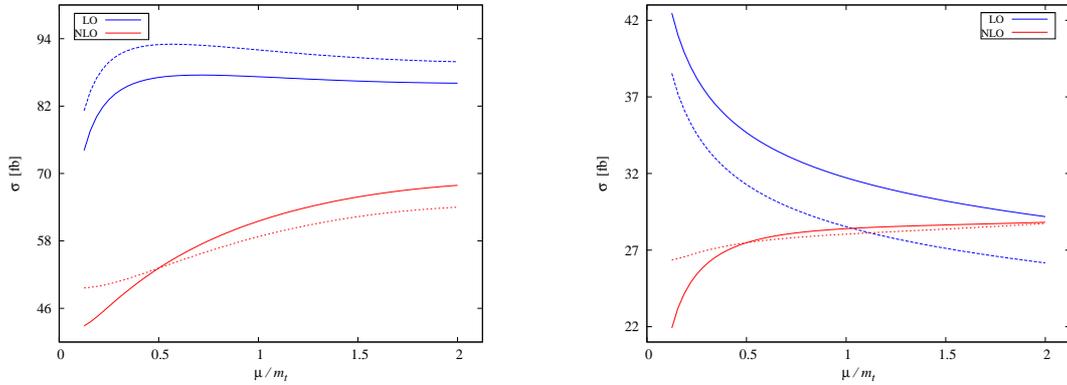
Figure 6.5: Scale dependence for $p\bar{p} \to J_b J_l\, l^+ \not{E}_T + X$ (left plot) and $p\bar{p} \to J_b J_{\bar{b}}\, l^+ \not{E}_T + X$ (right plot) at the Tevatron. The plot shows the scale dependence of the LO cross section using LO PDFs (dashed blue) and NLO PDFs (solid blue), and the scale dependence of the NLO cross section using NLO PDFs while varying the factorisation scale only, leaving the renormalisation scale fixed (dotted red), and while varying both scales simultaneously (solid red).

The errors (given as subscripts and superscripts) on the off-shell cross sections in Table 6.3 were obtained by varying the renormalisation and factorisation scales in the range $[m_t/4, m_t]$. We see a slight reduction in scale dependence as we move from LO to NLO in the double b-jet case, as expected. However, in the single b-jet case there is a substantial increase in the scale dependence. One possible explanation for this unexpected increase is that at NLO we have a dependence on both the renormalisation scale and the factorisation scale, whereas at LO there is no renormalisation-scale dependence, as the amplitude contains no strong coupling constants. The effects of the dependence on this additional scale can be seen more clearly in Figure 6.5. The red dotted line shows the scale dependence at NLO with the renormalisation scale fixed at the central scale and only the factorisation scale varied. The solid red line has both scales varied simultaneously, with $\mu_R = \mu_F$. When only the factorisation scale is varied, the resulting dependence is much flatter than that obtained when both scales are varied, thus leading to a smaller scale dependence. For the single b-jet process, the NLO scale-dependence is reduced to approximately the same level as the LO depen-

	Partonic process	$p\bar{p} \to J_b J_l\, l^+ \not{E}_T + X$	$p\bar{p} \to J_b J_{\bar{b}}\, l^+ \not{E}_T + X$
LO [fb]	$qb \to q'bl^+\nu_l$	86.89(1)	-
	$Q\bar{Q}' \to \bar{b}bl^+\nu_l$	-	34.68(1)
NLO [fb]	$qb \to q'bl^+\nu_l(g)$	$-4.7(1)$	-
	$gb \to q'bl^+\nu_l\bar{q}$	$-0.886(1)$	-
	$qg \to q'bl^+\nu_l\bar{b}$	$-29.67(6)$	3.524(2)
	$Q\bar{Q}' \to \bar{b}bl^+\nu_l(g)$	1.948(2)	$-9.84(3)$
	$Qg \to \bar{b}bl^+\nu_l Q'$	0.121(1)	$-1.002(1)$

Table 6.4: The contributions of the various partonic processes to the LO and NLO cross sections for $p\bar{p} \to J_b J_l\, l^+ \not{E}_T + X$ and $p\bar{p} \to J_b J_{\bar{b}}\, l^+ \not{E}_T + X$ at the Tevatron. Cross sections were calculated using the off-shell top-quark treatment. Numbers in brackets represent Monte Carlo errors.

dence, while for the double b-jet process, the NLO scale-dependence is reduced even further compared to that at LO. The effect is not due to the fact that we use NLO PDFs for the LO cross section. This causes a shift in the cross sections but does not have a large effect the overall shape of the scale dependence. This is also shown in Figure 6.5, where the blue dashed line shows the LO cross section with LO PDFs and the solid blue line the LO cross section with NLO PDFs. Finally, the scale uncertainty is dependent on our choice of central scale. In the figure, it can clearly be seen that the scale dependence is more pronounced at smaller values of μ with a gradual flattening as we go to larger values. Therefore, if we had taken our central scale as m_t, for example, rather than $m_t/2$, we would have obtained a smaller scale dependence.

As we redefined our processes in terms of final-state particles as opposed to the production method, it is interesting to see the size of the various contributions to the overall NLO cross section. A split of the cross sections, calculated using the off-shell heavy-particle treatment, is shown in Table 6.4. The partonic processes contributing are those given in Eqs. (6.1)-(6.7). The processes $qb \to q'bl^+\nu_l(g)$ and $Q\bar{Q}' \to \bar{b}bl^+\nu_l(g)$

in the table represent the sum of the one-loop corrections to the tree-level process and the real corrections defined by the tree-level process with an extra emitted gluon. For the single b-jet process, the majority of the full NLO cross section ($\sim 96\%$) comes from the t-channel diagrams, with the s-channel diagrams comprising the remaining amount. For the double b-jet process, however, the s-channel diagrams contribute $\sim 87\%$ of the full NLO cross section, while the t-channel diagrams make up the remaining $\sim 13\%$. Despite applying cuts specifically designed to suppress t-channel contributions to the s-channel cross section, their presence still has a sizeable effect. The results in the table also show, for the cuts and parameters we are using, the importance of the $qg \rightarrow q'bl^+\nu_l\bar{b}$ partonic process to both channels. For the single b-jet process, its contribution makes up $\sim 89\%$ of the total NLO correction, while for the double b-jet process its contribution makes up $\sim 33\%$ of the NLO correction. Its large, negative effect on the single b-jet cross section is likely to be a result of the veto on the $\bar{b}$-jet.

We will now move on to consider kinematic distributions for the two processes. Firstly, we will discuss the top-quark invariant-mass distributions, which are shown in Figure 6.6. The two plots show the LO and NLO results, calculated using the off-shell treatment of the top quark, as blue and red bands respectively. The bands were obtained by simultaneously varying the renormalisation and factorisation scales by a factor of 2 about the central value, $m_t/2$. That is, $m_t/4 \leq (\mu_R = \mu_F) \leq m_t$. The results obtained using the central value appear as solid lines within the wider band. The NLO result obtained using the iNWA treatment is also shown, for the central value of the scale, as a green line. The lower panel of the plots shows the ratio of the off-shell and spin-correlation effects, defined in Eq. (5.74), to the full off-shell NLO result, $\sigma_{\text{off}-\text{shell}}$. We observe similar effects to those discussed in Section 5.8 in both cases. The peak at $m_{\text{inv}}(t) = m_t$ decreases and becomes broader as we move from the iNWA treatment to the off-shell treatment. Above and below the peak we observe
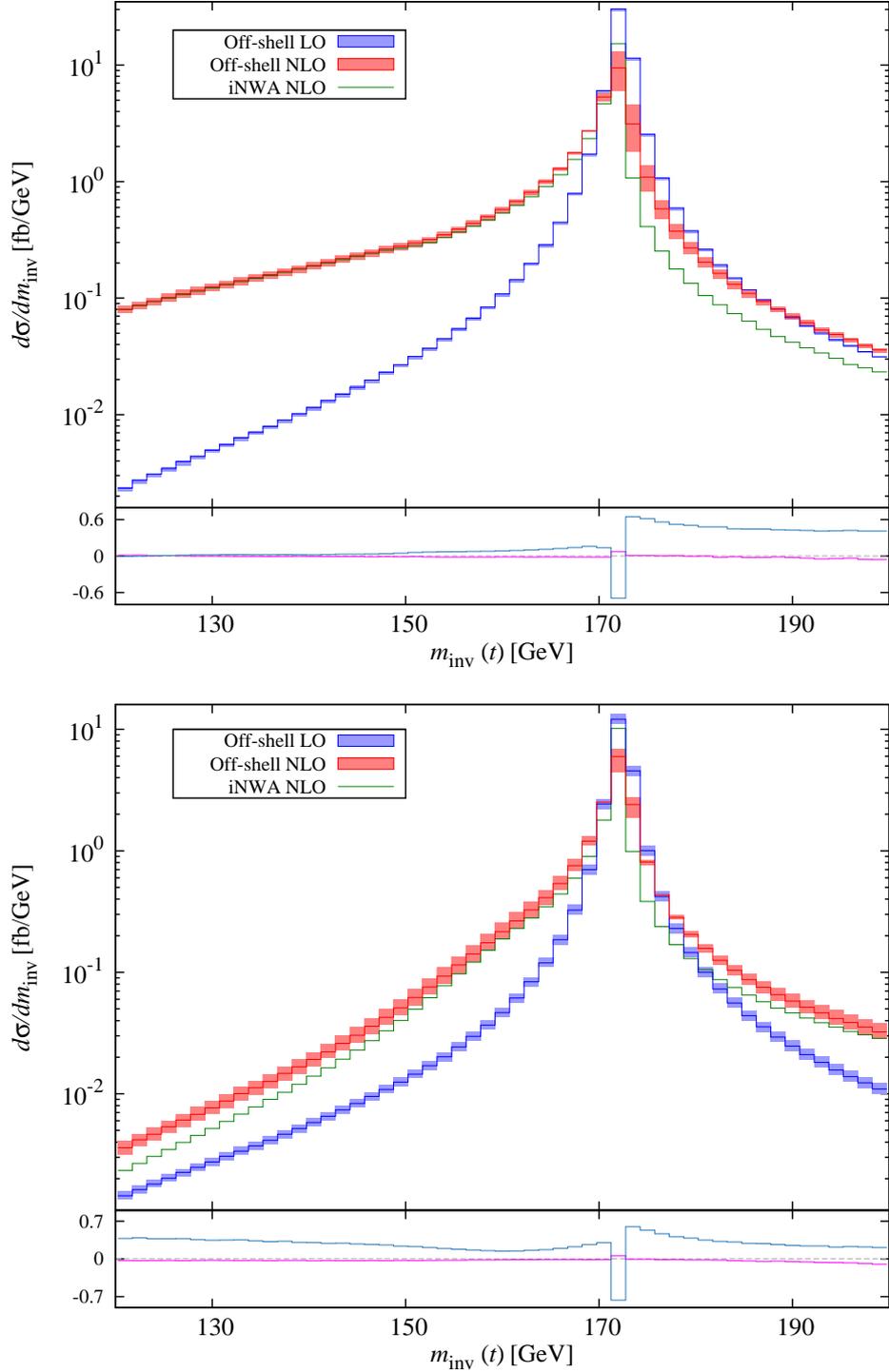
Figure 6.6: The top-quark invariant-mass distribution at LO (blue band) and NLO (red band) in the off-shell treatment and NLO in the iNWA treatment (green) for $p\bar{p} \rightarrow J_b J_l \, l^+ \, \not{E}_T + X$ (upper plot) and $p\bar{p} \rightarrow J_b J_{\bar{b}} \, l^+ \, \not{E}_T + X$ (lower plot) at the Tevatron. The lower panel of the plots shows the ratio of the off-shell effects (azure) and spin-correlation effects (magenta) to the full off-shell NLO result.

slightly different behaviour for the single b-jet and double b-jet processes. The former shows little difference between the iNWA and off-shell treatments for $m_{\mathrm{inv}}(t) < m_t$, with both having substantially larger differential cross sections than the LO off-shell treatment. For $m_{\mathrm{inv}}(t) > m_t$, we see that the NLO results lie below the LO results, with the difference between the two becoming smaller as $m_{\mathrm{inv}}(t)$ increases. In fact, the off-shell NLO result becomes larger than the LO result at $m_{\mathrm{inv}}(t) \sim 190$ GeV. The iNWA result is smaller than the off-shell result throughout this region. For the double b-jet process, in the region $m_{\mathrm{inv}}(t) < m_t$ we see an increasing difference between the NLO iNWA and off-shell results as $m_{\mathrm{inv}}(t)$ decreases. Both results lie much closer to the LO value than in the single b-jet case. For $m_{\mathrm{inv}}(t) > m_t$, the NLO results quickly become larger then the LO result and the difference between the iNWA and off-shell results decreases as $m_{\mathrm{inv}}(t)$ increases. In both cases, the NWA and iNWA results are almost identical, leading to the spin-correlation effects being very close to zero across the whole invariant-mass range. The differences in the NLO results can be seen more clearly in the lower panels of the plots. Around the peak, both display similar off-shell behaviour, with large effects and a flip from being a positive correction to a negative one. In the single b-jet case we see the off-shell effects tending towards zero as the invariant-mass decreases, while they settle to a value of $\sim 40\%$ of the full NLO result as the invariant-mass increases. For the double b-jet process, the off-shell effects gradually decrease as the invariant-mass increases, appearing to settle at a constant value of $\sim 30\%$ of the full NLO result, while they gradually increase as the invariant-mass decreases. Including off-shell effects increases the differential cross section in every bin except the one containing the peak, where the contribution is large and negative. It is the cancellation of these positive and negative effects that leads to the overall contribution of the off-shell effects appearing to be small in any observables which are very inclusive with respect to the top-quark invariant-mass, for example, the

total cross section. While we see effects as large as $\sim \pm 60\%$ in some individual bins of the invariant-mass distributions, the overall effect on the cross section is $\sim$ 1-2%. It is possible, however, that the application of certain kinematic cuts could spoil this cancellation, leading to more substantial off-shell effects in some distributions.

A selection of other kinematic distributions for the single b-jet process are presented in Figure 6.7. These plots give an idea of the kind of distributions that can be obtained using our method. Any other infrared-safe quantity could easily be calculated, however. Figure 6.7 shows the distributions of the following observables: the transverse-mass of the reconstructed top-quark, $M_T(t)$, the transverse hadronic-energy, $H_T(J_b, J_l^H)$, the transverse-momentum and pseudorapidity of the reconstructed top-quark, $p_T(t)$ and $\eta(t)$, the invariant-mass of the $l^+ \nu_l J_l^H$ system, $M_{\text{inv}}(l^+, \nu_l, J_l^H)$, and the cosine of the angle between the outgoing charged-lepton and the hardest light-parton jet in the rest-frame of the top quark, $\cos\theta$. These are defined as:

$$M_T(t) = \sqrt{|\vec{p}_\perp(J_b)|^2 + |\vec{p}_\perp(l^+)|^2 + \slashed{E}_T^2 - \left(\vec{p}_\perp(J_b) + \vec{p}_\perp(l^+) + \slashed{E}_T\right)^2}, \qquad (6.11)$$

$$H_T(J_b, J_l^H) = |\vec{p}_\perp(J_b)| + |\vec{p}_\perp(J_l^H)|, \qquad (6.12)$$

$$p_T(t) = |\vec{p}_\perp(t)|, \qquad (6.13)$$

$$\eta(t) = \frac{1}{2}\ln\left(\frac{|\vec{p}(t)| + |\vec{p}_\parallel(t)|}{|\vec{p}(t)| - |\vec{p}_\parallel(t)|}\right), \qquad (6.14)$$

$$M_{\text{inv}}(l^+, \nu_l, J_l^H) = \sqrt{\left(p(l^+) + p(\nu_l) + p(J_l^H)\right)^2}, \qquad (6.15)$$

$$\cos\theta = \left.\frac{\vec{p}(l^+) \cdot \vec{p}(J_l^H)}{|\vec{p}(l^+)||\vec{p}(J_l^H)|}\right|_t, \qquad (6.16)$$

where $\vec{p}_\parallel$ and $\vec{p}_\perp$ denote the components of momentum parallel and perpendicular to the beam axis respectively, $\slashed{E}_T \equiv \vec{p}_\perp(\nu_l)$ is the transverse missing-energy and $|_t$ indicates that the momenta are evaluated in the rest-frame of the reconstructed top-quark. Each of the plots shows the LO and NLO results, calculated using the off-shell treatment of
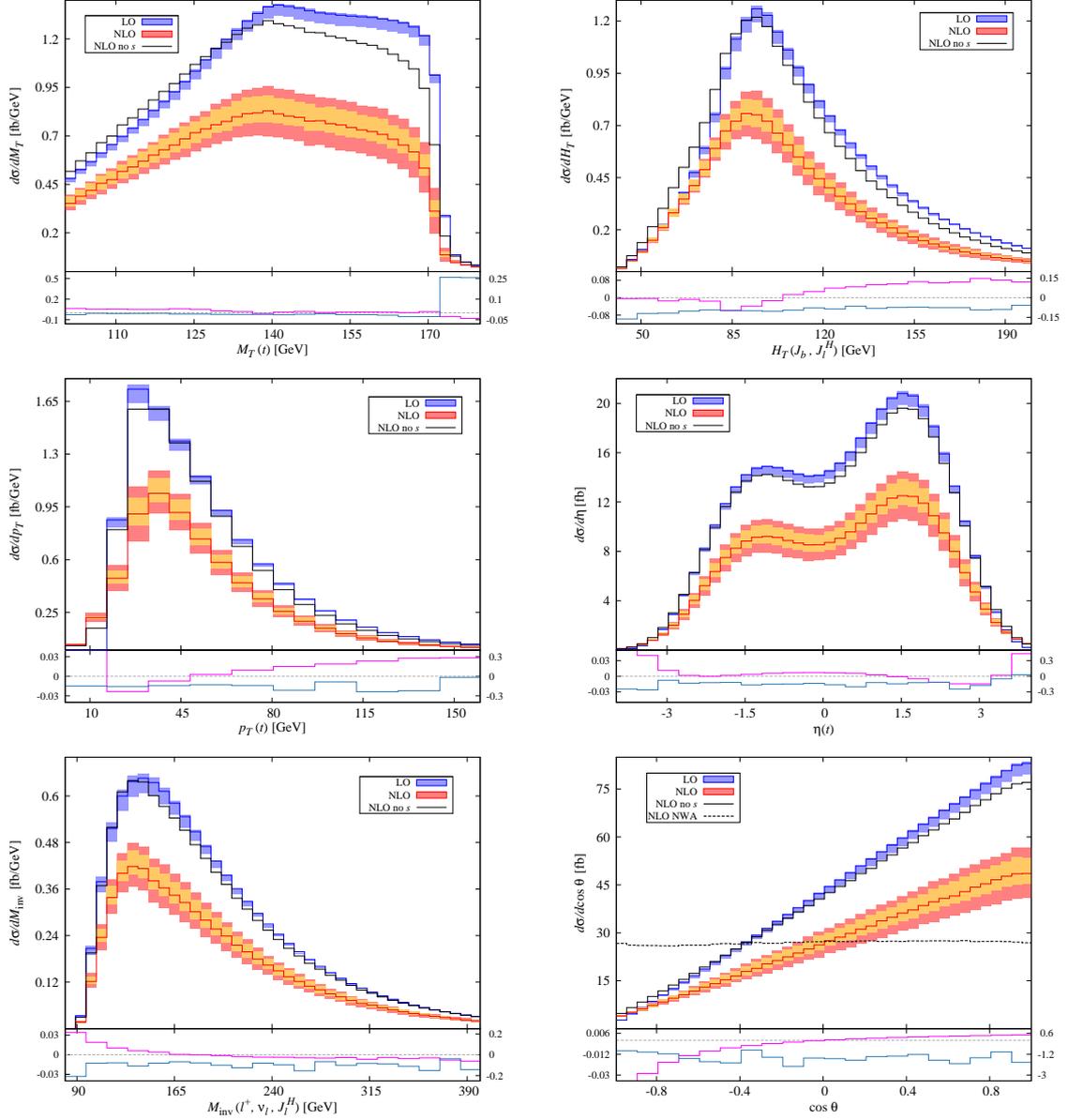
Figure 6.7: A selection of kinematic distributions for $p\bar{p} \to J_b J_l \, l^+ \not{E}_T + X$ at the Tevatron. Top: top-quark transverse-mass (left) and transverse hadronic-energy (right). Centre: top-quark transverse-momentum (left) and pseudorapidity (right). Bottom: $l^+ \nu_l J_l^H$ invariant-mass (left) and $\cos\theta$ (right). The upper panels show the differential cross section at LO (blue), NLO (red) and at NLO with the contributions from the 'wrong' process removed (black). The lower panels show the ratio of the off-shell effects (azure, left y-axis) and spin-correlation effects (magenta, right y-axis) to the full NLO result (red line in the upper plots). See text for more details.

the intermediate top-quark, as the blue and red bands respectively. As in the invariant-mass plots, the bands were obtained by varying the renormalisation and factorisation scales in the range, $m_t/4 \leq (\mu_R = \mu_F) \leq m_t$. The results obtained using the central scale, $m_t/2$, are shown as solid lines within the bands. The orange band shows the NLO result with only the factorisation scale varied, keeping the renormalisation scale fixed at the central value. The black line shows the unphysical off-shell NLO cross section obtained by artificially removing s-channel contributions (those containing a final state $\bar{b}$ quark) even if the $\bar{b}$-jet would not be detected, i.e. a perfect $\bar{b}$-jet veto. The difference between the red and black lines shows the size of the contributions of diagrams belonging to the 'wrong' process. The NLO results calculated using the NWA and iNWA treatments of the intermediate top-quark are not shown as they are, in general, very similar to the NLO off-shell results and could make the plots confusing. Instead, the lower panel of the plots shows the ratio of the off-shell and spin-correlation effects, defined in Eq. (5.74), to the full off-shell result at NLO. The azure line, with the left y-axis scale, shows the off-shell effects and the magenta line, with the right y-axis scale, shows the spin-correlation effects. The $\cos\theta$ plot also shows the NLO result obtained using the NWA treatment as a dashed black line in the upper panel. It is shown due to its vastly different shape to the results obtained using the iNWA and off-shell treatments in this particular distribution.

Considering all plots in Figure 6.7, we can see that, in general, the NLO contributions are large and negative. As discussed earlier, the majority of the NLO correction comes from the $qg \rightarrow q'bl^+\nu_l\bar{b}$ partonic process. This can be seen in the plots by comparing the red and black lines. Without this contribution, the NLO result, given by the black line, lies much closer to the LO result (blue line). The addition of the NLO corrections does not have a large effect on the overall shape of the distributions, although there are some subtle changes. At NLO, the peaks of the $H_T(J_b, J_l^H)$ and

$M_{\text{inv}}(l^+, \nu_l, J_l^H)$ distributions are shifted towards slightly smaller values, whereas the peak of the $p_T(t)$ distribution shifts to a slightly larger value. The $p_T(t)$ distribution also changes from having a sharp edge at low values, due to our kinematic cuts, to a smoother fall-off at NLO. The size of the off-shell and spin-correlation effects is dependent on the distribution. Generally, the off-shell effects amount to a negative correction of $\sim$ 2-3%. They can be much larger in certain kinematic regions and distributions, however. Good examples of this are the $M_T(t)$ distribution, in which the off-shell effects take their usual $\sim$ 2-3% value up to the region $M_T(t) \sim m_t$ when they become much larger, reaching up to $\sim$ 50%, and the $H_T(J_b, J_l^H)$ distribution, where the off-shell effects are larger than usual throughout, ranging from $\sim$ 3-10%. The spin-correlation effects also vary from distribution to distribution, but are often larger than the off-shell effects. Spin-correlation effects are particularly important in the $\cos\theta$ distribution, reaching over 300% in some bins. The reason for such large corrections is illustrated by the inclusion of the NLO NWA results in the plot (dashed black line). The observable $\cos\theta$ is the angle between the outgoing charged-lepton, which arises in the top-quark decay subprocess, and the hardest light-parton jet, which is likely to originate from the light-quark that is produced, along with the top quark, in the production subprocess. Without spin-correlations linking the production and decay subprocesses, we lose spin information and end up with a flat distribution over all possible angles. This observable constitutes a special case which is heavily dependent on spin-correlations and is not characteristic of most other observables, however. Many distributions display large spin-correlation effects towards their upper and/or lower boundaries. For example, at the upper and lower limits of the $\eta(t)$ and $p_T(t)$ distributions, the lower limit of the $M_{\text{inv}}(l^+, \nu_l, J_l^H)$ distribution and the upper limit of the $H_T(J_b, J_l^H)$ distribution. In these regions, effects of up to $\sim$ 30% are not uncommon.
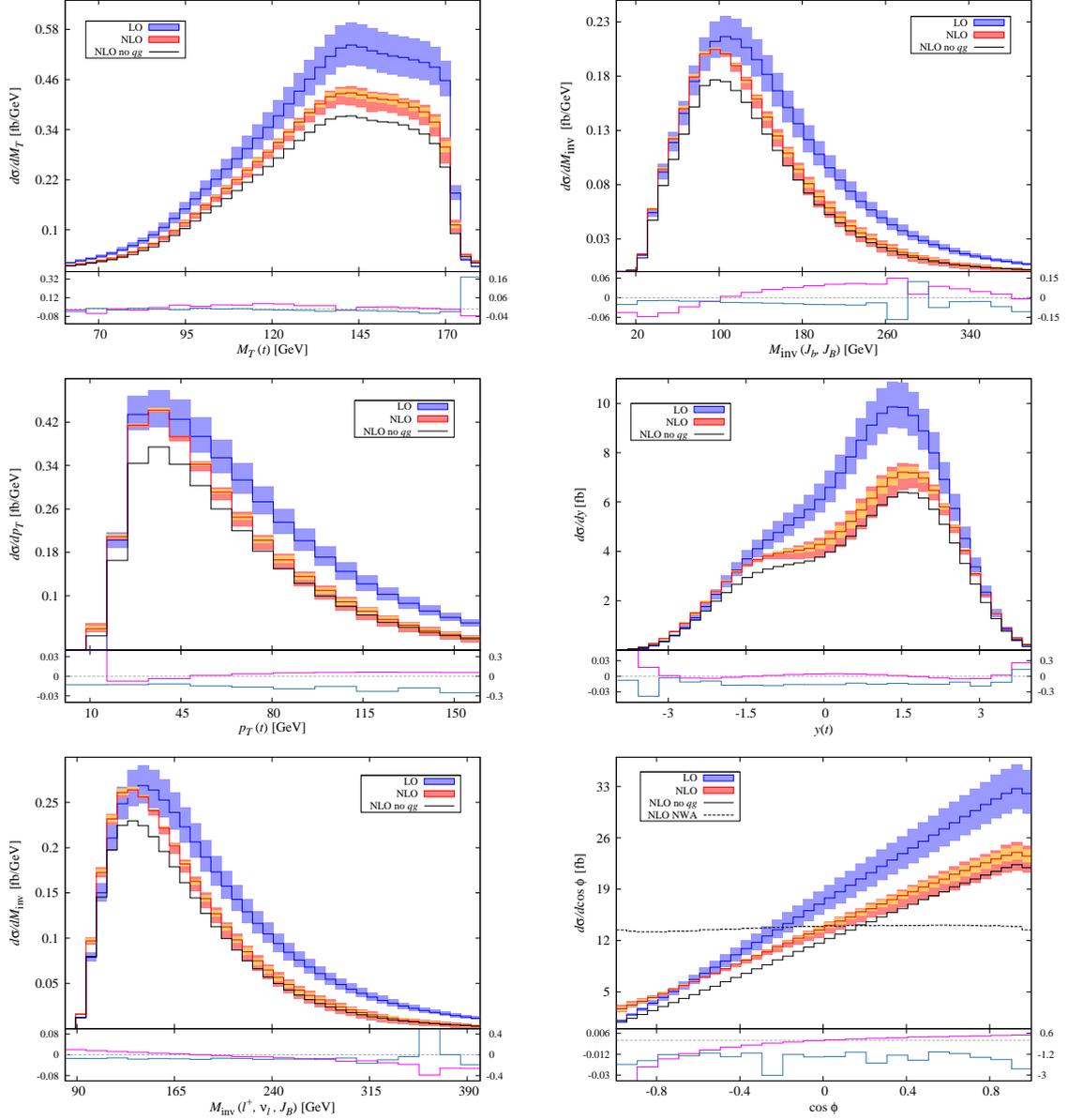
Figure 6.8: A selection of kinematic distributions for $p\bar{p} \to J_b J_{\bar{b}} \, l^+ \not{E}_T + X$ at the Tevatron. Top: top-quark transverse-mass (left) and $J_b J_{\bar{b}}$ invariant-mass (right). Centre: top-quark transverse-momentum (left) and rapidity (right). Bottom: $l^+ \nu_l J_{\bar{b}}$ invariant-mass (left) and $\cos\phi$ (right). The upper panels show the differential cross section at LO (blue), NLO (red) and at NLO with the contributions from the 'wrong' process removed (black). The lower panels show the ratio of the off-shell effects (azure, left y-axis) and spin-correlation effects (magenta, right y-axis) to the full NLO result (red line in the upper plots). See text for more details.

For the double b-jet process, we present the distributions of the following observables: the transverse-mass of the reconstructed top-quark, $M_T(t)$, the invariant-mass of the b- and $\bar{b}$-jets, $M_{\text{inv}}(J_b, J_{\bar{b}})$, the transverse-momentum and rapidity of the reconstructed top-quark, $p_T(t)$ and $y(t)$, the mis-reconstructed top-quark invariant-mass, i.e. the invariant-mass of the $l^+ \nu_l J_{\bar{b}}$ system, $M_{\text{inv}}(l^+, \nu_l, J_{\bar{b}})$, and the cosine of the angle between the outgoing charged-lepton and the incoming anti-proton beam in the rest-frame of the top quark, $\cos\phi$. These are defined as:

$$M_{\text{inv}}(J_b, J_{\bar{b}}) = \sqrt{\left(p(J_b) + p(J_{\bar{b}})\right)^2}\,, \tag{6.17}$$

$$y(t) = \frac{1}{2}\ln\left(\frac{E(t) + |\vec{p}_\parallel(t)|}{E(t) - |\vec{p}_\parallel(t)|}\right)\,, \tag{6.18}$$

$$M_{\text{inv}}(l^+, \nu_l, J_{\bar{b}}) = \sqrt{\left(p(l^+) + p(\nu_l) + p(J_{\bar{b}})\right)^2}\,, \tag{6.19}$$

$$\cos\phi = \left.\frac{\vec{p}(l^+) \cdot \vec{p}(\bar{p})}{|\vec{p}(l^+)||\vec{p}(\bar{p})|}\right|_t\,, \tag{6.20}$$

with $E(t)$ the energy of the reconstructed top-quark and $\vec{p}(\bar{p})$ the three-momentum of the incoming anti-proton. $M_T(t)$ and $p_T(t)$ are defined as in Eqs. (6.11) and (6.13). These distributions are shown in Figure 6.8. As before, the LO and NLO results are shown in blue and red respectively, with the bands obtained by varying the scale. The orange band comes from varying the factorisation scale only. In this case, the black line represents the NLO result with the t-channel contribution artificially removed, i.e. without the $qg \rightarrow q'bl^+\nu_l\bar{b}$ partonic process included. The lower panels show the ratio of the off-shell (azure, left y-axis) and spin-correlation (magenta, right y-axis) effects to the full off-shell NLO result (red line, upper panel).

For this process, the NLO effects are smaller than those of the single b-jet process, but are still negative. The inclusion of the $qg \rightarrow q'bl^+\nu_l\bar{b}$ partonic process also has a different effect. In the single b-jet case, removing this process vastly reduced the

size of the NLO corrections, whereas, in this case, the size of the NLO corrections is increased by its removal. This can be seen by comparing the red and black lines in the upper panels of the figure. The reduction in scale dependence from LO to NLO is also evident in the plots, with the red bands being narrower than the blue bands. Again, the inclusion of NLO effects does not dramatically affect the overall shape of the distributions, but does cause a small shift in the peaks of the two invariant-mass distributions. In this case, there is also a slight change in the shape of the top-quark rapidity distribution. In the region $-2 \leq y(t) \leq 0$ GeV, the NLO result (red) is much flatter than either the LO result (blue) or the NLO result with the 'wrong' process removed (black). This suggests that it is the inclusion of the $qg \to q'bl^+\nu_l\bar{b}$ partonic process that is causing this change of shape. The off-shell and spin-correlation effects also display similar behaviour to the single b-jet case. In general, the off-shell effects account for a negative correction of $\sim$ 1-3%, with the exception of the $M_T(t) = m_t$ boundary where they reach $\sim$ 30%. The spin-correlation effects are again very large for the angular distribution, $\cos\phi$, and towards the edges of some distributions, $p_T(t)$ and $y(t)$, for example, but are generally small around the distribution peak. Their effect in the $M_{\text{inv}}(J_b, J_{\bar{b}})$ is particularly interesting, with corrections reaching $\pm15\%$ in various parts of the distribution.

In both processes, the off-shell effects are much smaller than we may naïvely expect after observing the top-quark invariant-mass distributions (Figure 6.6), where their contribution can be as great as 60-70% in some bins. This is likely a result of an averaging effect over the top-quark invariant-mass. While the off-shell contributions are large around the invariant-mass peak, they also contain a sign change. Therefore, when integrated over the full range, their total effect on, for example, the cross section is only small, $\sim 2\%$. This reasoning can also be applied to many of the other observables which are only indirectly related to the top-quark invariant-mass. For a fixed value of

an observable, there are a number of kinematic configurations which can give rise to this value. Assuming the observable is not too closely related to the top-quark invariant-mass, each of these kinematic configurations may give a different $m_{\mathrm{inv}}(t)$ value. In some of these configurations, $m_{\mathrm{inv}}(t)$ may fall into the region near the peak, where the off-shell corrections are large and negative. However, in other configurations, $m_{\mathrm{inv}}(t)$ may fall into the region where the off-shell corrections are large and positive. Averaging over all of these kinematic configurations has a similar effect to averaging over the top-quark invariant-mass distribution, leaving us with a small, negative off-shell correction. A good illustration of this effect can be seen if we consider the $M_T(t)$ distribution. The transverse-mass of the top quark is constrained to be smaller than the invariant-mass of the top quark, so we may investigate certain kinematic regions. For a fixed $M_T(t)$ value, the top-quark invariant-mass must be in the range $M_T(t) \leq m_{\mathrm{inv}}(t) \leq 200$ GeV, where the upper limit comes from the cut we applied to the process. For $M_T(t) < 160$ GeV, we encompass a large range of invariant-mass values and the averaging of the off-shell contributions works effectively, giving an overall negative correction of $\sim$ 1-3%. However, as we move to transverse-mass values closer to the invariant-mass peak, the averaging becomes less effective. In the region $160 < M_T(t) < 170$ GeV, we lose the positive contributions to the off-shell effects which are present just below the peak. These can be seen in the lower panels of the plots in Figure 6.6. This leads to the off-shell effects in the transverse-mass plots becoming more negative in this region. The most noticeable effect occurs at $M_T(t)$ values above m_t. Here, the large negative peak in the off-shell effects is no longer included in our invariant-mass range and, therefore, the averaging does not occur. Instead, we include only the large positive peak and the remaining positive contributions from $m_{\mathrm{inv}}(t) > m_t$, leading to large, positive off-shell corrections to the $M_T(t)$ distribution. This can be seen in the lower panels of the $M_T(t)$ plots in Figures 6.7 and 6.8. In this particular case, we can see the effect in action as
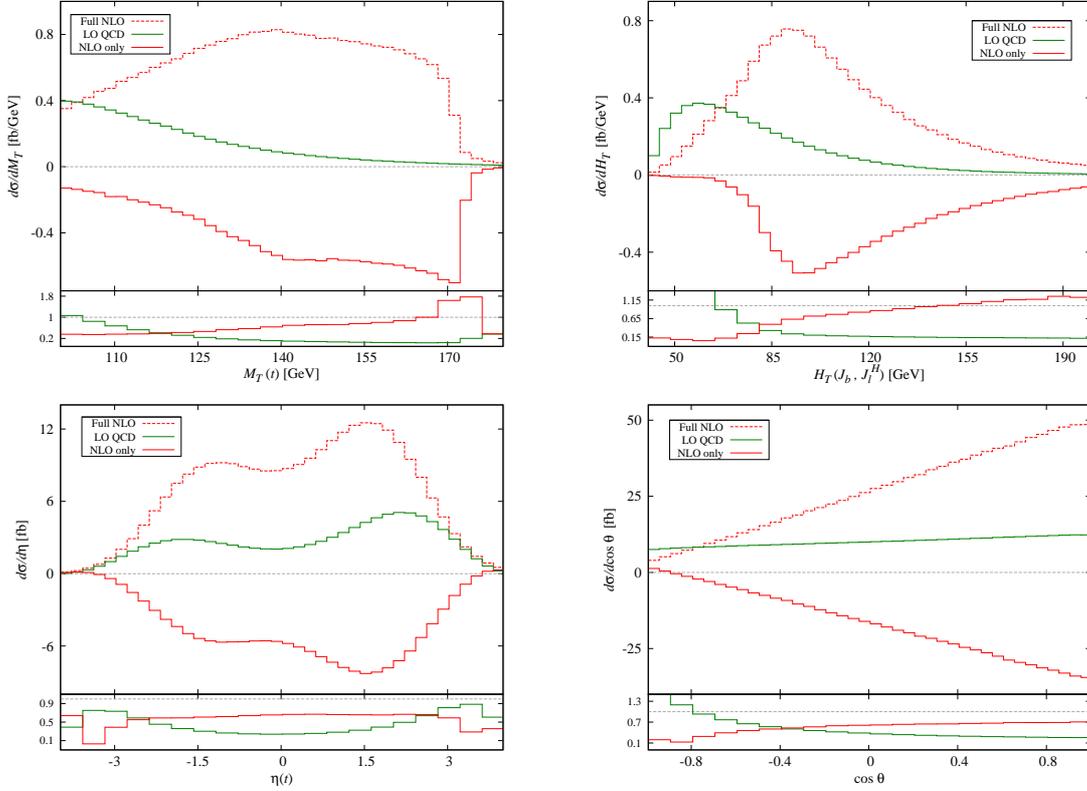
Figure 6.9: A selection of kinematic distributions for $p\bar{p} \to J_b J_l\, l^+ \not{E}_T + X$ at the Tevatron. Top: top-quark transverse-mass (left) and transverse hadronic-energy (right). Bottom: top-quark pseudorapidity (left) and $\cos\theta$ (right). The upper panels show the full NLO differential cross section (dashed red), the NLO contribution only (solid red) and at LO QCD contribution (green). The lower panels show the ratio of the absolute value of the NLO contribution (red) and QCD contribution (green) to the full NLO result (dashed red line in the upper plots). See text for more details.

the transverse- and invariant-masses are closely related. In other distributions, we do not have this relation and the averaging effect over the invariant-mass values occurs as it did for the lower $M_T(t)$ values, leaving only a small residual effect.

As discussed in Section 5.8, our choice of top-quark invariant-mass window affects the suppression of other diagrams. While we saw that choosing a smaller invariant-mass window increased the suppression, and would ideally be required for our δ-counting to apply, this would not generally be done experimentally. Instead, we chose a more

realistic experimental window with the knowledge that our counting may not be entirely satisfied. In light of this, the least suppressed contribution, that of the tree-level QCD-mediated diagrams, was also calculated. The results of this calculation, for some distributions of the single b-jet process, are shown in Figure 6.9. The upper panels of the plots show the differential cross section, calculated using the off-shell treatment of the intermediate top-quark, at NLO to $\mathcal{O}(\delta^{3/2})$ as the dashed red line, the NLO contributions only (i.e. the contributions suppressed by a factor $\sim \delta^{1/2}$ compared to our LO result) as the solid red line, and the LO QCD-mediated diagrams (suppressed by a factor $\sim \delta$ compared to our LO result) as the solid green line. The lower panels of the plots show the ratio of the absolute value of the NLO contributions and the LO QCD contributions to the full NLO result as the red and green lines respectively. If our counting were working perfectly, we would expect to see the QCD contributions suppressed by a factor $\sim \delta^{1/2}$ with respect to the NLO contributions. As expected, due to our large invariant-mass window, however, this is not observed. Overall, the QCD contributions are suppressed with respect to the NLO contributions, having a smaller absolute value of total cross section (20.1 fb compared to 33.3 fb). The suppression is not as large as we would have hoped, however. The importance of the QCD contributions is very dependent on the kinematical region and the distribution. For some distributions, the QCD and NLO contributions can be disentangled due to having qualitatively different shapes. Examples of such distributions are the top-quark transverse-mass, $M_T(t)$, the hadronic transverse-energy, $H_T(J_b, J_l^H)$, and $\cos\theta$. In the first two examples, the QCD and NLO contributions contain peaks in different kinematic regions. Here, the QCD effects dominate in a small kinematic region of the distribution and then show suppression of $\sim \delta^{1/2}$, as originally hoped, throughout the rest of the distribution. In the angular distribution, the QCD contribution amounts to an almost constant shift in the distribution due to its flat shape. For other distributions, such as the top-quark pseu-

$pp \to J_b J_l \, l^+ \, \not{E}_T + X$	$pp \to J_b J_{\bar{b}} \, l^+ \, \not{E}_T + X$
$p_T(J_b) \geq 20$ GeV	$p_T(J_b) \geq 20$ GeV
$p_T(J_l^H) \geq 20$ GeV	$p_T(J_{\bar{b}}) \geq 30$ GeV
$p_T(J_{\bar{b}}) < 15$ GeV	$p_T(J_l) < 15$ GeV
$\left(\not{E}_T + p_T(l^+) \right) \geq 60$ GeV	$\left(\not{E}_T + p_T(l^+) \right) \geq 60$ GeV
$120 \leq m_{\mathrm{inv}}(t) \leq 200$ GeV	$120 \leq m_{\mathrm{inv}}(t) \leq 200$ GeV

Table 6.5: Kinematical cuts applied to the two considered processes at the LHC.

dorapidity, however, the QCD contributions have the same overall shape as the NLO contributions and the suppression shows less dependence on the kinematic region. In general, the LO QCD contribution is suppressed with respect to the NLO contribution across a large percentage of each distribution. While the suppression is not as large as originally predicted, the reasons for this are understood and could be addressed in future work.

6.3 LHC Results

The next set of results we present are for the LHC with a centre-of-mass energy, $\sqrt{s} = 7$ TeV. The kinematical cuts applied to our two processes of interest, Eqs. (6.8) and (6.9), are shown in Table 6.5. The cuts applied on both processes are very similar to those used for the Tevatron, but with a harder cut on the transverse-momenta of the W-boson decay products.

The cross sections of the two processes are given, at LO and NLO in our counting, in Table 6.6. Results calculated using both the NWA and iNWA treatments of the top quark are also given for comparison. The total NLO corrections to the single b-jet

		σ_{NWA}	σ_{iNWA}	$\sigma_{\text{off−shell}}$
$pp \to J_b J_l \, l^+ \not{E}_T + X$	LO [pb]	3.526(1)	3.505(1)	$3.460(1)^{+0.278}_{-0.403}$
	NLO [pb]	1.643(1)	1.642(1)	$1.609(6)^{+0.303}_{-0.240}$
$pp \to J_b J_{\bar{b}} \, l^+ \not{E}_T + X$	LO [pb]	0.1678(1)	0.1677(1)	$0.1654(1)^{+0.0001}_{-0.0010}$
	NLO [pb]	0.1634(1)	0.1636(1)	$0.1618(4)^{+0.0021}_{-0.0005}$

Table 6.6: The LO and NLO cross sections for $pp \to J_b J_l \, l^+ \not{E}_T + X$ and $pp \to J_b J_{\bar{b}} \, l^+ \not{E}_T + X$ at the 7 TeV LHC, calculated using the NWA, iNWA and off-shell top-quark treatments. Numbers in brackets represent Monte Carlo errors. The subscript and superscript values on the off-shell results are errors arising from scale uncertainty only.

process are very large, amounting to $\sim 50\%$ of the LO value, whereas for the double b-jet process they are very small, amounting to only $\sim 2\%$ of the LO value. As for the Tevatron results, the differences between the three heavy-particle treatments are small, with the off-shell effects typically being $\sim 1\%$.

As in Section 6.2, the subscripts and superscripts on the off-shell cross sections in Table 6.6 were obtained by varying the renormalisation and factorisation scales in the range $[m_t/4, \, m_t]$. We see a small reduction in the scale dependence as we move from LO to NLO in the single b-jet process, but a small increase in the double b-jet process. Scale dependence plots for both processes are shown in Figure 6.10. In the single b-jet case, we can again attribute much of the NLO scale dependence to the introduction of a renormalisation-scale dependence, which is missing at LO. This is clear when we compare the NLO scale dependence with fixed renormalisation scale (red dotted line) to the case where the two scales are varied simultaneously (solid red line). The dotted line is much flatter, showing little scale dependence across the whole range of scale values shown. For the double b-jet case, there is little difference between the NLO scale-dependence with fixed or varied renormalisation scale. Instead, our increase in scale dependence is due to our choice of central scale. In the region we take, the LO dependence is quite weak but the NLO dependence is strong. However, had we taken
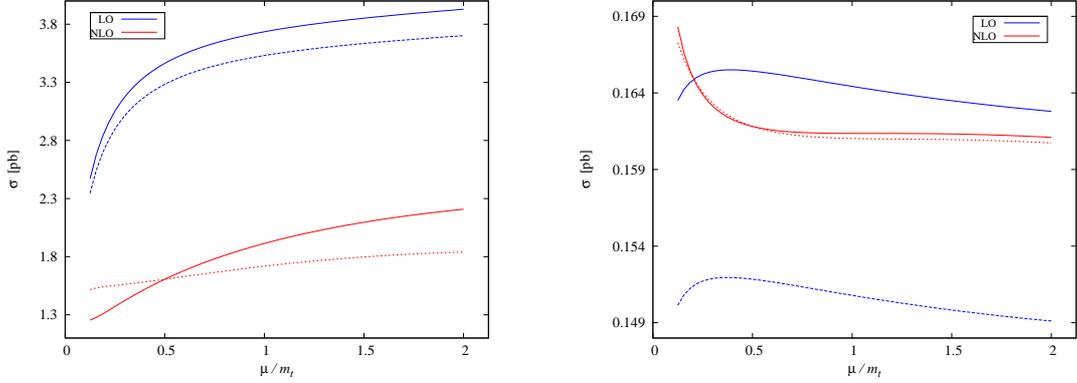
Figure 6.10: Scale dependence for $pp \to J_b J_l \, l^+ \not{E}_T + X$ (left plot) and $pp \to J_b J_{\bar{b}} \, l^+ \not{E}_T + X$ (right plot) at the 7 TeV LHC. The plot shows the scale dependence of the LO cross section using LO PDFs (dashed blue) and NLO PDFs (solid blue), and the scale dependence of the NLO cross section using NLO PDFs while varying the factorisation scale only, leaving the renormalisation scale fixed (dotted red), and while varying both scales simultaneously (solid red).

a larger central scale, we would have hit the region above $\mu \sim m_t/2$ where we still have some dependence at LO but the NLO dependence is almost flat.

Splitting the cross sections, calculated using the off-shell heavy-particle treatment, into their respective partonic processes, given in Eqs. (6.1)-(6.7), we obtain the results shown in Table 6.7. The processes $qb \to q'bl^+\nu_l(g)$ and $Q\bar{Q}' \to \bar{b}bl^+\nu_l(g)$ in the table represent the sum of the one-loop corrections to the tree-level process and the real corrections defined by the tree-level process with an extra emitted gluon. For the single b-jet process, almost all of the full NLO cross section ($\sim 99.5\%$) comes from the t-channel diagrams, with the s-channel diagrams comprising only $\sim 0.5\%$. However, for the double b-jet process, the s-channel diagrams contribute $\sim 41\%$ of the full NLO cross section, with the t-channel diagrams making up the remaining $\sim 59\%$. Despite applying cuts specifically designed to suppress t-channel contributions to the s-channel cross section, they are dominant. This is largely due to the fact that, at the LHC, the t-channel production cross section is much larger than that of the s-channel, as shown in Table 1.2. We can again see the importance of the $qg \to q'bl^+\nu_l\bar{b}$ partonic process

	Partonic process	$pp \to J_b J_l\, l^+ \not{E}_T + X$	$pp \to J_b J_{\bar{b}}\, l^+ \not{E}_T + X$
LO [pb]	$qb \to q'b l^+ \nu_l$	3.460(1)	-
	$Q\bar{Q}' \to \bar{b}b l^+ \nu_l$	-	0.1654(1)
NLO [pb]	$qb \to q'b l^+ \nu_l(g)$	$-0.427(9)$	-
	$gb \to q'b l^+ \nu_l \bar{q}$	$-0.0532(1)$	-
	$qg \to q'b l^+ \nu_l \bar{b}$	$-1.362(4)$	0.0949(1)
	$Q\bar{Q}' \to \bar{b}b l^+ \nu_l(g)$	0.0068(1)	$-0.0747(2)$
	$Qg \to \bar{b}b l^+ \nu_l\, Q'$	0.0012(1)	$-0.0243(1)$

Table 6.7: The contributions of the various partonic processes to the LO and NLO cross sections for $pp \to J_b J_l\, l^+ \not{E}_T + X$ and $pp \to J_b J_{\bar{b}}\, l^+ \not{E}_T + X$ at the 7 TeV LHC. Cross sections were calculated using the off-shell top-quark treatment. Numbers in brackets represent Monte Carlo errors.

to both channels. For the single b-jet process, its contribution makes up $\sim 75\%$ of the total NLO correction, while for the double b-jet process its contribution cancels that of the other NLO partonic processes almost exactly.

We will now look at the top-quark invariant-mass distributions of the two processes. These are shown in Figure 6.11. As in the Tevatron case, the blue and red bands show the LO and NLO results obtained using the off-shell treatment of the top quark, with the bands obtained by varying the scale in the range $m_t/4 \leq (\mu_R = \mu_F) \leq m_t$. The green line shows the NLO result obtained using the iNWA treatment. We observe similar effects to those seen in the Tevatron case. The peak at $m_{\text{inv}}(t) = m_t$ decreases and becomes broader as we move from the iNWA treatment to the off-shell treatment. The off-shell effects are large and contain a sign change around the peak. The spin-correlation effects are small throughout. Away from the peak, the behaviour differs for the single b-jet and double b-jet processes. For the single b-jet process, in the region $m_{\text{inv}}(t) < m_t$, there is little difference between the iNWA and off-shell treatments, both being substantially larger than the LO off-shell result. For $m_{\text{inv}}(t) > m_t$, we see that
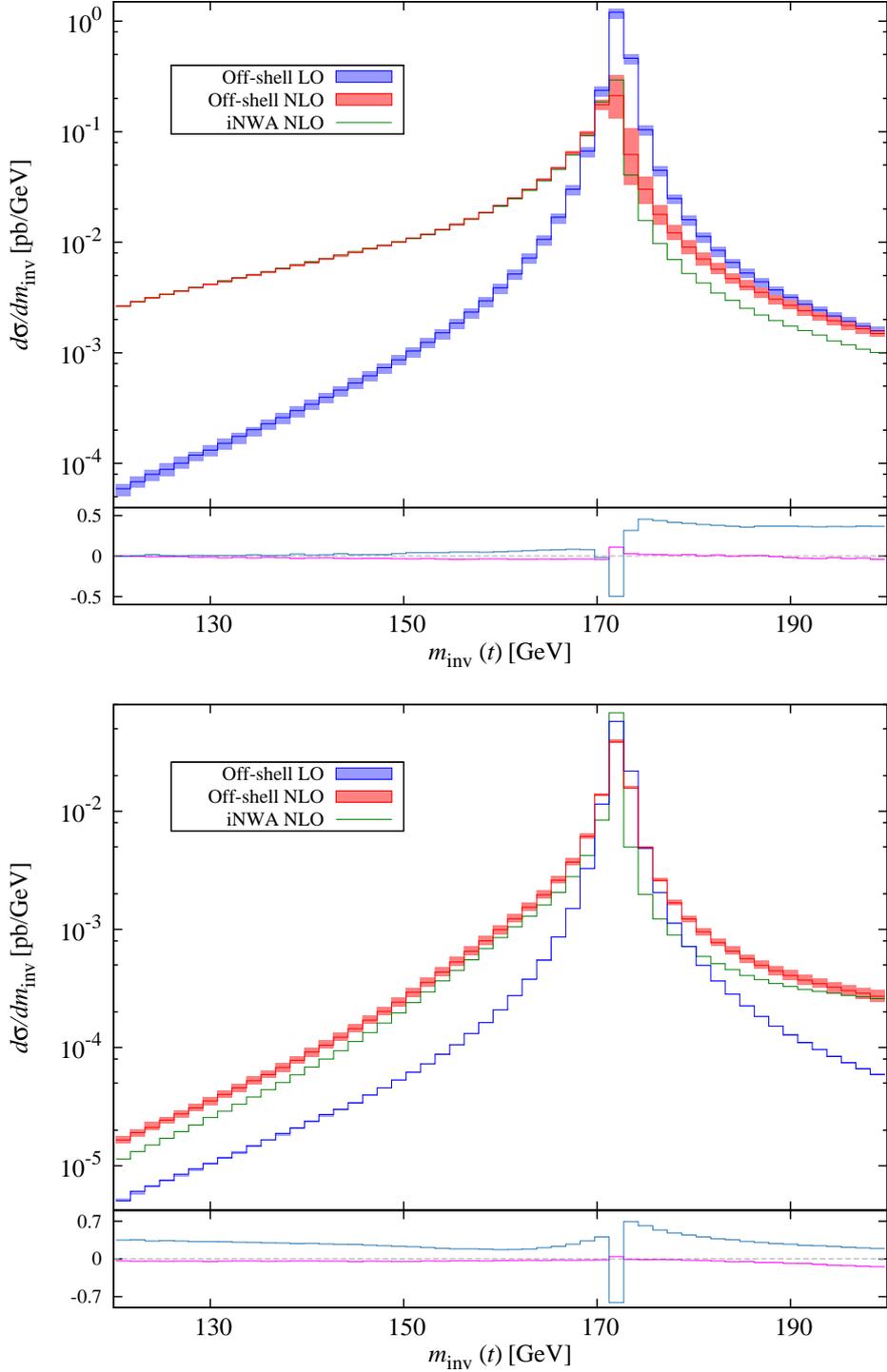
Figure 6.11: The top-quark invariant-mass distribution at LO (blue band) and NLO (red band) in the off-shell treatment and NLO in the iNWA treatment (green) for $pp \to J_b J_l \, l^+ \, \not{E}_T + X$ (upper plot) and $pp \to J_b J_{\bar{b}} \, l^+ \, \not{E}_T + X$ (lower plot) at the 7 TeV LHC. The lower panel of the plots shows the ratio of the off-shell effects (azure) and spin-correlation effects (magenta) to the full off-shell NLO result.

the NLO results lie below the LO result, with the difference between the two becoming gradually smaller as $m_{\text{inv}}(t)$ increases. The difference between the NLO iNWA and off-shell results remains approximately constant, with the iNWA treatment having a smaller value than the off-shell treatment. This can be seen by the almost flat shape of the off-shell effects in the lower panel of the figure. For the double b-jet process, in the region $m_{\text{inv}}(t) < m_t$, we see an increasing difference between the NLO iNWA and off-shell results as $m_{\text{inv}}(t)$ decreases, with both results being much closer to the LO result than in the single b-jet case. For $m_{\text{inv}}(t) > m_t$, the NLO results quickly become larger than the LO result and the difference between the iNWA and off-shell results decreases as $m_{\text{inv}}(t)$ increases.

Plots of the same kinematic distributions presented for the Tevatron, defined in Eqs. (6.11)-(6.20), are shown, for the single b-jet and double b-jet processes, in Figures 6.12 and 6.13 respectively. The LO and NLO results, obtained using the off-shell treatment of the intermediate top-quark, are shown in blue and red respectively, with the bands obtained by varying the renormalisation and factorisation scales in the range $m_t/4 \leq (\mu_R = \mu_F) \leq m_t$. The orange band comes from varying the factorisation scale only, leaving $\mu_R = m_t/2$. The values obtained using the central scale are shown as solid blue and red lines. The black lines represent the NLO result with the 'wrong' contributions artificially removed. That is, for the single b-jet process we artificially remove the s-channel contributions (those containing a $\bar{b}$-quark in the final state), and for the double b-jet process we artificially remove the t-channel contribution (the $qg \to q'bl^+\nu_l\bar{b}$ partonic process). The lower panels show the ratio of the off-shell (azure, left y-axis) and spin-correlation (magenta, right y-axis) contributions to the full NLO result (red line, upper panel). The NLO result calculated using the NWA treatment of the top quark is also shown as a dashed black line in the angular distributions, $\cos\theta$ and $\cos\phi$, to illustrate the large spin-correlation effects present in these distributions.
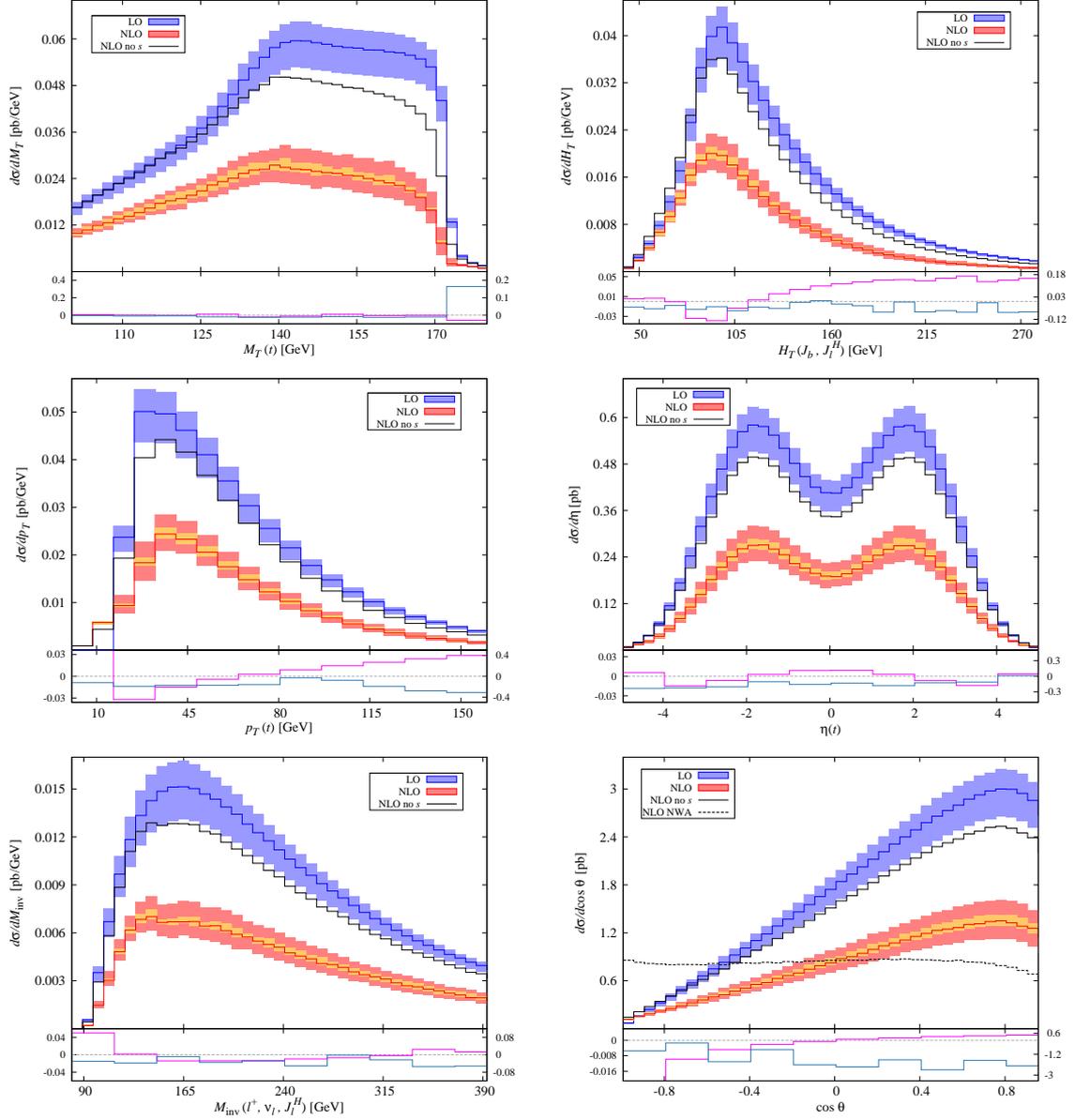
Figure 6.12: A selection of kinematic distributions for $pp \to J_b J_l\, l^+ \not{E}_T + X$ at the 7 TeV LHC. Top: top-quark transverse-mass (left) and transverse hadronic-energy (right). Centre: top-quark transverse-momentum (left) and pseudorapidity (right). Bottom: $l^+ \nu_l J_l^H$ invariant-mass (left) and $\cos\theta$ (right). The upper panels show the differential cross section at LO (blue), NLO (red) and at NLO with the contributions from the 'wrong' process removed (black). The lower panels show the ratio of the off-shell effects (azure, left y-axis) and spin-correlation effects (magenta, right y-axis) to the full NLO result (red line in the upper plots). See text for more details.

Figure 6.13: A selection of kinematic distributions for $pp \to J_b J_{\bar{b}} l^+ \not{E}_T + X$ at the 7 TeV LHC. Top: top-quark transverse-mass (left) and $J_b J_{\bar{b}}$ invariant-mass (right). Centre: top-quark transverse-momentum (left) and rapidity (right). Bottom: $l^+ \nu_l J_{\bar{b}}$ invariant-mass (left) and $\cos\phi$ (right). The upper panels show the differential cross section at LO (blue), NLO (red) and at NLO with the contributions from the 'wrong' process removed (black). The lower panels show the ratio of the off-shell effects (azure, left y-axis) and spin-correlation effects (magenta, right y-axis) to the full NLO result (red line in the upper plots). See text for more details.

If we first consider the results for the single b-jet process, shown in Figure 6.12, we observe similar effects to those seen in the Tevatron results. The NLO corrections are large and negative, with a large percentage of these corrections coming from the $qg \to q'bl^+\nu_l\bar{b}$ partonic process, as can be seen by comparing the red and black lines in the figure. The inclusion of the NLO corrections has only a minor effect on the overall shape of the distributions, such as slightly shifting the peak of the $H_T(J_b, J_l^H)$ and $p_T(t)$ distributions. We also observe a small decrease in the scale dependence as we move from LO to NLO. The off-shell effects are again small and negative, in general $\sim$ 1-3%, except close to some kinematic thresholds, such as the edge of the $M_T(t)$ distribution at m_t. The spin-correlation effects are small in most cases, with the exception of the edges of some distributions, such as $H_T(J_b, J_l^H)$, $p_T(t)$ and $\eta(t)$, and in the $\cos\theta$ distribution, where the shape of the spin-correlated and non-spin-correlated distributions are qualitatively different.

For the double b-jet process at the LHC (Figure 6.13), the off-shell and spin-correlation effects display the same behaviour as for the single b-jet process at the LHC and the two processes at the Tevatron. The shapes of the distributions, however, show large differences. As shown in Tables 6.6 and 6.7, the total NLO corrections are small. These corrections are comprised of two pieces, however. The s-channel piece contributes a large, negative correction, as can be seen from the black line in the plots, whereas the t-channel piece contributes a large, positive correction. These two contributions largely cancel one another out, leading to a small overall NLO contribution in the total cross sections. The large contribution of the t-channel piece causes the shapes of the distributions to become distorted, however. In particular, for distributions such as $M_{\text{inv}}(J_b, J_{\bar{b}})$, $p_T(t)$, $y(t)$ and $M_{\text{inv}}(l, \nu_l, J_{\bar{b}})$, the NLO contribution is sizeable and positive around the peak of the distribution, and negative in the tail. The peaks of these distributions are also shifted slightly with respect to the LO peaks. The change
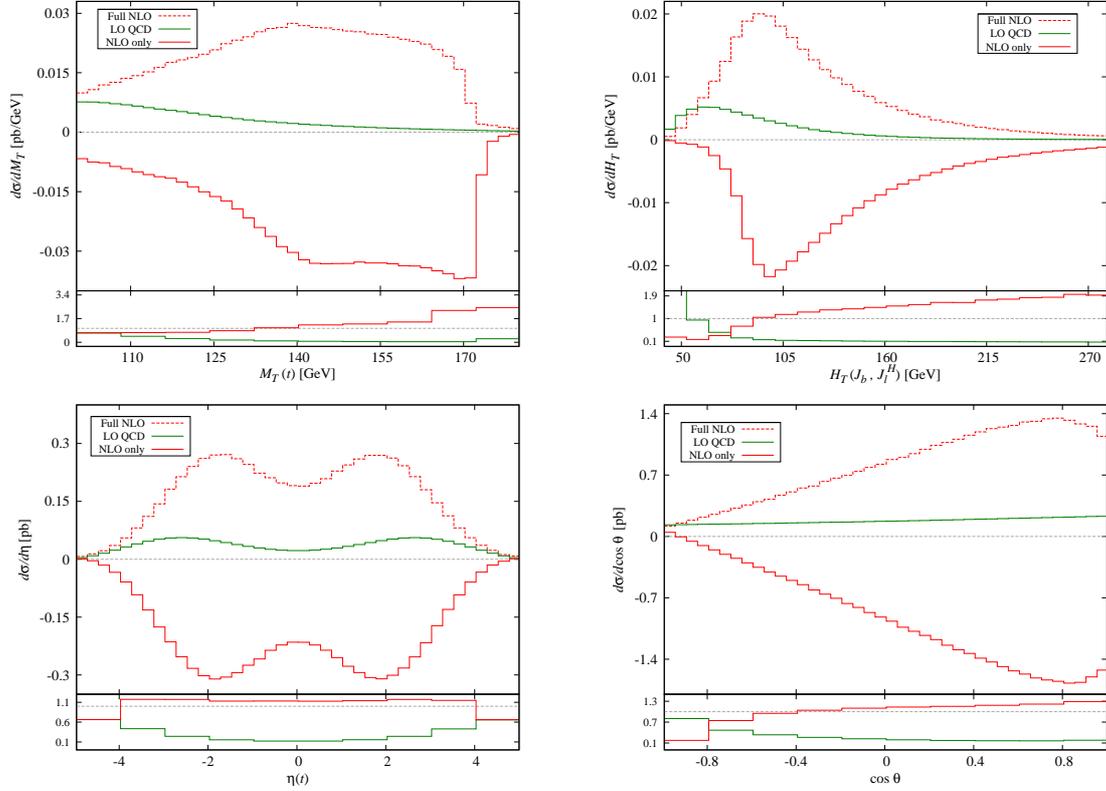
Figure 6.14: A selection of kinematic distributions for $pp \rightarrow J_b J_l \, l^+ \not{E}_T + X$ at the 7 TeV LHC. Top: top-quark transverse-mass (left) and transverse hadronic-energy (right). Bottom: top-quark pseudorapidity (left) and $\cos \theta$ (right). The upper panels show the full NLO differential cross section (dashed red), the NLO contribution only (solid red) and at LO QCD contribution (green). The lower panels show the ratio of the absolute value of the NLO contribution (red) and QCD contribution (green) to the full NLO result (dashed red line in the upper plots). See text for more details.

in shape of the distributions is particularly noticeable for the top-quark rapidity, $y(t)$, where the plateau, observed at LO and at NLO without the t-channel contribution, is completely removed, instead becoming a central peak when the t-channel contribution is included. The small scale dependence at both LO and NLO, with a slight increase as we move from LO to NLO, is very evident in the plots. The reasons behind this were discussed earlier.

$pp \to J_b J_l\, l^+ \not{E}_T + X$	
$p_T(J_b) \geq 20$ GeV	$\eta(J_b) \leq 2.5$
$p_T(l^+) \geq 20$ GeV	$\eta(l^+) \leq 2.5$
$p_T(J_l^H) \geq 20$ GeV	$\eta(J_l^H) \leq 2.0$
$120 \leq m_{\mathrm{inv}}(t) \leq 200$ GeV	$\not{E}_T \geq 20$ GeV

Table 6.8: Kinematical cuts applied to the t-channel process at the LHC, for comparison to results in the literature.

Comparing the size of the off-shell NLO contributions to those coming from the tree-level QCD-mediated diagrams for some distributions of the single b-jet process, as we did for the Tevatron, we obtain the plots shown in Figure 6.14. The QCD and NLO contributions are shown in green and red respectively, with the full NLO result shown as the dashed red line. The lower panels of the plots show the ratio of the absolute value of the two contributions to the full NLO result. In general, the QCD contributions are more suppressed at the LHC than at the Tevatron, with the NLO contributions dominating across most of the distribution. There are still some kinematic regions, however, where the QCD contributions are larger than the NLO contributions. These tend to occur when the shapes of the NLO and QCD distributions peak in different regions, making the separation of signal and background somewhat easier.

6.4 Comparison to Existing Results

The size of the NLO corrections presented in Sections 6.2 and 6.3 are, in general, much larger than those found in the literature, for example, in Ref. [40]. This large discrepancy is down to the kinematical cuts chosen. In particular, the strong vetoes on the extra jets. As a check of the validity of our results, we performed our calculation
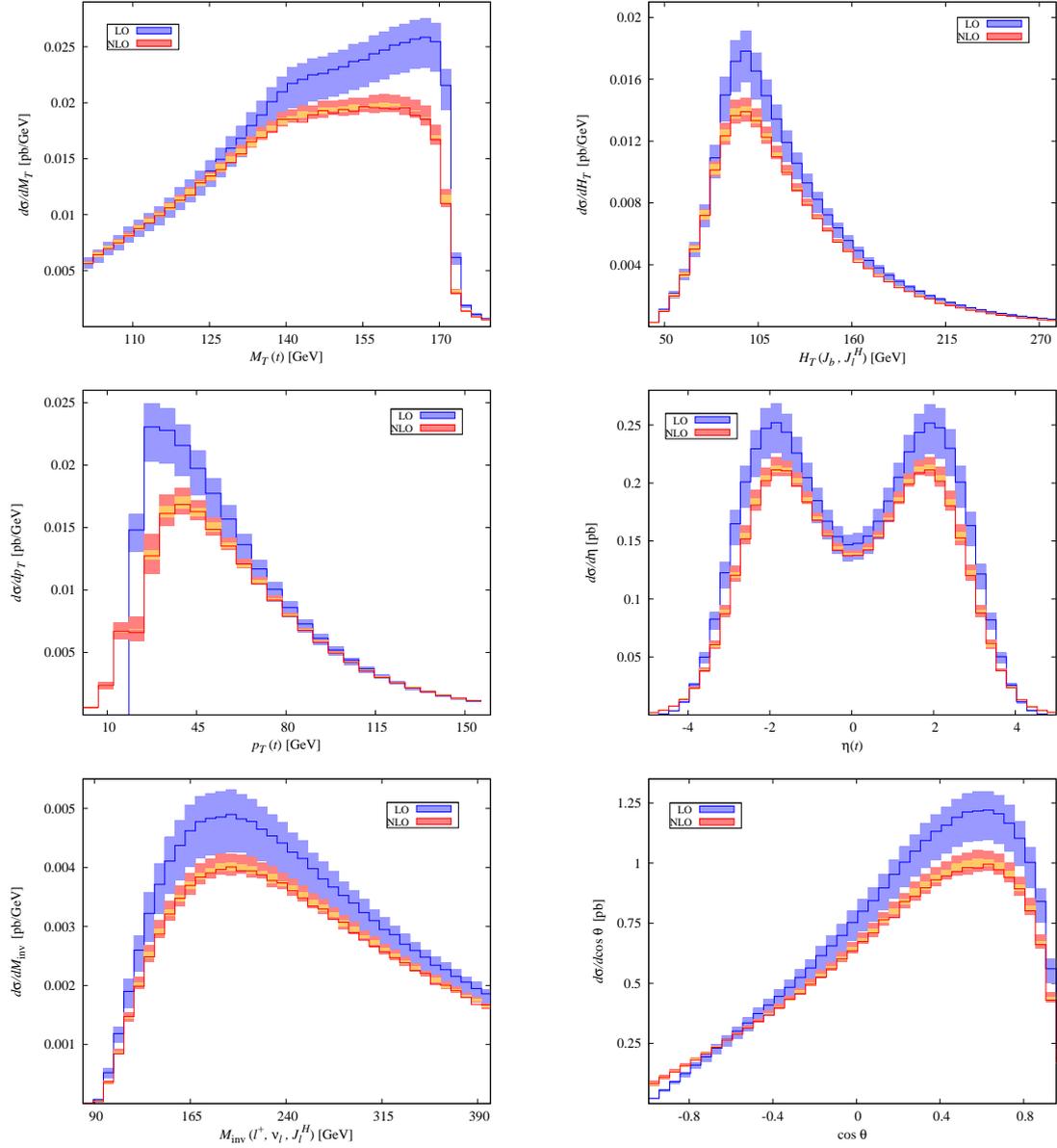
Figure 6.15: A selection of kinematic distributions for $pp \rightarrow J_b J_l l^+ \not{E}_T + X$ at the 7 TeV LHC, using the parameters and cuts given in Table 6.8. Top: top-quark transverse-mass (left) and transverse hadronic-energy (right). Centre: top-quark transverse-momentum (left) and pseudorapidity (right). Bottom: $l^+ \nu_l J_l^H$ invariant-mass (left) and $\cos \theta$ (right). The plots show the differential cross section at LO (blue) and NLO (red). See text for more details.

using a different set of cuts, given in Table 6.8, for t-channel production at the 7 TeV LHC with no veto on a $\bar{b}$-jet. That is, we include all partonic processes shown in Eqs. (6.1)-(6.4). The LO results were also calculated using LO PDFs, in accordance with the literature. Distributions for the observables defined in Eqs. (6.11)-(6.16) are shown in Figure 6.15. As before, the LO and NLO results are shown as the blue and red bands respectively, with the bands obtained by varying the renormalisation and factorisation scales in the range $m_t/4 \leq (\mu_R = \mu_F) \leq m_t$. The orange band comes from varying the factorisation scale only, leaving $\mu_R = m_t/2$. The values obtained using the central scale are shown as solid blue and red lines. It is clear to see, by comparison with the plots shown in Figure 6.12, that removing the $\bar{b}$-jet veto leads to a reduction in the size of the NLO corrections. These smaller corrections are in much better agreement with the results found in the literature.

The major contributor to the correlation between the $\bar{b}$-jet veto and the size of the NLO corrections is the $qg \to q'bl^+\nu_l\bar{b}$ partonic process. As we saw in the previous sections, for the single b-jet process with a $\bar{b}$-jet veto, the $qg \to q'bl^+\nu_l\bar{b}$ partonic process provides a large, negative contribution to the NLO corrections. This can be seen by comparing the black and red lines in the plots of Figure 6.12. For the double b-jet process, which requires a detected $\bar{b}$-jet, the $qg \to q'bl^+\nu_l\bar{b}$ partonic process provides a large, positive contribution to the NLO corrections. This can be seen by comparing the black and red lines in the plots of Figure 6.13. By removing the veto, we include all possible kinematics of the $\bar{b}$-jet. That is, its contribution when the jet is very forward and remains undetected (the same contribution we include when we have the veto in the single b-jet case) and its contribution when the jet has larger transverse-momentum and is detected (the same contribution we include when we require a detected $\bar{b}$-jet in the double b-jet case). The inclusion of both of these kinematic regions leads to a cancellation between the large, positive effects of the detected jet and the large,

negative effects of the undetected jet, resulting in a smaller overall contribution. It is this reduction in the size of the contributions from the $qg \rightarrow q'bl^+\nu\bar{b}$ partonic process that is mainly responsible for the overall reduction in the size of the NLO corrections as we move from having a strong veto on a $\bar{b}$-jet to no veto at all.

Chapter 7

Conclusions and Outlook

In this chapter, the work presented in this thesis is summarised and conclusions are drawn. The chapter closes with a brief outlook on future applications of the method and possible improvements that could be made.

7.1 Summary and Conclusions

In this thesis, a general method for calculating processes involving an intermediate heavy-particle has been presented. The method allows for the inclusion of off-shell effects, including the non-factorisable next-to-leading order contributions which link the production and decay subprocesses. The inclusion of these effects extends our results beyond those of the improved narrow-width approximation. The method involves simultaneously applying a standard perturbative expansion in the electroweak and strong couplings along with an expansion in the virtuality of the heavy particle. This calculation was carried out, along with calculations using both the standard and

improved narrow-width approximations, for s- and t-channel single-top production at the Tevatron and the LHC.

Performing the calculation in three ways offered the chance to explore the changing complexity of the calculation as the treatment of the top quark was changed. While the amplitudes in the NWA have a simpler structure than in the iNWA and off-shell cases, due to the separate treatment of the production and decay subprocesses, the calculation is hindered by the presence of the massive top-quark as an external particle. When dealing with the real corrections, we are forced to use massive dipoles which, in general, have a far more complicated structure than their massless counterparts. Therefore, whilst the structure of the amplitudes may be more complicated in the off-shell treatment, the presence of only massless external particles reduces the complexity of the dipoles. If we require spin-correlation information, calculating with the off-shell treatment is actually simpler than calculating using the iNWA treatment, due to this change from massive to massless dipoles.

Having the results calculated using the three heavy-particle treatments also allowed the size of the off-shell and spin-correlation effects to be investigated. In general, the off-shell effects were small ($\sim$ 1-3% of the full NLO result) for cross sections and observables which were inclusive enough in the top-quark invariant-mass. However, in the top-quark invariant-mass distributions, and at kinematic edges of certain other distributions, their effect can be more substantial. The changes in the top-quark invariant-mass distributions, brought about by the inclusion of the off-shell effects, could have an impact on precise measurements of the top-quark mass. Spin-correlation effects were also found to be small for most distributions. They can become much larger at the edge of certain distributions, however. In distributions which measure the angle between particles produced in the production and decay subprocesses, the spin-correlation ef-

fects can be huge, as we would expect. In these cases, the shape of the distributions in the spin-correlated and non-spin-correlated cases are qualitatively different.

The success of our method is very dependent on the effectiveness of our δ-expansion. Of particular importance, in this regard, is the virtuality of the top quark. To ensure that this scales as expected in our δ-counting, we would have to impose a very tight cut on the top-quark invariant-mass. Imposing such a tight cut, however, leads to a substantial loss of cross section and would not generally be used in experiment. In light of this, we impose a looser cut with the expectation that our neglected contributions may be larger than we originally hoped. When we compare the size of our NLO contribution to the contribution of the first neglected tree-level diagrams, the QCD-mediated diagrams, we see that the suppression is generally good in most distributions. In those distributions where the suppression is less effective, however, the overall shape of the two distributions tends to be different and thus, the two effects can be disentangled. The suppression of the QCD-mediated diagrams appears to be stronger at the LHC than at the Tevatron.

Finally, we have seen that at NLO it is no longer instructive to consider s- and t-channel production. The presence of diagrams in both production channels that lead to identical final states makes distinguishing them impossible experimentally. Instead, we can separate the results into those containing a single b-jet in the final state, which correspond to t-channel production at tree level, and those containing two b-jets in the final state, which correspond to s-channel production at tree level. Even with this separation, it is important to include all diagrams which can contribute, as it is possible for their effects to be large, even if cuts designed to suppress the contribution have been applied. A good example of this is the $qg \to q'bl^+\nu\bar{b}$ partonic process. This process contains two b-jets in its final state. However, should the $\bar{b}$-jet remain undetected, it

appears to contain only a final-state b-jet and may need to be included in the single b-jet process. In this case, its contribution to the total cross section can be very large.

The calculation presented in this thesis has shown that our method can be applied to processes containing an unstable heavy-particle in a relatively straightforward way. Although the off-shell effects are generally small, there are regions in which they become numerically important. Their inclusion is therefore desirable in calculations which require high precision, such as the determination of heavy-particle masses.

7.2 Outlook

Future research involving the method outlined in this thesis lies in two main areas; the improvement of the accuracy of the calculation and the application of the method to other processes of interest.

The most straightforward way to improve the accuracy of the calculation would be to include higher orders in δ. The obvious step would be to include the next term in the δ-expansion. This includes two-loop processes, however, which leads to greatly increased complexity in the calculation of the amplitudes. An alternative to this would be to redefine the scaling of the resonant top-quark propagator from $\sim \delta^{-1}$ to $\sim \delta^{-1/2}$. This would cover the large top-quark invariant-mass window we currently use. The calculation would then include both the resonant and QCD-mediated tree-level diagrams at leading order, with the $\mathcal{O}(\alpha_s)$ corrections to each, plus the tree-level electroweak-resonant interference diagrams, making up the NLO corrections. This would increase the accuracy of the calculation while avoiding the added complexity of two-loop diagrams.

Another method of increasing the accuracy of the calculation would be to introduce different scales for the hard and soft regions. This is typical in a strict effective-theory. The two scales are then evolved to a common scale via renormalisation-group equations. The introduction of these two separate scales generally improves the scale dependence of the cross section, but should also lead to a more accurate description of the off-shell effects. As we currently use only a single, hard scale, soft contributions are evaluated with the strong coupling constant defined at this hard scale. By introducing a soft scale, that is much smaller than the hard scale, the strong coupling constant used to evaluate the soft corrections becomes substantially larger. This could, in turn, increase the size of the off-shell effects. In order to achieve this, the real contributions also have to be split into hard and soft contributions. This separation is not straightforward, however, and would need to be investigated further.

As the method presented in this thesis is very general, its application to other processes containing unstable heavy-particles is straightforward. One candidate processes would be the associated-tW channel of single-top production. This would, in combination with the results presented in this thesis, give a full description of single-top production at the Tevatron and the LHC. Another interesting process would be top-pair production. This process will be studied extensively at the LHC in order to make precise measurements of the various properties of the top quark. Therefore, an understanding of the off-shell effects present within it would be desirable.

Appendix A

Renormalisation and Resummation of the Top-Quark Propagator

In this appendix, the renormalisation and resummation of the top-quark propagator will be discussed, in detail, for a general, real renormalisation scheme. It will then be shown how, by electing to use the on-shell renormalisation scheme, the final expressions can be simplified.

As seen in Figure 2.1, the Feynman rule for a top-quark propagator is

$$\frac{i(\slashed{p}_t + m_t)}{p_t^2 - m_t^2} = \frac{i}{\slashed{p}_t - m_t} \, , \tag{A.1}$$

where the presence of the $i0^+$ factor in the denominator is understood. It is clear to see that we have a pole when $p_t^2 = m_t^2$. This is due to a breakdown of strict fixed-order perturbation theory as the intermediate top-quark approaches its mass shell. Subleading corrections to the propagator become enhanced as the denominator becomes small. To counter this problem, these corrections must be resummed to all

orders. To do this, we replace

$$\frac{i}{\not{p}_t - m_t} \rightarrow \frac{i}{\not{p}_t - m_t} \sum_{n=0}^{\infty} \left[\frac{\bar{\Sigma}_t(\not{p}_t)}{\not{p}_t - m_t} \right]^n = \frac{i}{\not{p}_t - m_t - \bar{\Sigma}_t(\not{p}_t)}, \qquad \text{(A.2)}$$

where $\bar{\Sigma}_t(\not{p}_t)$ is the sum of renormalised one-particle irreducible corrections to the top-quark two-point function. This shifts the pole of the propagator to a new location, μ_t. This is defined as the solution to the equation $\bar{\Gamma}_t(\mu_t) = 0$, where

$$\bar{\Gamma}_t(\not{p}_t) = \not{p}_t - m_t - \bar{\Sigma}_t(\not{p}_t) \qquad \text{(A.3)}$$

is the denominator of the modified top-quark propagator. As our calculation requires the production of a single top-quark via weak interactions, we need only consider the left-handed top-quark propagator. Replacing the bare parameters in Eq. (A.3) with renormalised parameters, denoted by a superscript r, we obtain

$$\bar{\Gamma}_t^L(\not{p}_t) = \not{p}_t \left(1 + \delta Z_t^{L,r} \right) - m_t^r - \delta m_t^r - \frac{m_t^r}{2} \left(\delta Z_t^{L,r} + \left(\delta Z_t^{R,r} \right)^\dagger \right) - \bar{\Sigma}_t^L(\not{p}_t), \qquad \text{(A.4)}$$

for the denominator of the left-handed propagator. Here, the superscripts L and R denote left- and right-handed contributions respectively. The pole of the propagator is found by solving $\bar{\Gamma}_t^L(\mu_t) = 0$. The general solution to this equation has the form $\mu_t = m_t - i\Gamma_t/2$, where m_t is the pole mass and Γ_t is the decay width. Both of these parameters are real and thus,

$$m_t = \text{Re} \left[\mu_t \right], \qquad \qquad \Gamma_t = -2 \, \text{Im} \left[\mu_t \right]. \qquad \text{(A.5)}$$

The residue of the propagator at the complex pole, μ_t, is defined by

$$(1 + \delta R_t^r) = \left(\frac{\partial \bar{\Gamma}_t^L}{\partial \not{p}_t}(\mu_t) \right)^{-1} = \left(1 + \delta Z_t^{L,r} - \frac{\partial \bar{\Sigma}_t^L}{\partial \not{p}_t}(\mu_t) \right)^{-1} . \qquad (A.6)$$

To complete our calculation to the desired accuracy, we must expand the denominator in Eq. (A.4), to $\mathcal{O}(\delta)$ in our counting, and solve for μ_t. As $\alpha_s \sim \delta^{1/2}$ and $\alpha_{ew} \sim \delta$, this means including corrections up to $\mathcal{O}(\alpha_s^2)$ in the strong coupling and to $\mathcal{O}(\alpha_{ew})$ in the electroweak coupling. Higher order corrections contribute to the amplitude perturbatively and need not be resummed. We expand the expressions for the wavefunction and mass renormalisation parameters, and for $\bar{\Sigma}_t^L(\mu_t)$, in the following way:

$$\delta m_t^r = \alpha_s \delta m_{(0,1)}^r + \alpha_s^2 \delta m_{(0,2)}^r + \alpha_{ew} \delta m_{(1,0)}^r , \qquad (A.7)$$

$$\delta Z_t^{L/R,r} = \alpha_s \delta Z_{(0,1)}^r + \alpha_s^2 \delta Z_{(0,2)}^r + \alpha_{ew} \delta Z_{(1,0)}^{L/R,r} , \qquad (A.8)$$

$$\bar{\Sigma}_t^L(\mu_t) = \alpha_s \Sigma_{(0,1)}(\mu_t) + \alpha_s^2 \Sigma_{(0,2)}(\mu_t) + \alpha_{ew} \Sigma_{(1,0)}^L(\mu_t) , \qquad (A.9)$$

where the subscript (m, n) denotes that the parameter corresponds to the expansion to order $\alpha_{ew}^m \alpha_s^n$. Note that the QCD parts of the expansion of these parameters do not depend on the helicity of the top quark. By using a real renormalisation scheme, we ensure that the wavefunction and mass renormalisation parameters, and thus the parameters in their expansions, are purely real. The QCD self-energy contributions, $\Sigma_{(0,1)}$ and $\Sigma_{(0,2)}$, are also real. Setting $\bar{\Gamma}_t^L(\mu_t) = 0$ and substituting these expansions into Eq. (A.4), we obtain two separate equations; one for the real part of μ_t and one

for the imaginary part of μ_t. From these, we obtain

$$
\begin{aligned}
m_t \;=\;& m_t^r - \alpha_s \left(\delta m_{(0,1)}^r + \Sigma_{(0,1)}(m_t^r) \right) \\
& - \alpha_s^2 \left[\delta m_{(0,2)}^r + \Sigma_{(0,2)}(m_t^r) + \delta Z_{(0,2)}^r \left(\delta m_{(0,1)}^r + \Sigma_{(0,1)}(m_t^r) \right) \right] \\
& - \alpha_{ew} \left(\delta m_{(1,0)}^r + \frac{m_t^r}{2} \left(\delta Z_{(1,0)}^{R,r} - \delta Z_{(1,0)}^{L,r} \right) + \mathrm{Re}\left[\Sigma_{(1,0)}^L(m_t^r) \right] \right) , \quad \text{(A.10)}
\end{aligned}
$$

$$
\Gamma_t \;=\; -2\alpha_{ew} \,\mathrm{Im}\left[\Sigma_{(1,0)}^L(m_t^r) \right] . \tag{A.11}
$$

These expressions define our μ_t value and, hence, our resummation. We include this resummation in our amplitudes by making the replacement $(p_t^2 - m_t^2) \to (p_t^2 - \mu_t^2)$ in the denominator of the resonant top-quark propagator.

Using the same expansion, the residue has the form

$$
\begin{aligned}
(1 + \delta R_t^r) &= \left(1 + \alpha_s \left(\delta Z_{(0,1)}^r - \frac{\partial \Sigma_{(0,1)}}{\partial \slashed{p}_t}(\mu_t) \right) + \mathcal{O}(\alpha_s^2, \alpha_{ew}) \right)^{-1} \\
&= 1 + \alpha_s \left(\frac{\partial \Sigma_{(0,1)}}{\partial \slashed{p}_t}(\mu_t) - \delta Z_{(0,1)}^r \right) + \mathcal{O}(\alpha_s^2, \alpha_{ew}) ,
\end{aligned} \tag{A.12}
$$

and hence, $\delta R_t^r \sim \alpha_s$.

In the on-shell renormalisation scheme, the counterterms satisfy the following conditions:

$$
\delta m_{(0,1)}^{\mathrm{OS}} = -\Sigma_{(0,1)}(m_t^{\mathrm{OS}}) , \tag{A.13}
$$

$$
\delta m_{(0,2)}^{\mathrm{OS}} = -\Sigma_{(0,2)}(m_t^{\mathrm{OS}}) , \tag{A.14}
$$

$$
\delta m_{(1,0)}^{\mathrm{OS}} + \frac{m_t^{\mathrm{OS}}}{2} \left(\delta Z_{(1,0)}^{R,\mathrm{OS}} - \delta Z_{(1,0)}^{L,\mathrm{OS}} \right) = -\mathrm{Re}\left[\Sigma_{(1,0)}^L(m_t^{\mathrm{OS}}) \right] . \tag{A.15}
$$
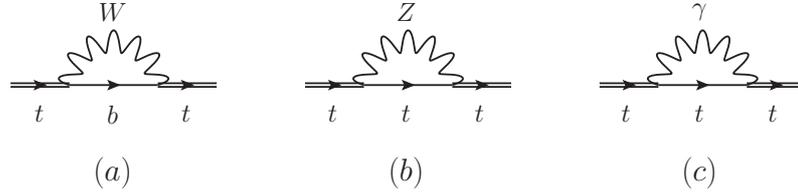
Figure A.1: The Feynman diagrams contributing to the top-quark self-energy at $\mathcal{O}(\alpha_{ew})$.

This simplifies Eqs. (A.10) and (A.11) to

$$m_t = m_t^{\text{OS}} , \tag{A.16}$$

$$\Gamma_t = -2\alpha_{ew} \, \text{Im} \left[\Sigma_{(1,0)}^L (m_t^{\text{OS}}) \right] . \tag{A.17}$$

As we can see, the dependence on the QCD top-quark self-energy diagrams is totally cancelled out by the top-quark mass counterterms. The only remaining dependence is on the imaginary part of the electroweak self-energy diagrams. The electroweak self-energy diagrams at order α_{ew} are shown in Figure A.1. The Feynman diagrams containing a Z-boson and a photon, shown in diagrams (b) and (c) of the figure, do not have an imaginary component. Therefore, the only diagram which is resummed is the electroweak self-energy diagram containing a W-boson in the loop, shown as diagram (a) in Figure A.1.

The scaling of the residue is also altered. Using the fact that, in the on-shell scheme,

$$\delta Z_t^{L,\text{OS}} = \text{Re} \left[\frac{\partial \bar{\Sigma}_t^L}{\partial \slashed{p}_t} (m_t^{\text{OS}}) \right] , \tag{A.18}$$

we get a cancellation of the $\mathcal{O}(\alpha_s)$ components in Eq. (A.12) and are left with $\delta R_t^{\text{OS}} \sim \alpha_{ew}$.

We have seen, above, how the choice of renormalisation scheme can affect the definition of the complex pole, μ_t, and its residue, $(1 + \delta R_t)$. These, in turn, can affect

the implementation of our δ-counting. Firstly, in the on-shell scheme we have the residue factor, $\delta R_t^{\text{OS}} \sim \alpha_{ew} \sim \delta$, which makes its contribution to Eq. (4.7) beyond our target accuracy. However, in a generic renormalisation scheme, $\delta R_t^r \sim \alpha_s \sim \delta^{1/2}$, and its contribution would need to be included in our calculation. More importantly, however, throughout this thesis it has been assumed that both $D_t = p_t^2 - (m_t^r)^2 \sim m_t^2 \delta$ and $\Delta_t = p_t^2 - \mu_t^2 \sim m_t^2 \delta$. In the on-shell scheme this is consistent as $\mu_t^2 - (m_t^{\text{OS}})^2 = \mu_t^2 - m_t^2 \sim m_t \Gamma_t \sim m_t^2 \delta$. However, in a general scheme $\mu_t^2 - (m_t^r)^2 \sim \alpha_s m_t^2 \sim m_t^2 \delta^{1/2}$, and the two conditions are incompatible. Therefore, while any renormalisation scheme could be chosen, for our δ-counting to work correctly we must select a scheme in which $\mu_t^2 - (m_t^r)^2 \sim m_t^2 \delta$. The on-shell renormalisation scheme is an example of such a scheme and is the one we choose to use throughout.

Appendix B

Jet Algorithm

The jet algorithm used to obtain all results in Chapters 5 and 6 is outlined below.

For each final-state parton, i, we define a distance measure between it and the beam axis,

$$d_i = p_T^2(i) = \vec{p}_\perp^2(i) \,.$$

We also define a distance measure between two partons, i and j,

$$d_{ij} = \min(d_i, d_j) \frac{\Delta_{ij}^2}{D_{\mathrm{res}}^2} \,,$$

where D_{res} is the arbitrary jet-resolution parameter and

$$\Delta_{ij}^2 = (y(i) - y(j))^2 + (\phi(i) - \phi(j))^2 \,,$$

with y and ϕ the rapidity and azimuthal angle of the partons respectively,

$$y(i) = \frac{1}{2} \ln \left(\frac{E(i) + |\vec{p}_{\parallel}(i)|}{E(i) - |\vec{p}_{\parallel}(i)|} \right) \, , \tag{B.4}$$

$$\tag{B.5}$$

$$\tan (\phi(i)) = \frac{\vec{p}_{\perp_2}(i)}{\vec{p}_{\perp_1}(i)} \, , \tag{B.6}$$

where $\vec{p}_{\perp_1}$ and $\vec{p}_{\perp_2}$ are the components of 3-momentum which are perpendicular to one another and the beam axis. We then look for the smallest of all the d_i and d_{ij} values. If the smallest value belongs to one of the d_i, we call parton i a jet, remove it from the list and start over. If the smallest value belongs to one of the d_{ij}, however, we combine partons i and j into a proto-jet, K, with momentum $p(K) = p(i) + p(j)$ and start over, calculating d_K and d_{iK} as if the proto-jet were a final-state parton. This process continues until all final-state partons have been incorporated into jets.

With the definition of our single b- and double b-jet processes in Chapter 6, problems could arise if a final-state b-quark and $\bar{b}$-quark combined to create a single jet. To avoid this potential issue, if the two combine we create a single 'fat' jet which corresponds to neither a b or $\bar{b}$-jet. Hence, the event will not satisfy the cuts of either process (one requiring a detected b-jet, the other a detected $\bar{b}$-jet) and will be ignored. This 'fat'-jet veto should be compatible with experiment where a jet containing two b-quarks should be distinguishable from jets originating from a single b-quark.

Appendix C

Amplitudes

In this appendix, the various amplitudes required for the calculation of the cross section of t-channel single-top production to NLO in our counting are presented. The amplitudes for s-channel single-top production can be obtained from these via the crossing of momenta. The t-channel partonic process, at tree level, is

$$q(p_1)\, b(p_2) \to q'(p_3)\, b(p_4)\, W^+(p_W) \to q'(p_3)\, b(p_4)\, l^+(p_5)\, \nu_l(p_6)\,, \tag{C.1}$$

and we define

$$s_{ij} = (p_i + p_j)^2\,, \qquad D_t = p_t^2 - m_t^2\,,$$
$$p_t = p_4 + p_5 + p_6\,, \qquad \Delta_t = p_t^2 - \mu_t^2\,. \tag{C.2}$$

Amplitudes are expressed using the helicity notation, introduced in Section 3.5. The overall factor $g_{ew}\sqrt{1/(2\Gamma_W M_W)}$, that appears in the amplitudes, comes from the inclusion of the W-boson decay using the improved narrow-width approximation, as discussed in Section 5.2.
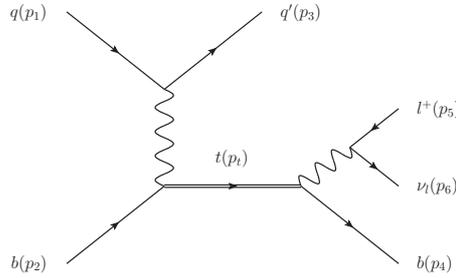
Figure C.1: The only tree-level Feynman diagram contributing to the LO cross section of the hard-scattering process in Eq. (C.1) to $\mathcal{O}(\delta)$.

C.1 Tree-Level Amplitude

At tree level we require only the amplitude of the resonant diagram, shown in Figure C.1. The squared matrix-element of this diagram is given by

$$\mathcal{M}^{\text{tree}} = g_{ew}^6 \left| A_{(-1)}^{(3,0)} \right|^2 + \mathcal{O}(\delta^2) \,, \tag{C.3}$$

where

$$A_{(-1)}^{(3,0)} = g_{ew} \sqrt{\frac{1}{2 M_W \Gamma_W}} \frac{[12]\langle 46 \rangle \langle 3|4+6|5]}{\left(s_{13} + M_W^2 \right) \Delta_t} \,. \tag{C.4}$$

It should be noted that the above amplitude is correct only if the initial-state q is a quark. If q represents an anti-quark, the relevant amplitude is obtained by crossing the momenta $p_1 \leftrightarrow -p_3$ in Eq. (C.4). This momentum crossing can also be applied to the one-loop and real amplitudes.
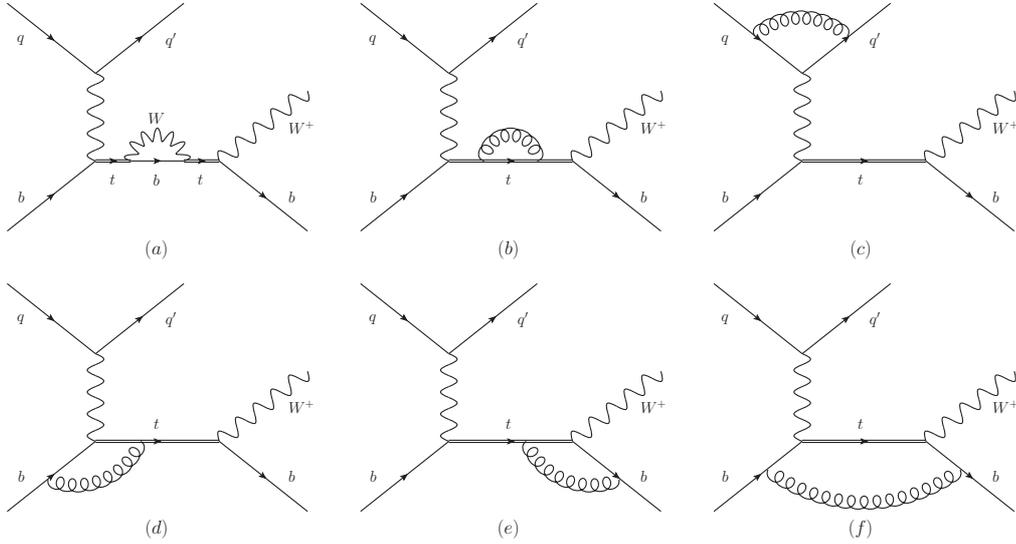
Figure C.2: The one-loop Feynman diagrams required to calculate the NLO cross section of the hard-scattering process in Eq. (C.1) to $\mathcal{O}(\delta^{3/2})$.

C.2 One-Loop Amplitudes

At one-loop, the squared matrix-element is given by

$$\mathcal{M}^{\text{Virtual}} = g_{ew}^6 g_s^2 \, 2 \, \text{Re} \left[A_{(-1)}^{(3,2)} \left(A_{(-1)}^{(3,0)} \right)^* \right] + \mathcal{O}(\delta^2) \,, \tag{C.5}$$

with the diagrams contributing to $A_{(-1)}^{(3,2)}$ shown in diagrams (b)-(f) of Figure C.2. These diagrams are split into soft and hard contributions, as explained in Section 5.3. The soft contributions factorise according to

$$A_{(-1),i}^{(3,2),S} = \delta V_i^S A_{(-1)}^{(3,0)} \,, \tag{C.6}$$

where $A_{(-1)}^{(3,0)}$ is the tree-level amplitude, given in Eq. (C.4), and δV_i^S are the soft factors corresponding to diagram (i) of Figure C.2. These are given by

$$
\begin{aligned}
\delta V_b^S &= -4iC_F\tilde{\mu}^{2\epsilon}\frac{m_t^2}{\Delta_t}\int\frac{d^dk}{(2\pi)^d}\frac{1}{k^2}\frac{1}{\Delta_t - 2p_t\cdot k}\\
&= \frac{C_F}{8\pi^2}\left[\frac{1}{\epsilon}+2\right]\left(-\frac{\Delta_t}{\mu m_t}\right)^{-2\epsilon},
\end{aligned}
\tag{C.7}
$$

$$
\begin{aligned}
\delta V_c^S &= -4iC_F\tilde{\mu}^{2\epsilon}(p_1\cdot p_3)\int\frac{d^dk}{(2\pi)^d}\frac{1}{k^2}\frac{1}{(-2p_1\cdot k)}\frac{1}{(-2p_3\cdot k)}\\
&= 0,
\end{aligned}
\tag{C.8}
$$

$$
\begin{aligned}
\delta V_d^S &= -4iC_F\tilde{\mu}^{2\epsilon}(p_2\cdot p_t)\int\frac{d^dk}{(2\pi)^d}\frac{1}{k^2}\frac{1}{(-2p_2\cdot k)}\frac{1}{\Delta_t - 2p_t\cdot k}\\
&= \frac{C_F}{8\pi^2}\left[\frac{1}{2\epsilon^2}+\frac{5}{24}\pi^2\right]\left(-\frac{\Delta_t}{\mu m_t}\right)^{-2\epsilon},
\end{aligned}
\tag{C.9}
$$

$$
\begin{aligned}
\delta V_e^S &= -4iC_F\tilde{\mu}^{2\epsilon}(p_4\cdot p_t)\int\frac{d^dk}{(2\pi)^d}\frac{1}{k^2}\frac{1}{(-2p_4\cdot k)}\frac{1}{\Delta_t - 2p_t\cdot k}\\
&= \frac{C_F}{8\pi^2}\left[\frac{1}{2\epsilon^2}+\frac{5}{24}\pi^2\right]\left(-\frac{\Delta_t}{\mu m_t}\right)^{-2\epsilon},
\end{aligned}
\tag{C.10}
$$

$$
\begin{aligned}
\delta V_f^S &= -4iC_F\tilde{\mu}^{2\epsilon}(p_2\cdot p_4)\int\frac{d^dk}{(2\pi)^d}\frac{1}{k^2}\frac{1}{(-2p_2\cdot k)}\frac{1}{(-2p_4\cdot k)}\frac{\Delta_t}{\Delta_t - 2p_t\cdot k}\\
&= \frac{C_F}{8\pi^2}\left[-\frac{1}{\epsilon^2}-\frac{1}{\epsilon}\ln\left(\frac{(s_{2t}-m_t^2)(s_{4t}-m_t^2)}{m_t^2 s_{24}}\right)\right.\\
&\quad\left.+\mathrm{Li}_2\left(1-\frac{(s_{2t}-m_t^2)(s_{4t}-m_t^2)}{m_t^2 s_{24}}\right)-\frac{5}{12}\pi^2\right]\left(-\frac{\Delta_t}{\mu m_t}\right)^{-2\epsilon}.
\end{aligned}
\tag{C.11}
$$

Here, the prefactor $\tilde{\mu}^{2\epsilon} = \mu^{2\epsilon}e^{\epsilon\gamma_E}(4\pi)^{-\epsilon}$ is introduced to simplify the subtraction scheme. When this factor is combined with the $\bar{\epsilon}$-poles, which arise in the loop integrals, we are left only with ϵ-poles and the renormalisation scale, μ. The $\overline{\mathrm{MS}}$ subtraction scheme is then equivalent to removing the ϵ-poles only. This is explained in Section 5.3.

The soft contribution to diagram (a) scales as $\sim \delta^{3/2}$ and is beyond the accuracy we are aiming for. Summing these contributions gives a total soft contribution,

$$
\begin{aligned}
\delta V^S = \frac{C_F}{8\pi^2} \left(-\frac{\Delta_t}{\mu m_t} \right)^{-2\epsilon} \Bigg[& \frac{1}{\epsilon} \left(1 - \ln \left(\frac{(s_{2t} - m_t^2)(s_{4t} - m_t^2)}{m_t^2 s_{24}} \right) \right) \\
& + 2 + \text{Li}_2 \left(1 - \frac{(s_{2t} - m_t^2)(s_{4t} - m_t^2)}{m_t^2 s_{24}} \right) \Bigg] .
\end{aligned}
\tag{C.12}
$$

The hard contributions of the one-loop amplitudes can be written in the form

$$
A^{(3,2),H}_{(-1),i} = \delta V_i^H A^{(3,0)}_{(-1)} + \delta A_i^H , \tag{C.13}
$$

where $A^{(3,0)}_{(-1)}$ is the tree-level amplitude, δV_i^H are the hard factors, corresponding to diagram (i) of the figure, that multiply the tree-level amplitude and δA_i^H are finite factors that have a different Lorentz structure. The hard part of diagram (b) contains 'superleading' contributions which are exactly cancelled by the counterterms (ct), as described in Section 5.4. It is instructive, therefore, to group these contributions together, rather than keeping them separate. The hard part of diagram (a) is taken care of via the resummation of the top-quark propagator, described in Section 4.2 and Appendix A, and does not require a separate expression for its amplitude. The hard part of diagram (f) scales as $\sim \delta^2$ and is beyond the target accuracy of our calculation.

The finite factors are:

$$\delta A_{b+ct}^{H} = 0 \,, \tag{C.14}$$

$$\delta A_{c}^{H} = 0 \,, \tag{C.15}$$

$$\delta A_{d}^{H} = g_{ew} \sqrt{\frac{1}{2M_W \Gamma_W}} \frac{C_F}{16\pi^2} \frac{[52]\langle 46\rangle \langle 3|2|1]}{(s_{13} + M_W^2)\Delta_t} \frac{m_t^2}{2m_t^2 - s_{2t}} \ln\left(\frac{s_{2t} - m_t^2}{m_t^2}\right) \,, \tag{C.16}$$

$$\delta A_{e}^{H} = g_{ew} \sqrt{\frac{1}{2M_W \Gamma_W}} \frac{C_F}{16\pi^2} \frac{[12]\langle 43\rangle \langle 6|4|5]}{(s_{13} + M_W^2)\Delta_t} \frac{m_t^2}{2m_t^2 - s_{4t}} \ln\left(\frac{s_{4t} - m_t^2}{m_t^2}\right) \,, \tag{C.17}$$

$$\delta A_{f}^{H} = 0 \,. \tag{C.18}$$

The hard factors, δV^H, are general for the off-shell treatment and the various on-shell treatments of the heavy top-quark. Therefore, rather than writing them with a subscript corresponding to the off-shell diagrams in Figure C.2, a more general labelling is used. For the combination of the QCD top-quark self-energy diagram (b) and the counterterms, we use the label $se + ct$; for the upper quark line diagram with a gluon attached to the legs with momenta p_1 and p_3 (diagram (c)), we use the label [31]; for the lower quark line diagram with the gluon attached to the legs with momenta p_2 and p_t (diagram (d)), we use the label [2t]; for the lower quark line diagram with the gluon attached to the legs with momenta p_4 and p_t (diagram (e)), we use the label [4t]; and finally, for the non-factorisable lower quark line diagram with the gluon attached to

the legs with momenta p_2 and p_4 (diagram (f)), we use the label nf. Then,

$$\delta V^H_{b+ct} = \delta V^H_{se+ct} = \frac{C_F}{8\pi^2}\left[-\frac{3}{2\epsilon} + \frac{3}{2}\ln\left(\frac{m_t^2}{\mu^2}\right) - 2 - \frac{x_{sc}}{2}\right],\tag{C.19}$$

$$\delta V^H_c = \delta V^H_{[31]} = \frac{C_F}{8\pi^2}\left[-\frac{1}{\epsilon^2} + \frac{1}{\epsilon}\left(\ln\left(\frac{s_{13}}{\mu^2}\right) - \frac{3}{2}\right) - \frac{1}{2}\ln^2\left(\frac{s_{13}}{\mu^2}\right)\right.$$
$$\left. + \frac{3}{2}\ln\left(\frac{s_{13}}{\mu^2}\right) - 4 + \frac{x_{sc}}{2} + \frac{\pi^2}{12}\right],\tag{C.20}$$

$$\delta V^H_d = \delta V^H_{[2t]} = \frac{C_F}{8\pi^2}\left[-\frac{1}{2\epsilon^2} + \frac{1}{\epsilon}\left(\ln\left(\frac{s_{2t} - m_t^2}{\mu m_t}\right) - \frac{1}{2}\right)\right.$$
$$+ \mathrm{Li}_2\left(1 - \frac{m_t^2}{s_{2t} - m_t^2}\right) - 2 - \frac{\pi^2}{24} - \frac{1}{2}\ln^2\left(\frac{s_{2t} - m_t^2}{\mu m_t}\right)$$
$$+ \ln\left(\frac{s_{2t} - m_t^2}{\mu m_t}\right)\left(1 - \frac{s_{2t} - m_t^2}{2(2m_t^2 - s_{2t})} - \frac{1}{2}\ln\left(\frac{m_t^2}{\mu^2}\right)\right)$$
$$\left. + \frac{1}{8}\ln^2\left(\frac{m_t^2}{\mu^2}\right) + \frac{s_{2t} - m_t^2}{4(2m_t^2 - s_{2t})}\ln\left(\frac{m_t^2}{\mu^2}\right) + \frac{x_{sc}}{2}\right],\tag{C.21}$$

$$\delta V^H_e = \delta V^H_{[4t]} = \delta V^H_{[2t]}\bigg|_{s_{2t} \to s_{4t}},\tag{C.22}$$

$$\delta V^H_f = \delta V^H_{nf} = 0.\tag{C.23}$$

Summing these contributions for the upper and lower quark lines separately, we get

$$\delta V^H_{[31]} = \frac{C_F}{8\pi^2}\left[-\frac{1}{\epsilon^2} + \frac{1}{\epsilon}\left(\ln\left(\frac{s_{13}}{\mu^2}\right) - \frac{3}{2}\right) + \frac{x_{sc}}{2}\right] + \mathcal{O}(1)\tag{C.24}$$

and

$$\delta V^H_{[42]} = \frac{C_F}{8\pi^2}\left[-\frac{1}{\epsilon^2} + \frac{1}{\epsilon}\left(\ln\left(\frac{(s_{2t} - m_t^2)(s_{4t} - m_t^2)}{\mu^2 m_t^2}\right) - \frac{5}{2}\right) + \frac{x_{sc}}{2}\right] + \mathcal{O}(1)\tag{C.25}$$
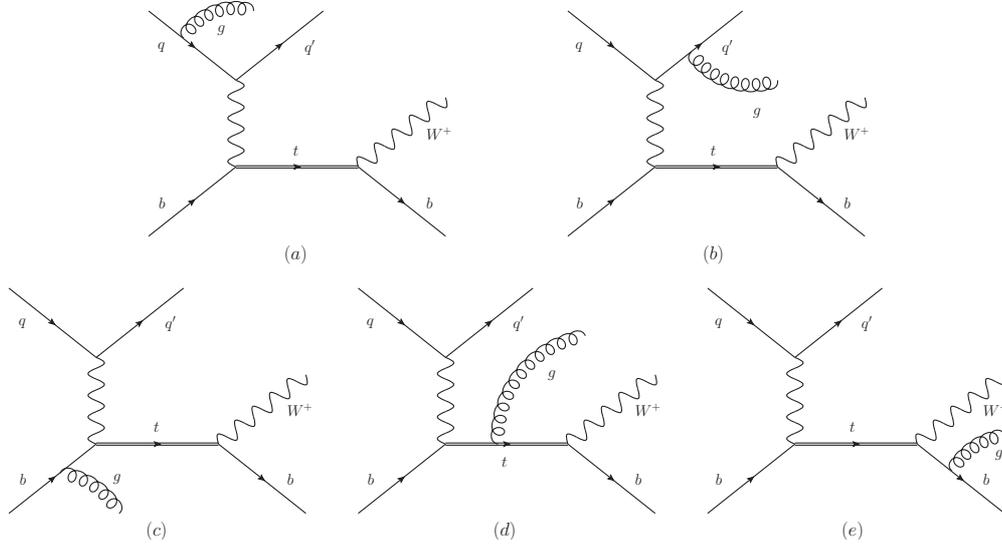
Figure C.3: The real gluon-emission Feynman diagrams, representing the process in
Eq. (C.28), required to calculate the NLO cross section of the hard-scattering
process in Eq. (C.1) to $\mathcal{O}(\delta^{3/2})$.

respectively. Combining these with the soft contributions, the total virtual correction
has the form

$$\delta V_{[31]} = \frac{C_F}{8\pi^2} \left[-\frac{1}{\epsilon^2} + \frac{1}{\epsilon} \left(\ln \left(\frac{s_{13}}{\mu^2} \right) - \frac{3}{2} \right) + \frac{x_{sc}}{2} \right] + \mathcal{O}(1) \qquad \text{(C.26)}$$

for the upper quark line, and

$$\delta V_{[42]} = \frac{C_F}{8\pi^2} \left[-\frac{1}{\epsilon^2} + \frac{1}{\epsilon} \left(\ln \left(\frac{s_{24}}{\mu^2} \right) - \frac{3}{2} \right) + \frac{x_{sc}}{2} \right] + \mathcal{O}(1) \qquad \text{(C.27)}$$

for the lower quark line.
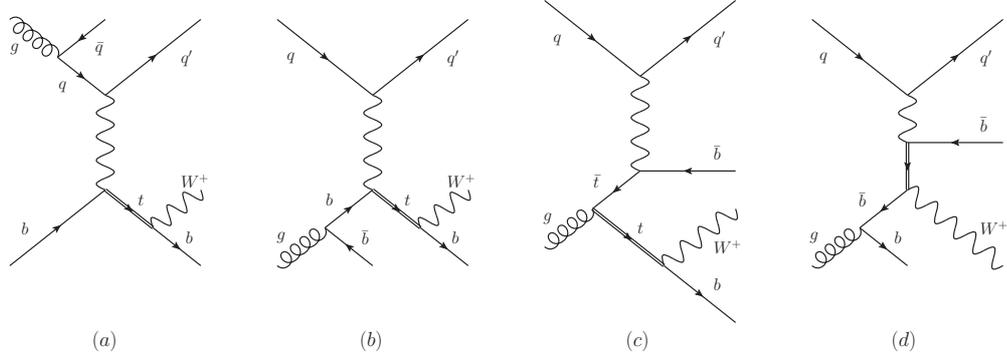
Figure C.4: The gluon-initiated Feynman diagrams, representing the processes in Eqs. (C.29) and (C.30), required to calculate the NLO cross section of the hard-scattering process in Eq. (C.1) to $\mathcal{O}(\delta^{3/2})$.

C.3 Real Amplitudes

For the real corrections we must consider three processes:

$$q(p_1)\, b(p_2) \to q'(p_3)\, b(p_4)\, W^+(p_W)\, g(p_7) \to q'(p_3)\, b(p_4)\, l^+(p_5)\, \nu_l(p_6)\, g(p_7)\,, \quad \text{(C.28)}$$

$$g(p_1)\, b(p_2) \to q'(p_3)\, b(p_4)\, W^+(p_W)\, \bar{q}(p_7) \to q'(p_3)\, b(p_4)\, l^+(p_5)\, \nu_l(p_6)\, \bar{q}(p_7)\,, \quad \text{(C.29)}$$

$$q(p_1)\, g(p_2) \to q'(p_3)\, b(p_4)\, W^+(p_W)\, \bar{b}(p_7) \to q'(p_3)\, b(p_4)\, l^+(p_5)\, \nu_l(p_6)\, \bar{b}(p_7)\,. \quad \text{(C.30)}$$

The real squared matrix-element is given by

$$\mathcal{M}^{\text{Real}} = \left|\mathcal{A}^{\text{Real}}_{qb}\right|^2 + \left|\mathcal{A}^{\text{Real}}_{gb}\right|^2 + \left|\mathcal{A}^{\text{Real}}_{qg}\right|^2\,, \quad \text{(C.31)}$$

where $\mathcal{A}^{\text{Real}}_{qb}$ represents the resonant tree-level diagram (Figure C.1) with an extra emitted gluon, shown in Figure C.3, and $\mathcal{A}^{\text{Real}}_{gb}$ and $\mathcal{A}^{\text{Real}}_{qg}$ represent the gluon-initiated diagrams with the gluon appearing on the upper and lower quark lines, shown in diagram (a) and diagrams (b)-(d) of Figure C.4 respectively. The amplitude for the

gluon-emission diagrams can be written as

$$\mathcal{A}_{qb}^{\text{Real}}(g_7^{\pm}) = \delta_{c_4 c_2} t_{c_3 c_1}^{A_7} g_{ew}^3 g_s A_{(-1),[31]}^{(3,1)}(g_7^{\pm}) + \delta_{c_3 c_1} t_{c_4 c_2}^{A_7} g_{ew}^3 g_s A_{(-1),[42]}^{(3,1)}(g_7^{\pm}), \qquad \text{(C.32)}$$

where c_i is the colour index of external quark i, A_7 is the colour index of the emitted gluon and $g^{\pm}$ denotes the two possible helicity states of the emitted gluon. The amplitudes $A_{(-1),[31]}^{(3,1)}$ and $A_{(-1),[42]}^{(3,1)}$ are the contributions of diagrams with a gluon emitted from the upper quark line (diagrams (a) and (b) in Figure C.3) and lower quark line (diagrams (c)-(e) in Figure C.3) respectively. These are given by

$$A_{(-1),[31]}^{(3,1)}(g_7^+) = g_{ew} \sqrt{\frac{1}{2M_W \Gamma_W}} \frac{\sqrt{2} \langle 46 \rangle \langle 3|4+6|5] \langle 3|7-1|2]}{(s_{137} + M_W^2)\Delta_t \langle 17 \rangle \langle 37 \rangle},$$

$$A_{(-1),[31]}^{(3,1)}(g_7^-) = -g_{ew} \sqrt{\frac{1}{2M_W \Gamma_W}} \frac{\sqrt{2} \langle 46 \rangle [12] [1|3+7|4+6|5]}{(s_{137} + M_W^2)\Delta_t [17][37]}, \qquad \text{(C.33)}$$

where $s_{137} = s_{13} + s_{17} - s_{37}$, and

$$A_{(-1),[42]}^{(3,1)}(g_7^+) = -g_{ew} \sqrt{\frac{1}{2M_W \Gamma_W}} \frac{\sqrt{2}\langle 46 \rangle}{(s_{13} + M_W^2)\Delta_t} \left(\frac{\langle 3|4+6|5]\langle 4|7-2|1]}{\langle 27 \rangle \langle 47 \rangle} \right.$$
$$\left. + \frac{[12]}{\langle 47 \rangle} \frac{\langle 3|1+2|7]\langle 4|6|5] - \mu_t^2 \langle 34 \rangle [57]}{\Delta_{t7}} \right),$$

$$A_{(-1),[42]}^{(3,1)}(g_7^-) = -g_{ew} \sqrt{\frac{1}{2M_W \Gamma_W}} \frac{\sqrt{2} [12]}{(s_{13} + M_W^2)\Delta_{t7}} \left(\frac{\langle 3|1+2|5]\langle 6|4+7|2]}{[27][47]} \right.$$
$$\left. - \frac{\langle 46 \rangle}{[27]} \frac{\langle 3|1|2]\langle 7|4+6|5] + \mu_t^2 \langle 37 \rangle [25]}{\Delta_t} \right), \qquad \text{(C.34)}$$

with $\Delta_{t7} = (p_t + p_7)^2 - \mu_t^2$. The amplitudes for the gluon-initiated diagrams can be written as

$$\mathcal{A}_{gb}^{\text{Real}}(g_1^{\pm}) = \delta_{c_4 c_2} t_{c_3 c_7}^{A_1} g_{ew}^3 g_s A_{(-1),[37]}^{(3,1)}(g_1^{\pm}) , \tag{C.35}$$

$$\mathcal{A}_{qg}^{\text{Real}}(g_2^{\pm}) = \delta_{c_3 c_1} t_{c_4 c_7}^{A_2} g_{ew}^3 g_s A_{(-1),[47]}^{(3,1)}(g_2^{\pm}) . \tag{C.36}$$

Expressions for $A_{(-1),[37]}^{(3,1)}(g_1^{\pm})$ and $A_{(-1),[47]}^{(3,1)}(g_2^{\pm})$ can be obtained by crossing the momenta of Eqs. (C.33) and (C.34) respectively.

Appendix D

Dipole Insertions

In this appendix, the $\boldsymbol{I}$ insertions required for both t-channel and s-channel single-top production using the off-shell and NWA treatments of the intermediate top-quark are given explicitly. For the full calculation, $\boldsymbol{K}$ and $\boldsymbol{P}$ insertions are also required. These are calculated in the same way as the $\boldsymbol{I}$ insertions, by following the methods outlined in Refs. [64] and [72]. We give the $\boldsymbol{I}$ insertions here as they contain explicit poles and are thus necessary to illustrate the overall cancellation of poles in our calculations.

When using the off-shell treatment of the intermediate top-quark, we must consider the process as a whole and, hence, all incoming and outgoing partons are massless. Therefore, we follow the methods outlined in Ref. [64]. For our process, the general expression for the $\boldsymbol{I}$ insertion is

$$\boldsymbol{I} = \frac{\alpha_s C_F}{2\pi} \sum_i \sum_{j \neq i} \left(\frac{1}{\bar{\epsilon}^2} + \frac{3}{2\bar{\epsilon}} + 5 - \frac{7\pi^2}{12} - \frac{x_{sc}}{2} \right) \left(\frac{\tilde{\mu}^2}{2p_i \cdot p_j} \right)^\epsilon , \qquad \text{(D.1)}$$

where i and j are external quarks on the same fermion line and

$$\tilde{\mu}^{2\epsilon} = \mu^{2\epsilon} e^{\epsilon\gamma_E} (4\pi)^{-\epsilon} \,, \qquad \frac{1}{\bar{\epsilon}} = \frac{1}{\epsilon} e^{-\epsilon\gamma_E} (4\pi)^{\epsilon} \,, \qquad \frac{1}{\bar{\epsilon}^2} = \frac{1}{\epsilon^2} e^{-\epsilon\gamma_E} (4\pi)^{\epsilon} \,. \qquad \text{(D.2)}$$

The introduction of these parameters leads, on expansion in ϵ, to a simplified $\overline{\text{MS}}$ subtraction scheme which involves subtracting only the remaining ϵ-poles. This is explained in Section 5.3. For t-channel production, the insertion splits into pieces due to gluon emission from the upper quark line, denoted [31], and the lower quark line, denoted [42]. For s-channel production, the split is into gluon emission off the initial-state quark line, denoted [21] and the final-state quark line, denoted [43]. This gives

$$\boldsymbol{I}_t = \boldsymbol{I}_{[31]} + \boldsymbol{I}_{[42]} \,, \qquad \text{(D.3)}$$

$$\boldsymbol{I}_s = \boldsymbol{I}_{[21]} + \boldsymbol{I}_{[43]} \,, \qquad \text{(D.4)}$$

for t- and s-channel production respectively, where

$$\begin{aligned}
\boldsymbol{I}_{[xy]} &= \frac{\alpha_s C_F}{2\pi} \left(\frac{1}{\bar{\epsilon}^2} + \frac{3}{2\bar{\epsilon}} + 5 - \frac{7\pi^2}{12} - \frac{x_{sc}}{2} \right) \left[\left(\frac{\tilde{\mu}^2}{2p_x \cdot p_y} \right)^{\epsilon} + \left(\frac{\tilde{\mu}^2}{2p_y \cdot p_x} \right)^{\epsilon} \right] \\
&= \frac{\alpha_s C_F}{2\pi} \left[\frac{2}{\epsilon^2} + \frac{1}{\epsilon} \left(2\ln\left(\frac{\mu^2}{s_{yx}}\right) + 3 \right) + 10 - \frac{7\pi^2}{6} - x_{sc} \right. \\
&\quad \left. + \ln\left(\frac{\mu^2}{s_{yx}}\right) \left(\ln\left(\frac{\mu^2}{s_{yx}}\right) + 3 \right) \right] + \mathcal{O}(\epsilon) \,.
\end{aligned} \qquad \text{(D.5)}$$

When treating the intermediate top-quark using the NWA, our process splits into production and decay subprocesses. Each subprocess contains a massive external particle. For the production subprocess, the massive top-quark is an outgoing particle and we can follow the method outlined in Ref. [72]. For the decay subprocess, the massive top-quark is an incoming particle and we use the expressions given in Ref. [35]. As

the massive particle appears on only one of the quark lines (the lower-quark line in t-channel production and the final-state quark line in s-channel production), the $\boldsymbol{I}$ insertions for these quark lines are split into a production and decay part, while the expressions for the other quark lines remain as they were in the off-shell case. That is,

$$\boldsymbol{I}_t = \boldsymbol{I}_{[31]} + \boldsymbol{I}_{\mathrm{prod},[42]} + \boldsymbol{I}_{\mathrm{dec},[42]} \, , \tag{D.6}$$

$$\boldsymbol{I}_s = \boldsymbol{I}_{[21]} + \boldsymbol{I}_{\mathrm{prod},[43]} + \boldsymbol{I}_{\mathrm{dec},[43]} \, . \tag{D.7}$$

Here,

$$
\begin{aligned}
\boldsymbol{I}_{\mathrm{prod},[xy]} = \frac{\alpha_S C_F}{2\pi} \Bigg\{ &\frac{1}{\epsilon^2} - \frac{1}{\epsilon}\left[2\ln\left(\frac{s_{yt}-m_t^2}{m_t\mu}\right) - \frac{5}{2}\right] - \frac{x_{sc}}{2} + 8 - \frac{11\pi^2}{12} \\
&- \left[\ln\left(\frac{m_t^2}{s_{yt}}\right) + \ln\left(\frac{m_t^2}{s_{yt}-m_t^2}\right) - 1\right]\ln\left(\frac{s_{yt}-m_t^2}{s_{yt}}\right) \\
&+ \frac{1}{2}\ln\left(\frac{\mu^2}{s_{yt}-m_t^2}\right)\left[2\ln\left(\frac{m_t^2}{s_{yt}-m_t^2}\right) + \ln\left(\frac{\mu^2}{s_{yt}-m_t^2}\right) + 6\right] \\
&+ \frac{1}{2}\ln\left(\frac{m_t^2}{\mu^2}\right) - \frac{1}{2}\ln^2\left(\frac{m_t^2}{s_{yt}-m_t^2}\right) - 2\mathrm{Li}_2\left(\frac{s_{yt}-m_t^2}{s_{yt}}\right) \\
&+ \frac{m_t^2}{m_t^2 - s_{yt}}\ln\left(\frac{m_t^2}{s_{yt}}\right) - 3\ln\left(\frac{\sqrt{s_{yt}}-m_t}{\sqrt{s_{yt}}}\right) - \frac{3m_t}{m_t + \sqrt{s_{yt}}} \Bigg\}
\end{aligned}
\tag{D.8}
$$

and

$$
\begin{aligned}
\boldsymbol{I}_{\mathrm{dec},[xy]} = \frac{\alpha_s C_F}{2\pi} \Bigg\{ &\frac{1}{\epsilon^2} - \frac{1}{\epsilon}\left(2\ln\left(\frac{s_{xt}-m_t^2}{m_t\mu}\right) - \frac{5}{2}\right) + \frac{27}{4} - \frac{11\pi^2}{12} - \frac{x_{sc}}{2} \\
&+ \frac{16m_t^4 - 22s_{xt}m_t^2 + 7s_{xt}^2}{2(m_t^2 - s_{xt})^2}\ln\left(\frac{2m_t^2 - s_{xt}}{m_t^2}\right) + \frac{m_t^2}{2(s_{xt}-m_t^2)} \\
&+ \frac{1}{2}\ln\left(\frac{\mu^2}{m_t^2}\right)\left(\ln\left(\frac{\mu^2}{m_t^2}\right) + 5\right) - \ln\left(\frac{s_{xt}-m_t^2}{m_t^2}\right)\left(2\ln\left(\frac{\mu^2}{m_t^2}\right) + 5\right) \\
&+ 2\mathrm{Li}_2\left(\frac{s_{xt}-m_t^2}{m_t^2}\right) + 2\ln^2\left(\frac{s_{xt}-m_t^2}{m_t^2}\right) \Bigg\} \, .
\end{aligned}
\tag{D.9}
$$

Bibliography

[1] N. Cabibbo, "*Unitary Symmetry and Leptonic Decays*," Phys. Rev. Lett. **10** (1963) 531.

[2] M. Kobayashi and T. Maskawa, "*CP-Violation in the Renormalizable Theory of Weak Interaction*," Prog. Theor. Phys. **49** (1973) 652.

[3] F. Abe *et al.* [CDF Collaboration], "*Observation of Top Quark Production in $\bar{p}p$ Collisions*," Phys. Rev. Lett. **74** (1995) 2626 [arXiv:hep-ex/9503002].

[4] S. Abachi *et al.* [D0 Collaboration], "*Observation of the Top Quark*," Phys. Rev. Lett. **74** (1995) 2632 [arXiv:hep-ex/9503003].

[5] W. Bernreuther, "*Top Quark Physics at the LHC*," J. Phys. G **35** (2008) 083001 [arXiv:0805.1333 [hep-ph]].

[6] G. Mahlon and S. J. Parke, "*Single Top Quark Production at the LHC: Understanding Spin*," Phys. Lett. B **476** (2000) 323 [arXiv:hep-ph/9912458].

[7] P. Motylinski, "*Angular Correlations in t-channel Single Top Production at the LHC*," Phys. Rev. D **80** (2009) 074015 [arXiv:0905.4754 [hep-ph]].

[8] J. Alwall *et al.*, "*Is $V_{tb} = 1$?*," Eur. Phys. J. C **49** (2007) 791 [arXiv:hep-ph/0607115].

[9] N. Kidonakis, "*Top Quark Cross Sections and Differential Distributions*," [arXiv:1105.3481 [hep-ph]].

[10] T. Aaltonen *et al.* [CDF Collaboration], "*First Observation of Electroweak Single Top Quark Production*," Phys. Rev. Lett. **103** (2009) 092002 [arXiv:0903.0885 [hep-ex]].

[11] V. M. Abazov *et al.* [D0 Collaboration], "*Observation of Single Top Quark Production*," Phys. Rev. Lett. **103** (2009) 092001 [arXiv:0903.0850 [hep-ex]].

[12] N. Kidonakis, "*Single Top Quark Production at the Fermilab Tevatron: Threshold Resummation and Finite-Order Soft Gluon Corrections*," Phys. Rev. D **74** (2006) 114012.

[13] W. Beenakker, A. P. Chapovsky and F. A. Berends, "*Non-factorizable Corrections to W-pair Production: Methods and Analytic Results*," Nucl. Phys. B **508** (1997) 17 [arXiv:hep-ph/9707326].

[14] A. Denner, S. Dittmaier and M. Roth, "*Non-factorizable Photonic Corrections to $e^+e^- \to WW \to$ Four Fermions*," Nucl. Phys. B **519** (1998) 39 [arXiv:hep-ph/9710521].

[15] R. G. Stuart, "*Gauge Invariance, Analyticity and Physical Observables at the Z_0 Resonance*," Phys. Lett. B **262** (1991) 113.

[16] A. Aeppli, G. J. van Oldenborgh and D. Wyler, "*Unstable Particles in One Loop Calculations*," Nucl. Phys. B **428** (1994) 126 [arXiv:hep-ph/9312212].

[17] M. Beneke, A. P. Chapovsky, A. Signer and G. Zanderighi, "*Effective Theory Approach to Unstable Particle Production*," Phys. Rev. Lett. **93** (2004) 011602 [arXiv:hep-ph/0312331].

[18] M. Beneke, A. P. Chapovsky, A. Signer and G. Zanderighi, "*Effective Theory Calculation of Resonant High-energy Scattering*," Nucl. Phys. B **686** (2004) 205 [arXiv:hep-ph/0401002].

[19] M. Beneke, P. Falgari, C. Schwinn, A. Signer and G. Zanderighi, "*Four-fermion Production Near the W Pair Production Threshold*," Nucl. Phys. B **792** (2008) 89 [arXiv:0707.0773 [hep-ph]].

[20] M. Beneke and V. A. Smirnov, "*Asymptotic Expansion of Feynman Integrals Near Threshold*," Nucl. Phys. B **522** (1998) 321 [arXiv:hep-ph/9711391].

[21] V. A. Smirnov, "*Applied Asymptotic Expansions in Momenta and Masses*," Springer Tracts Mod. Phys. **177** (2002) 1.

[22] P. Falgari, P. Mellor and A. Signer, "*Production-Decay Interferences at NLO in QCD for t-channel Single-Top Production*," Phys. Rev. D **82** (2010) 054028 [arXiv:1007.0893 [hep-ph]].

[23] B. W. Harris, E. Laenen, L. Phaf, Z. Sullivan and S. Weinzierl, "*The Fully Differential Single Top Quark Cross Section in Next-to-leading Order QCD*," Phys. Rev. D **66** (2002) 054024 [arXiv:hep-ph/0207055].

[24] G. Bordes and B. van Eijk, "*Calculating QCD Corrections to Single Top Production in Hadronic Interactions*," Nucl. Phys. B **435** (1995) 23.

[25] T. Stelzer, Z. Sullivan and S. Willenbrock, "*Single Top Quark Production via W-gluon Fusion at Next-to-leading Order*," Phys. Rev. D **56** (1997) 5919 [arXiv:hep-ph/9705398].

[26] Z. Sullivan, "*Understanding Single Top Quark Production and Jets at Hadron Colliders,*" Phys. Rev. D **70** (2004) 114012 [arXiv:hep-ph/0408049].

[27] M. C. Smith and S. Willenbrock, "*QCD and Yukawa Corrections to Single Top Quark Production via* $q\bar{q} \rightarrow t\bar{b}$," Phys. Rev. D **54** (1996) 6696 [arXiv:hep-ph/9604223].

[28] W. T. Giele, S. Keller and E. Laenen, "*QCD Corrections to W-boson Plus Heavy Quark Production at the Tevatron,*" Phys. Lett. B **372** (1996) 141 [arXiv:hep-ph/9511449].

[29] M. Beccaria *et al.*, "*A Complete One-loop Calculation of Electroweak Supersymmetric Effects in t-channel Single Top Production at LHC,*" Phys. Rev. D **77** (2008) 113018 [arXiv:0802.1994 [hep-ph]].

[30] G. Macorini, S. Moretti and L. Panizzi, "*Strong and Electroweak Supersymmetric Corrections to Single Top Processes at the Large Hadron Collider,*" Phys. Rev. D **82** (2010) 054016 [arXiv:1006.1501 [hep-ph]].

[31] N. Kidonakis, "*Higher-order Soft Gluon Corrections in Single Top Quark Production at the LHC,*" Phys. Rev. D **75** (2007) 071501 [arXiv:hep-ph/0701080].

[32] N. Kidonakis, "*NNLL Resummation for s-channel Single Top Quark Production,*" Phys. Rev. D **81** (2010) 054028 [arXiv:1001.5034 [hep-ph]].

[33] H. X. Zhu, C. S. Li, J. Wang and J. J. Zhang, "*Factorization and Resummation of s-channel Single Top Quark Production,*" JHEP **1102** (2011) 099 [arXiv:1006.0681 [hep-ph]].

[34] J. Wang, C. S. Li, H. X. Zhu and J. J. Zhang, "*Factorization and Resummation of t-channel Single Top Quark Production,*" [arXiv:1010.4509 [hep-ph]].

[35] J. M. Campbell, R. K. Ellis and F. Tramontano, "*Single-Top Production and Decay at Next-to-Leading Order,*" Phys. Rev. D **70** (2004) 094012 [arXiv:hep-ph/0408158].

[36] Q. H. Cao and C. P. Yuan, "*Single Top Quark Production and Decay at Next-to-leading Order in Hadron Collisions,*" Phys. Rev. D **71** (2005) 054022 [arXiv:hep-ph/0408180].

[37] Q. H. Cao, R. Schwienhorst, J. A. Benitez, R. Brock and C. P. Yuan, "*Next-to-leading Order Corrections to Single Top Quark Production and Decay at the Tevatron: 2. t-channel Process,*" Phys. Rev. D **72** (2005) 094027 [arXiv:hep-ph/0504230].

[38] J. M. Campbell and F. Tramontano, "*Next-to-leading Order Corrections to Wt Production and Decay,*" Nucl. Phys. B **726** (2005) 109 [arXiv:hep-ph/0506289].

[39] S. Heim, Q. H. Cao, R. Schwienhorst and C. P. Yuan, "*Next-to-leading Order QCD Corrections to s-channel Single Top Quark Production and Decay at the LHC,*" Phys. Rev. D **81** (2010) 034005 [arXiv:0911.0620 [hep-ph]].

[40] R. Schwienhorst, C. P. Yuan, C. Mueller and Q. H. Cao, "*Single Top Quark Production and Decay in the t-channel at Next-to-leading Order at the LHC,*" [arXiv:1012.5132 [hep-ph]].

[41] R. Pittau, "*Final State QCD Corrections to Off-shell Single Top Production in Hadron Collisions,*" Phys. Lett. B **386** (1996) 397 [arXiv:hep-ph/9603265].

[42] W. Beenakker, F. A. Berends and A. P. Chapovsky, "*One-loop QCD Interconnection Effects in Pair Production of Top Quarks,*" Phys. Lett. B **454** (1999) 129 [arXiv:hep-ph/9902304].

[43] V. S. Fadin, V. A. Khoze and A. D. Martin, "*Interference Radiative Phenomena in the Production of Heavy Unstable Particles,*" Phys. Rev. D **49** (1994) 2247.

[44] K. Melnikov and O. I. Yakovlev, "*Top Near Threshold: All α_s Corrections are Trivial,*" Phys. Lett. B **324** (1994) 217 [arXiv:hep-ph/9302311].

[45] J. A. Aguilar-Saavedra, A. Onofre, "*Using Single Top Rapidity to Measure V_{td}, V_{ts}, V_{tb} at Hadron Colliders,*" Phys. Rev. D **83** (2011) 073003 [arXiv:1002.4718 [hep-ph]].

[46] P. Falgari, F. Giannuzzi, P. Mellor and A. Signer, "*Off-Shell Effects for t-channel and s-channel Single-Top Production at NLO in QCD,*" Phys. Rev. D **83** (2011) 094013 [arXiv:1102.5267 [hep-ph]].

[47] J. M. Campbell, R. Frederix, F. Maltoni and F. Tramontano, "*Next-to-leading Order Predictions for t-channel Single Top Production at Hadron Colliders,*" Phys. Rev. Lett. **102** (2009) 182003 [arXiv:0903.0005 [hep-ph]].

[48] J. M. Campbell, R. Frederix, F. Maltoni and F. Tramontano, "*NLO Predictions for t-channel Production of Single Top and Fourth Generation Quarks at Hadron Colliders,*" JHEP **0910** (2009) 042 [arXiv:0907.3933 [hep-ph]].

[49] M. E. Peskin and D. V. Schroeder, "*An Introduction to Quantum Field Theory,*" Westview Press (1995).

[50] L. D. Faddeev and V. N. Popov, "*Feynman Diagrams for the Yang-Mills Field,*" Phys. Lett. B **25** (1967) 29.

[51] A. Denner, "*Techniques for Calculation of Electroweak Radiative Corrections at the One-Loop level and Results for W-Physics at LEP-200,*" Fortsch. Phys. **41** (1993) 307 [arXiv:0709.1075 [hep-ph]].

[52] A. D. Martin, R. G. Roberts, W. J. Stirling and R. S. Thorne, *"Uncertainties of Predictions from Parton Distributions. I: Experimental Errors,"* Eur. Phys. J. C **28** (2003) 455 [arXiv:hep-ph/0211080].

[53] M. R. Whalley, D. Bourilkov and R. C. Group, *"The Les Houches Accord PDFs (LHAPDF) and LHAGLUE,"* [arXiv:hep-ph/0508110.]

[54] P. M. Nadolsky *et al.*, *"Implications of CTEQ Global Analysis for Collider Observables,"* Phys. Rev. D **78** (2008) 013004 [arXiv:0802.0007 [hep-ph]].

[55] A. D. Martin, W. J. Stirling, R. S. Thorne and G. Watt, *"Parton Distributions for the LHC,"* Eur. Phys. J. C **63** (2009) 189 [arXiv:0901.0002v3[hep-ph]].

[56] G. 't-Hooft, *"Renormalization of Massless Yang-Mills Fields,"* Nucl. Phys. B **33** (1971) 173.

[57] G. 't-Hooft and M. Veltman, *"Regularization and Renormalization of Gauge Fields,"* Nucl. Phys. B **44** (1972) 189.

[58] R. K. Ellis and G. Zanderighi, *"Scalar One-loop Integrals for QCD,"* JHEP **0802** (2008) 002 [arXiv:0712.1851 [hep-ph]].

[59] J. C. Collins, D. E. Soper and G. Sterman, *"Heavy Particle Production in High-Energy Hadron Collisions,"* Nucl. Phys. B **263** (1986) 37.

[60] J. C. Collins, D. E. Soper and G. Sterman, *"Soft Gluons and Factorization,"* Nucl. Phys. B **308** (1988) 833.

[61] T. Kinoshita, *"Mass Singularities of Feynman Amplitudes,"* J. Math. Phys. **3** (1962) 650.

[62] T. D. Lee and M. Nauenberg, *"Degenerate Systems and Mass Singularities,"* Phys. Rev. **133** (1964) B1549.

[63] F. Bloch and A. Nordsieck, *"Note on the Radiation Field of the Electron,"* Phys. Rev. **52** (1937) 54.

[64] S. Catani and M. H. Seymour, *"A General Algorithm for Calculating Jet Cross Sections in NLO QCD,"* Nucl. Phys. B **485** (1997) 291 [Erratum-ibid. B **510** (1998) 503] [arXiv:hep-ph/9605323].

[65] S. Frixione, Z. Kunszt and A. Signer, *"Three Jet Cross-Sections to Next-to-Leading Order,"* Nucl. Phys. B **467** (1996) 399 [arXiv:hep-ph/9512328].

[66] Z. Xu, D. H. Zhang and L. Chang, *"Helicity Amplitudes for Multiple Bremsstrahlung in Massless Non-Abelian Gauge Theories,"* Nucl. Phys. B **291** (1987) 392.

[67] M. L. Mangano and S. J. Parke, "*Multi-Parton Amplitudes in Gauge Theories,*" Phys. Rept. **200** (1991) 301 [arXiv:hep-th/0509223].

[68] L. J. Dixon, "*Calculating Scattering Amplitudes Efficiently,*" [arXiv:hep-ph/9601359].

[69] A. Signer and D. Stockinger, "*Using Dimensional Reduction for Hadronic Collisions,*" Nucl. Phys. B **808** (2009) 88 [arXiv:0807.4424 [hep-ph]].

[70] A. P. Chapovsky, V. A. Khoze, A. Signer and W. J. Stirling, "*Non-factorizable Corrections and Effective Field Theories,*" Nucl. Phys. B **621** (2002) 257 [arXiv:hep-ph/0108190].

[71] T. Hahn, "*CUBA: A Library for Multi-Dimensional Numerical Integration,*" Comput. Phys. Commun. **168** (2005) 78 [arXiv:hep-ph/0404043].

[72] S. Catani, S. Dittmaier, M. H. Seymour and Z. Trócsányi, "*The Dipole Formalism for Next-to-Leading Order QCD Calculations with Massive Partons,*" Nucl. Phys. B **627** (2002) 189 [arXiv:hep-ph/0201036].